The Interactions Between Fire and Hyrdoclimate Over Seasonal Timescales

Michael Vijay Saha

Charlottesville, VA

Bachelor of Science, The University of Virginia, 2012

A Dissertation presented to the Graduate Faculty of the University of Virginia in Candidacy for the Degree of Doctor of Philosophy

Department of Environmental Sciences

University of Virginia

May, 2018

Committee

Todd M. Scanlon (*Advisor*)

Paolo D'Odorico (*Advisor*)

Howard Epstein

Jonathan Goodall

Dedicated to the memory of Arunava Saha

Not the first or the last in a tradition of Science

Acknowledgements

This work was only realized with years of selfless support from colleagues, friends and family. Profound thanks to all who gave their love, encouragement, time, knowledge, ideas and funding.

An incomplete list

Jillian
Todd & Paolo
Office 274 and the larger department
Kyle, Jessica, Alex, Matthew, Alice, Seekell, Grace, Liz & Cal
Abi, Mo, Rwaza, Patrick, Nandos, Bostick & the rest of the Bots crew
David Hondula & Bob Davis
Daniel, Jessie, Neena & Joey
Mom, Eric, Ida & Rich

The institutions brave enough to fund me

The Virginia Space Grant Consortium
The National Aeronautics and Space Administration
The University of Virginia Department of Environmental Sciences
The National Socio-Environmental Synthesis Center
The National Science Foundation

Table of Contents

List of Figures

List of Tables

Abstract

Fire is a ubiquitous component of the Earth system and in African drylands in particular. It represents a dramatic and instantaneous change at the land surface by affecting plant communities, hydrologic cycling and the energy balance. The aim of this dissertation is to build understanding of how fire is affected by, and in turn affects, regional climate.

This dissertation consists of research on two fronts. In the first I develop a novel methodology to explore the hypothesis that strong seasonality enhances burned area. Using monthly, global, gridded temperature and precipitation data I derived seasonality metrics that can be used to describe a periodic seasonal cycle. Using just three such metrics and a random forest model, I explained 66% of the variance in global burned area, on par with significantly more complex models that are limited to a regional scope. A more complex random forest model that included nine seasonality correctly predicted 87% of the variability in global burned area. These findings confirm that seasonality plays a large role in determining global burned area and suggest mechanism by which this occurs. The methodology developed in this Chapter will be useful for other researchers wishing to describe seasonality using standardized, interpretable metrics.

The second research area surrounds the hypothesis that fire can influence rainfall on seasonal timescales. First, I demonstrated a relationship between dry season fires and subsequent with a statistical model and observational data. I find that more extensive and later dry season fires account for reductions of up to 30 mm of rainfall (~%10 of average yearly totals) in the subsequent dry season. The observed effect is strongest in regions that are already water limited. This could potentially lead to a negative feedback represented by an interannual oscillation in rainfall and fire activity, an effect observed in actual rainfall records.

I then used a simple physically-based boundary layer model to evaluate how the land surface could contribute to these observed rainfall deficits over the Kalahari region of southern Africa. Using simple, but realistic parameterizations of fire at the land surface, I showed that positive albedo anomalies (brightening) or increases in latent heat flux after fire could explain observed rainfall reduction. This is in large part by less vigorous boundary layer growth and a reduced probability of the boundary layer exceeding the lifting condensation layer. I also showed new satellite-based evidence that brightening does indeed occur after fires over the Kalahari transect in regions receiving less that 850 mm of rainfall annually. This finding challenges the idea that immediate darkening is the only meaningful albedo change after dryland fires and supports the idea that brightening is responsible for observed rainfall deficits after fire.

Finally, I extended this observational approach to the whole continent of Africa. I applied a pixel grouping technique to label satellite burned area data into individual fire events and compared the albedo following fire to a surrounding unburnt reference region. On average albedo was $+2.71 \times 10^{-4}$ higher in burn scars in the five years following fire, representing a statistically significant negative forcing on a continental scale. These findings build new understanding of the land surface effect of fire and the potential for interactions with regional hydroclimate.

Chapter One

Introduction

To the dryland ecologists
Wherever they may be
In whatever time they work

Frank Herbert
Dedication of *Dune*

1.1 The geography of Africa

Drylands are regions where ecosystems and physical processes are shaped by the perennial or intermittent limitation of available moisture [*Nicholson*, 2011]. Much of this dissertation focuses on physical processes in the drylands of sub-Saharan Africa. Geographically, Africa is a unique continent, spanning nearly 70° of latitude from 35° S to 40° N. This vast range shapes the major continental features and offers a wide range of heterogeneous, interesting and understudied landscapes.

At a continental level, the main hydroclimatic features are an equatorial band of high moisture availability near the equator and two subtropical arid zones relating to the diverging Hadley cells around 30° N and 30° S [*Nicholson*, 2011]. These features are largely shaped by the presence of the intercontinental tropical convergence zone (ITCZ), a band of low pressure close to the equator that promotes rainfall. Near 0° the ITCZ remains close year-round, and rainfall is common. Outside of these bands, in relation to subtropical highs, are the two corresponding dry bands of the hyperarid Saharan desert and the less expansive Kalahari desert in southern Africa. Between these bands there are semi-arid regions—the Sahel in the northern hemisphere and the Kalahari transect in the southern hemisphere—where rainfall is highly seasonal, and wet seasons correspond to the seasonal, zonal migration of the ITCZ [*Koch et al*., 1995; *Nicholson*, 2011].

These natural moisture gradients offer two exceptional testbeds for understanding how both physical and ecological processes function with varying moisture availability. Many such processes—large scale ecology [*Staver et al*., 2011], fire frequency [*Van Der Werf et al*., 2008], and land-atmosphere feedbacks [*Koster et al*., 2004; *Seneviratne et al*., 2010; *Nicholson*, 2015]—are known to be at least partially determined by these striking trends in moisture availability. In many ways, these large geographical trends are unique to Africa.

The study water of resources in Africa is not only interesting from a scientific perspective, but is also societally relevant [*Wang et al*., 2012]. In drylands there is extremely high variability in interannual rainfall totals [*Nicholson,* 2011]. Intraseasonal moisture variability is also highly intermittent; in some cases the whole of wet season rainfall is supplied in just a few storms. In these regions, the limitation of water resources is historically associated with loss of livelihood and lives. Many local economies are either directly or indirectly tied to the stable availability of water [*Reynolds et al*., 2007]. Understanding how Earth System processes such as fire might impact water is essential for improving predictions and mitigating the societal effects of drought on a seasonal time-scale. For this reason, understanding the physical determinants, as well as possible feedbacks that may aide or hamper the predictability of seasonal rainfall is extremely important. A goal of this dissertation is to examine the extent to which an important land surface process—fire—might modify rainfall over large areas.

1.2 The fire continent

Fire in Africa is extremely common, burning up to 10% of the land area on an annual basis. In some regions fire frequency approaches an annual return interval. However, like many features of the continent, this is highly dependent on geography. Fire is most common in regions around 1200 mm of mean annual precipitation (MAP). The 'sweet spot' in these moderate rainfall bands is due to the conflicting requirements of moisture availability for fuel accumulation and the desiccation and curing of fuel necessary for fire to spread [*Van der Werf et al*., 2008]. The extreme frequency of fire shapes the environment in profound ways. Frequent disturbance creates stable savanna plant communities with discontinuous woody cover and a continuous herbaceous understory [*Staver et al*., 2011]. This continuous bed of fuel in turn promotes frequent fires, leading to a feedback cycle in which savanna is maintained. These feedbacks suppress woody cover on a continental level substantially below what is expected from water resources available to plants [*Sankaran et al*, 2005]. These savanna ecosystems dominate much of the land area of semi-arid Africa. An additional motivation of this research involves the linkage between humans and fire [*Andela & Van Der Werf*, 2014]. By causing or suppressing fires over large scales, humans may be unwittingly influencing regional climate in regions where water is already scarce.

1.3 Land-atmosphere interactions

There is growing recognition of the role that the land surface plays in modifying regional weather and climate. Research along this path has a strong history in semi-arid regions of Africa. One such example is the classic hypothesis of Charney [1975] used to explain a decades-long drought in the Sahel. Charney proposed a positive feedback cycle in which desertification causes brightening of the land surface. This in turn causes atmospheric subsidence and reduces rainfall, thereby intensifying the desertification. This hypothesis has been supported by more recent application of sophisticated interactive climate and land-surface models [*Meng et al.*, 2014].

Another example of land-atmosphere interactions specific to Africa is the negative soil moisture-rainfall feedback proposed by Taylor *et al*. [2011]. These researchers observed that initiation of mesoscale convective systems in the Sahel were preferentially located downwind of regions that were drier than the surrounding area. The proposed mechanism suggested that boundary layer instability due to warmer, dry soils instigates the formation of large convective systems that are responsible for a majority of rainfall in the Sahel. These findings were in direct contrast to predictions of climate models that tend to 'lock in' periods of drought through positive feedbacks. These studies demonstrate the importance of the land surface in the generation of rainfall and the ways in which modeling and observation can be used to form a mechanistic understanding of land-atmosphere feedbacks. This understanding can in turn aide the prediction of rainfall and help inform future modeling and validation efforts. Semi-arid regions are a focus for land-atmosphere interactions because they exist at the intersection of warm dry regions with high available energy for convective processes (but little available moisture), and wet regions with high moisture availability where available energy and convective instability might be lacking [*Seneviratne et al*., 2010; *Nicholson*, 2011]. It is precisely in these regions the inputs of energy and moisture from the land surface can modulate atmospheric processes.

1.4 Research Needs

While some land-based controls on precipitation have been demonstrated in the past, the possibility of fire-induced rainfall modification has not yet been studied. This is due to a few factors. First, there is lack of understanding of the physical changes associated with fire, especially over an extended timeframe. Even the directional change of albedo—a land surface property known to influence land-atmosphere interactions—is not known weeks and months after fire occurs. For fire to have a substantial impact on seasonal rainfall total, the land surface changes following a typical dry season burn would need to be sustained over multiple storms, well into the wet seasons. Understanding how the physical properties of the land surface recover after fire is key in predicting how fire might modify boundary layer dynamics. There are widespread reports that reaffirm the short-term darkening due to char on the land surface immediately after fire. However, knowledge of long-term land-surface effects of fire on a continental level is precisely what is missing in the literature. This dissertation aims to fill that gap using maturing long-term satellite datasets.

Even with knowledge of the effect of fire on the land surface, it is unclear how this might impact atmospheric processes. Boundary layer modeling with parameterizations for fire based on observations are needed investigate the potential for land-atmosphere interactions. This could provide a mechanistic link between fire and rainfall. Finally, even if physical models suggest fire-induced rainfall modification can occur, it is unclear if this is manifested in reality. The results must be confirmed with measurements. This dissertation represents the first such attempt to link fire to long-term rainfall using observations.

1.5 Outline

I broadly investigate the role of fire both as a cause and a result of regional climate in this dissertation. In Chapter Two I explore the effect of climatic aspects on the presence of fire on a global basis. I specifically investigate how large predictable intraannual variations in climate signals contribute to fire frequency. In Chapter Three I investigate the potential impact of fire on rainfall using an observational approach. This represents the first observational study associating fire with long-term changes in rainfall. Chapter Four explains this phenomenon mechanistically through the lens of boundary layer interactions. I provide an explanation that invokes observed increases in land surface reflectivity, or brightening, after fire to explain reduced convective rainfall. In Chapter Five I expand the exploration of brightening to the whole continent and demonstrate that the Kalahari in particular drives overall net brightening after fires. I end with a conclusion summarizing the new scientific knowledge and methodological advances that stem from the studies.

1.6 References

Andela, N., & Van Der Werf, G. R. (2014). Recent trends in African fires driven by cropland expansion and El Nino to La Nina transition. *Nature Climate Change*, *4*(9), 791.

Charney, J. G. (1975). Dynamics of deserts and drought in the Sahel. *Quarterly Journal of the Royal Meteorological Society*, *101*(428), 193-202.

Koch, G. W., Vitousek, P. M., Steffen, W. L., & Walker, B. H. (1995). Terrestrial transects for global change research. *Vegetatio*, *121*(1-2), 53-65.

Koster, R. D., Dirmeyer, P. A., Guo, Z., Bonan, G., Chan, E., Cox, P., ... & Liu, P. (2004). Regions of strong coupling between soil moisture and precipitation. *Science*, *305*(5687), 1138-1140.

Meng, X. H., Evans, J. P., & McCabe, M. F. (2014). The influence of inter-annually varying albedo on regional climate and drought. *Climate dynamics*, *42*(3-4), 787-803.

Nicholson, S. E. (2011). *Dryland Climatology*. Cambridge University Press.

Nicholson, S. E. (2015). Evolution and current state of our understanding of the role played in the climate system by land surface processes in semi-arid regions. *Global and Planetary Change*, *133*, 201-222.

Reynolds, J. F. *et al.* (2007). Global desertification: building a science for dryland development. *Science*, *316*(5826), 847-851.

Sankaran, M., Hanan, N. P., Scholes, R. J., Ratnam, J., Augustine, D. J., Cade, B. S., ... & Ardo, J. (2005). Determinants of woody cover in African savannas. *Nature*, *438*(7069), 846.

Seneviratne, S. I., Corti, T., Davin, E. L., Hirschi, M., Jaeger, E. B., Lehner, I., ... & Teuling, A. J. (2010). Investigating soil moisture–climate interactions in a changing climate: A review. *Earth-Science Reviews*, *99*(3-4), 125-161.

Staver, A. C., Archibald, S., & Levin, S. A. (2011). The global extent and determinants of savanna and forest as alternative biome states. *Science*, *334*(6053), 230-232.

Taylor, C. M., Gounou, A., Guichard, F., Harris, P. P., Ellis, R. J., Couvreux, F., & De Kauwe, M. (2011). Frequency of Sahelian storm initiation enhanced over mesoscale soil-moisture patterns. *Nature Geoscience*, *4*(7), 430.

Van Der Werf, G. R., Randerson, J. T., Giglio, L., Gobron, N., & Dolman, A. J. (2008). Climate controls on the variability of fires in the tropics and subtropics. *Global Biogeochemical Cycles*, *22*(3).

Wang, L., D'Odorico, P., Evans, J. P., Eldridge, D. J., McCabe, M. F., Caylor, K. K., & King, E. G. (2012). Dryland ecohydrology and climate change: critical issues and technical advances. *Hydrology and Earth System Sciences*, *16*(8), 2585-2603.

Chapter Two

Climate Seasonality as an Essential Predictor of Global Fire Activity

Some day you will die and somehow
Something's going to steal your carbon.

Modest Mouse

Substantial parts of this Chapter to be published in

Saha, M. V. Scanlon, T. M. & D'Odorico, P. (*Accepted pending minor revisions*). Climate Seasonality as an Essential Predictor of Global Fire Activity. *Global Ecology and Biogeography*.

2.1 Abstract

Fire is a globally important disturbance that affects nearly all vegetated biomes. Previous regional studies have suggested that the predictable seasonal pattern of a climatic time-series, or seasonality, may aid in the prediction of average fire activity, but it is not known if these findings are applicable globally. Here I investigate how seasonality can be used to explain variations in fire activity on a global scale. I describe a method to partition a periodic seasonal cycle into two seasons and define conceptually simple temporal metrics that describe spatial variability in seasonality. I explore the usefulness of these metrics in explaining global fire activity using the average monthly time series of precipitation and temperature and a flexible machine learning procedure (random forests). A simple model that uses only precipitation and temperature amplitude and synchrony between wet and warm seasons correctly predicts 66% of the variability in global fire activity, substantially higher than a model with mean annual temperature and precipitation. A more complex model that includes nine seasonality metrics predicts 87% of variability in global fire activity. This study shows that seasonality of temperature and precipitation can be used to predict long-term fire activity in a globally relevant way. This new method may be useful in hindcasting historical fire from station data or predicting future fire regimes using coarse output from climate models.

2.2 Introduction

Fires burn in virtually all vegetated biomes at varying frequency and intensity. On an annual basis up to 400 Mha of the terrestrial land surface is burned [*Schultz et al.*, 2008]. These fires influence vegetation composition [*Staver et al.*, 2011], global carbon cycling [*Randerson et al.*, 2012], human health [*Bowman & Johnston*, 2005] and the climate system over a range of scales [*Kaufman et al*., 2002; *Tosca et al*., 2014; Chapter Five]. Understanding the climatic causes of the biogeography of fire activity may aide in the prediction of future fire regimes and the global carbon dynamics under a changing climate.

Previous research has examined the effect that climate has on fire activity, and how various factors such as fuel accumulation, drought, and fire weather (i.e., local hot and dry conditions that promote the flammability of the fuel bed) mediate the occurrence of fire [*Krawchuk & Moritz*, 2014; *Hantson et al*., 2016]. In this study I examine seasonality, which I define as the predictable yearly cycle of an environmental variable, and seasonality metrics; quantitative descriptions of various aspects of the typical seasonal cycle. Seasonality is typically linked to fire due to the conditions that must be met in order for fire to occur [*Bradstock*, 2010]. On one hand, frequent fire must be supported by high fuel accumulation rates through net primary productivity. On the other hand, warm and dry weather conditions that promote the curing of fuels and the contiguity and flammability of the fuel bed ("fire weather") must also occur. To support frequent fires on an annual basis, these dual conditions must be met frequently as well. In many cases, specifically in the seasonally water-limited tropics and subtropics, plant productivity is promoted by cooler, wetter conditions that lift growth limitations due to heat and water stress. In other regions, such as high-latitude forests, low temperature may be the limiting factor for plant growth, and the growing season and fire season have significant overlap. These spatially and temporally varying constraints make the prediction of global fire activity difficult [*Hantson et al*., 2016]. To date, a global study of the effect of climate seasonality on spatial patterns of fire has not been undertaken.

A number of past studies have identified a positive relationship between strong shifts in a climatic variable over the course of the year (i.e. a marked seasonal pattern) and long-term fire activity. However, these studies tend to focus on certain regions or climatic gradients (e.g. Archibald *et al*., [2009]; Mondal & Sukumar, [2016]), or selectively pool data over large spatial units in recognition that different aspects of climate may be regionally important contributors to lower fire return intervals [*Pausas & Ribeiro*, 2013; *Bowman et al*., 2014]. Furthermore, the precise definition of seasonality differs between studies. For the purpose of relating climate to fire, seasonality has been defined variously as the number of months with rainfall under a variable threshold (such as 100 mm, as in Van der Werf *et al*. [2008]), the number of months accounting for less than some percentage of mean annual precipitation [*Archibald et al*., 2009], rainfall accumulated during certain fixed months [*Mondal & Sukumar*, 2016] or rainfall accumulated during the six driest months of the year [*Bowman et al*., 2014]. A more subtle difficulty in synthesizing the results of previous seasonality-fire findings stems from differences in how seasonality is actually represented. For example, the aforementioned definitions from previous studies suggest that seasonality can be represented by durations, rates or accumulations of some variable of interest. The diversity of the metrics that different studies have found to be statistically important suggests that multiple aspects of intra-annual variability contribute to what is commonly called ‘seasonality’; a single metric is unlikely to capture all of these facets. Typically, these metrics are defined based on a specific knowledge of the system being studied and are appropriate for a specific region. While ad hoc definitions may be appropriate for regional studies where the general seasonal pattern of a climate variable like rainfall is spatially homogeneous, these metrics may not be as useful in other regions where the seasonal precipitation patterns differ. This makes comparison between studies difficult and precludes generalizations about importance of climate seasonality at the global level. For example, studies that report a precipitation seasonality metric typically find that a positive association exists between the strength of intra-annual shifts and the amount of fire (e.g. Bowman *et al.*, [2014]). It is unclear if the opposite is true, i.e. if a weak seasonal precipitation cycle is associated with lower fire activity. Furthermore, a variable representing some aspect of the seasonal cycle is often included alongside other predictors, so it is unclear if seasonality metrics alone can accurately predict average fire activity at regional or larger scales.

A standardized method for quantifying seasonality would be useful for study inter-comparison and understanding more generally the role of climate seasonality in promoting or suppressing global fire activity. This method would ideally exclude ad-hoc metrics and data sources that are only relevant or available on a regional basis and instead be robust and generally applicable to all vegetated biomes. The results of such an analysis could be used for hindcasting historical fire activity based on station data as well as understanding data needs for predicting future fire.

While aspects of seasonality in climatic fields have been used to understand variability in fire in specific biomes, a formal quantitative and globally consistent approach has not yet been undertaken. This is a gap that I aim to fill in the current study. The goals of this study are (1) to develop a suite of conceptually simple, multi-faceted and globally applicable seasonality metrics, (2) to apply these metrics to global rainfall and temperature datasets and test their effectiveness as statistical predictors of global burned area, and (3) to understand the relationship between these metrics and burned area and place these results in the context of ongoing pyrogeographic research.

2.3 Data

2.3.1. Study Area and Period

I calculate the seasonality metrics over the global land surface from latitude 60° S to 60° N on a 0.25° grid. This latitudinal limitation is the maximum extent of satellite-based global precipitation estimates at higher latitudes. All average monthly (precipitation and rainfall) and yearly (fire) data are derived from monthly data spanning the time period 1999-2015.

2.3.2. Fire

I use fire data from the GFED version 4 fire product with small fires [*Randerson et al.*, 2012]. This product uses MODIS-derived burned area estimates with corrections to account for underestimation of low intensity or canopy-obscured fires. The data are available globally at 0.25° resolution, on the same grid as rainfall. Overall, 98.6% of GFED burned area occurs within the bounds of the study area (60° S to 60° N), mainly missing fire activity in the boreal zone. I converted the monthly input data to average monthly burned area, then summed these values to achieve yearly average proportion burned for each pixel (Fig. 2.1). It is spatial variations in this response variable (average annual proportion burned) that I try to predict using seasonality metrics derived from climatic variables.

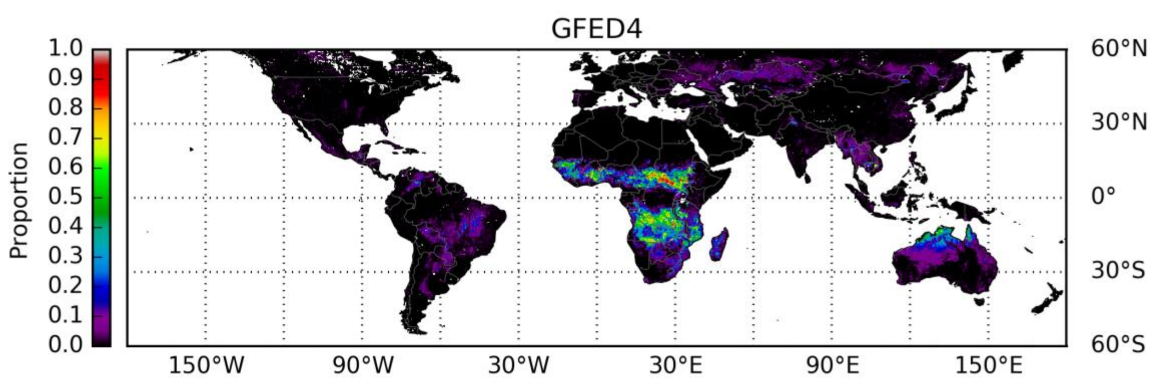

Figure 2.1. GFED4 average annual proportion burnt.

2.3.3 Rainfall

I performed the main analysis on the PERSIANN-CDR rainfall product [*Ashouri et al.*, 2015]. PERSIANN-CDR trains artificial neural networks to associate satellite brightness temperature with observed variations in rainfall. Estimates are then bias adjusted to match gauge-derived estimates from the Global Precipitation Climatology Project version 2.2 monthly estimates.

2.3.4 Temperature

I use the GHCN+CAMS global near surface air temperature dataset [*Fan & Van den Dool*, 2008]. This dataset is available as monthly means at 2.5° resolution. I down-sample to the 0.25° resolution of the fire and rainfall product by taking the temperature value of the closest 2.5° pixel centroid to each 0.25° pixel centroid (i.e. nearest neighbor downscaling).

2.4 Methods

2.4.1 Aim

My aim is to define simple metrics that succinctly describe how a climatic variable of interest varies over the course of an average year. As such, I assume that each variable oscillates between two periods over the course of the year (not necessarily a calendar year), where the values it takes are alternatively high and low. This assumption is physically rooted in the effects of Earth's obliquity, which is then manifested, for example, as seasonal variations between low and high temperature or the latitudinal migration of the inter-tropical convergence zone. However, this assumption is not valid for all regions. I also included a metric (seasonality index) that describes how appropriate this assumption is in different regions.

2.4.2 Seasonal Partitioning

It is assumed that the input data is a vector X of N regularly spaced measurements representing a single yearly cycle. In this study I considered monthly samples (N=12), but all of the following methods can be extended to regularly sampled data at any time scale, such as average daily (N=365); or seasonal (e.g. DFM, MAM, JJA, SON; N=4) values. Therefore the valid temporal indices, I, into X are:

$$I \in \{1,2,\ldots,N\}$$

Indexed subsets of X are denoted by X_S, where $S \subset I$. The mean of a given subset of X, $\bar{X}_S$, is defined as:

$$\bar{X}_S = \frac{\sum_{x \in X_S} x}{|S|}$$

where $|S|$ denotes the cardinality (number of elements) of an indexing set S and x is a given element of X. The variability of an indexed subset is defined as the within-season residual sum of squares:

$$V_S = \sum_{x \in X_S} (x - \bar{X}_S)^2$$

with total variability of the yearly cycle for a given variable (V_T) equal to:

$$V_T = \sum_{x \in X_I} (x - \bar{X}_I)^2$$

A season is defined as a contiguous subset of the possible indices, where contiguity is defined in the periodic sense such that index 12 (December) is contiguous to index 1 (January). For example, {12, 1, 2, 3} is a valid season, representing December, January, February and March. The set {5, 7, 8}, is not a valid season, because 5 (May) is not contiguous with 7 (July) or 8 (August). Every season is required to contain at least one index (or month of data for N=12). My goal was to partition X into two seasons with no common elements. For convenience the indexing set whose average indexed value is greatest is referred to as H (high season) and the other season as L (low) season, given by the following definition:

$$\bar{X}_H > \bar{X}_L$$

The definitions of high and low seasons are not predefined; their existence is a consequence of the following minimization procedure. I partitioned the seasons such that the sum of the within season variability is minimized:

$$\underset{H,L}{argmin} = V_H + V_L$$

where H and L are contiguous indexing sets with no common elements.

2.4.3 Amplitude

Using the above approach I defined metrics that capture different aspects of seasonality First, I defined the amplitude of a vector X, A_X, as the difference between the average value of the high and low seasons:

$$A_X = \bar{X}_H - \bar{X}_L$$

In more sophisticated models, I also considered the average low and high seasonal values ($\bar{X}_L$ and $\bar{X}_H$) as metrics, in which case the amplitude is not included as a predictor.

2.4.4 Duration

Seasonal duration is the number of months in the low season:

$$D = |L|$$

There is a constraint on the duration $|H| + |L| = N$. I excluded high season length as it does not offer any extra information to the statistical model.

2.4.5 Seasonality Index

The partitioning procedure assumes that the seasonal cycle can reliably be represented as one of two discrete values at different points in the year. While this assumption is based ultimately on the obliquity of the earth, it may not be valid in all regions. For this reason, I defined another metric, the seasonality index (*S*), that captures how well the two-season assumption fits the observed data yearly cycle. The seasonality index is defined as follows:

$$S = 1 - \frac{V_H + V_L}{V_T}$$

The value of *S* is between 0 and 1 and approaches 1 as the proportion of variability explained by the partitioning approaches the total variability observed in the yearly cycle. Fig. 2.2 shows how *S* varies for two different locations. The variable *S* is invariant under shifts in the magnitude and amplitude of the individual seasons. The seasonality index is a measure of how coherent the time-series is within each season relative to the variability of the time-series as a whole. For example, if the wet season is frequently interrupted by intermittent dry periods or a minor dry season (as in Fig. 2.2b) then fuel accumulation (and subsequent fire) could be impacted. Similarly, if the dry season were frequently interrupted by wet periods, then fire would also become less likely. In both these cases the seasonality index would be lower than if there were single consistent wet (warm) periods followed by consistent dry (cool) periods, with little intra-seasonal variability (as in Fig. 2.2a). Therefore, I expect regions with a larger seasonality index (i.e. high *S*) to promote greater fire activity across the globe.

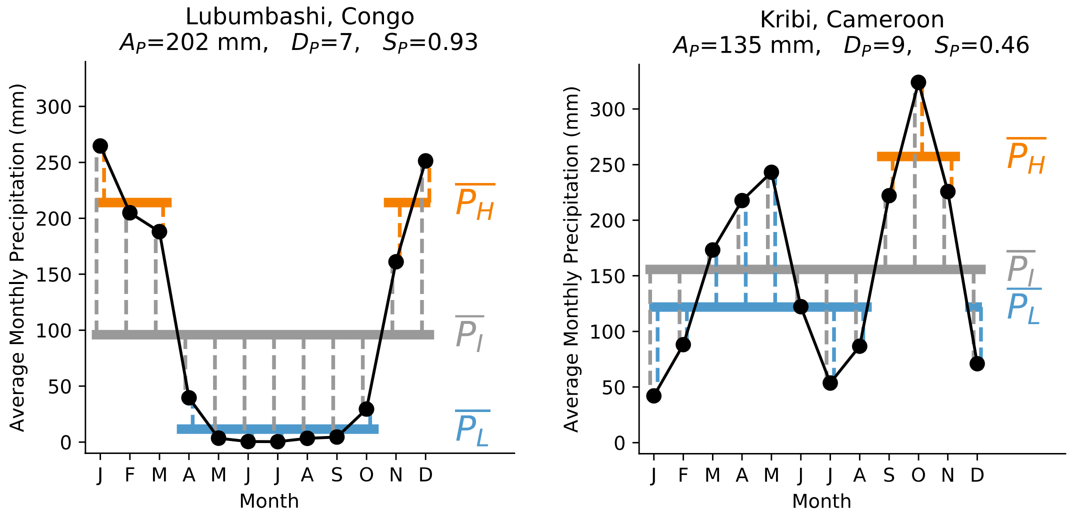

Figure 2.2. An illustration of the seasonal decomposition technique at two locations in Africa. The sum of the squared magnitudes of the orange and blue dashed lines are minimized to find the seasons. In each panel the black line represents average monthly rainfall amount and the height of the solid gray line represents the yearly average. The solid orange and blue lines represent the high ($\bar{P}_H$) and low ($\bar{P}_L$) season rainfall averages, respectively. Mean annual precipitation ($\bar{P}_I$), seasonal duration (D_P), and seasonality index (S_P) are noted for these two examples.

2.4.6 Seasonal Overlap

I defined one final variable, seasonal synchrony ($O_{P,\,T}$), that describes the overlap between two seasonal decompositions. Synchrony is defined as the number of months of overlap between the respective high and low seasons of two seasonal decompositions and is a way of measuring the relative phase of two seasonal cycles over a discrete number of months. Given two seasonal decompositions of high and low season month indices given by the indexing sets H_T, L_T and H_P, L_P, (for temperature and precipitation, respectively) synchrony is defined as:

$$O_{P,T} = |H_T \cap H_P| + |L_T \cap L_P|$$

where ∩ denotes set intersection and || denotes set cardinality. High overlap indicates that the warm season and the rainy season are in phase, while low cardinality indicates that the warm season tends to overlap with the dry season. Note that the overlap variable ($O_{P,T}$) is only defined for models that include both precipitation and temperature data.

2.4.7 Application of Metrics

All of the aforementioned metrics are computed independently for each land pixel in the domain. It is important to reiterate that these metrics can be used on any regularly spaced vector representing an average year and can be applied to a data vector that contains negative data points as well. Given the generality and interpretability of the seasonality metrics I envision that these metrics could be applied to the investigation of other seasonal cycles. One immediate extension of this current study is to apply the seasonality decomposition to investigate the seasonality of the yearly fire cycle. In this study I extract spatially varying seasonality metrics for the average yearly cycle of precipitation (a monthly data vector P, taking the place of the generic data vector X referred to above) and temperature (T). I refer to seasonality metrics computed on the precipitation and temperature data with the subscript $_P$ and $_T$, respectively. $O_{P,T}$ is calculated using the results from the seasonality decomposition of both the T and P data vectors, all other metrics are calculated using just one of the input data vectors.

2.4.8 Statistical Model

The aim of this study is not to compare particular statistical methods but rather to test whether a flexible enough statistical model, when given inputs that correspond to different seasonality metrics, can accurately predict global fire activity. It was necessary for the statistical model I chose to be able to handle non-linear and non-monotonic relationships between the predictors and burned area, making methods such as generalized linear models unsuitable for this task. I opted for random forests, a method that uses an ensemble of regression trees that vote on a continuous outcome variable [*Breiman*, 2001]. Random forests (RF) have been used previously for prediction of spatially varying fire activity. For example, Archibald *et al*. [2009] used random forests to predict fire occurrence using a suite of physical predictors and proxies for human activity and were able to explain 69% of variability in burned area. Additionally, RF estimators are adept at handling highly quantized metric (continuous) variables, like the duration metric (D_P/D_T).

I built a suite of models to demonstrate the efficacy of temperature and precipitation seasonality indicators as a predictor of fire activity. One third of variables were considered during each tree building iteration. Each random forest model was built with 1000 regression trees. All models are trained on a random subset of 70% of all land pixels in the domain, reserving the other 30% of the data for validation. As a measure of predictive performance, I report the proportion of variance explained in the validation data that is explained by models trained only on the independent training set. I compared these accuracy scores to a model using the same training procedure, but only MAP and MAT as inputs. I also report variable importance, which ranks a variable based on the expected decrease in predictive accuracy of the model were the variable randomly permuted. Finally, I visualize the per-pixel predictions and errors for all pixels on global maps to highlight how the performance of the models varies spatially.

The random forest method offers a flexible way to achieve high predictive accuracy with interacting inputs, but understanding the relationship between disparate variables and their effect on fire activity is more difficult. To accomplish this, I visualized how fire varies with seasonality metrics within regional climatic envelopes by conditioning on different climatic variables like mean annual precipitation (MAP) and mean annual temperature (MAT). First conditioning on MAT and MAP is useful because seasonality metrics, such as amplitude or seasonality may be associated with average climate. Without first stratifying based on MAT and MAP, I could not be certain that patterns of fire activity are due to the changes in seasonality metrics rather than a spurious correlation with the underlying average temperature and rainfall.

2.5 Results

2.5.1 Global Seasonality Metrics

I first briefly report the global patterns of the computed seasonal metrics (Fig. 2.3). The precipitation amplitude is typically highest within the tropics (Fig 2.3c). Low rainfall amplitude dominates temperate continental regions. A long (>9 months) dry season is found in the Sahara and Horn of Africa (Fig 1.3e). Elsewhere, long dry seasons (>6 months) are consistently observed in southern Africa, continental Asia and Australia. High precipitation seasonality indices (S_P) are observed in largely the same regions as high precipitation amplitude, approaching 1.0 (i.e. that a two-mean partition explains almost all of the intra-annual variability in precipitation) in southern Africa, central America and northern Australia. Precipitation seasonality indices less than 0.5 are observed consistently in the Horn of Africa.

Temperature amplitude is largest in high-latitude northern hemisphere and lowest in the tropics. The moderating influence of the ocean on near surface air temperature is observed in coastal regions, for example, in the coastal regions of southern Africa or Australia. Globally, the cool season tends to be shorter (<4 months) than the warm season, except in equatorial Africa and parts of Brazil. Spatial variability in the temperature seasonality index (S_T) is less pronounced than for S_P. Both the highest and lowest variability are observed in the tropics, where both higher (S_T>0.9) and lower (S_T<0.6) show spatial variability on sub-regional (<1000 km) scales. Overall, the seasonal decomposition of temperature also captures a majority (> 50%) of the intra-seasonal variability across the globe.

The overlap between high and low seasons of temperature and precipitation, ($O_{P,T}$), is typically high in South America, southern Africa, western Asia, central United States and Australia (Fig. 2.3i). Notable exceptions where the rainy season and the warm season are out of phase occur in equatorial climates and Mediterranean climates (i.e. the Mediterranean, Pacific coastal U.S., southwestern Australia).

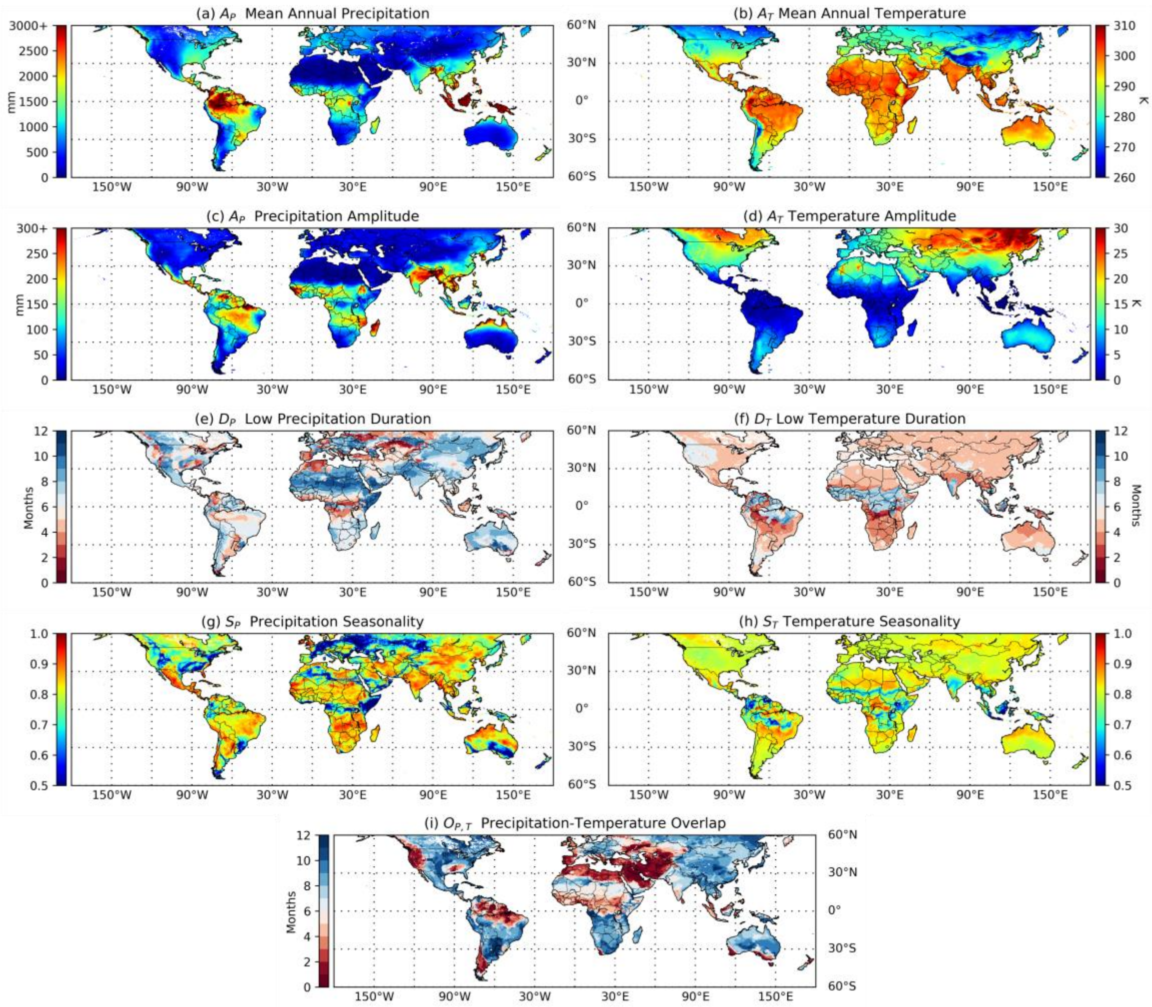

Figure 2.3. Global pattern of seasonality metrics. (a) Mean annual PERSIANN-CDR precipitation, (b) mean annual temperature. (c, d) Amplitude of precipitation and temperature. (e, f) duration of the low precipitation and low temperature season. (g, h) Seasonality index of precipitation and temperature. (i) Overlap ($O_{P,\ T}$) showing the number of months of overlap between the wet and warm season and the dry and cool season.

2.5.2 Statistical Modeling Results

Models ranged in accuracy from 29.3% to 87% of variability explained (Table 2.1). Only two of the various models I built did not explain at least 50% of variability in global fire activity. A baseline model random forest model using MAT and MAP as predictors explained just 46%. The best model with only three variables, A_P, A_T and $O_{P,\,T}$ (i.e., the amplitude of precipitation and temperature seasonality and the seasonal overlap, respectively), correctly predicted 66% of the variability in fire activity in the testing set (Fig. 2.4). This represents a 44% improvement over the baseline model that used mean climate predictors. Amplitude in both precipitation and temperature were typically the most important predictors for models in which they were included. The importance of S_T was greater than S_P in all cases, indicating that the coherence of warm/cool seasons were more important than coherent wet/dry seasons for predicting global fire activity. The best model, containing all of the non-redundant variables (S_P, S_T, D_P, D_T,$\bar{P}_L$,$\bar{P}_H$,$\bar{T}_L$,$\bar{T}_H$, $O_{P,\,T}$), predicted 87% of the global variability in fire activity (Fig. 2.5).

Table 2.1. Variable importance for different random forest models. Each row represents the results of a different random forest model built with the variables in occupied cells. Cell values indicate the normalized variable importance. The rightmost column (“score”) gives the proportion of variance (an analog to the R^2 value) on a test set that the model was not built with. From left to right the variables are precipitation seasonality index (S_P), duration of the dry season (D_P), precipitation amplitude (A_P), average dry season precipitation ($\bar{P}_L$), average wet season precipitation ($\bar{P}_H$), temperature seasonality index (S_T), duration of the cool season (D_T), temperature amplitude (A_T), average cool season temperature ($\bar{T}_L$), average warm season temperature ($\bar{T}_H$), and synchrony ($O_{P,T}$). The two most important variables for each model are highlighted in bold.

S_P	D_P	A_P	$\bar{P}_L$	$\bar{P}_H$	S_T	D_T	A_T	$\bar{T}_L$	$\bar{T}_H$	$O_{P,T}$	Score
	0.192					**0.573**				**0.234**	0.293
0.415					**0.464**					0.121	0.446
0.335	0.095				**0.371**	0.199					0.602
0.319	0.079				**0.344**	0.169				0.088	0.642
		0.396					**0.510**			0.095	0.663
0.189		**0.275**			0.203		**0.334**				0.712
0.170		**0.251**			0.172		**0.304**			0.103	0.793
	0.090	**0.341**				0.125	**0.444**				0.750
	0.068	**0.335**				0.104	**0.422**			0.072	0.769
0.334	0.096				**0.371**	0.199					0.602
0.318	0.080				**0.345**	0.169				0.088	0.644
0.128			0.193	**0.195**	0.126			**0.195**	0.162		0.816
0.109			**0.189**	**0.189**	0.110			0.177	0.142	0.084	0.852
0.103	0.079		**0.173**	**0.169**	0.105	0.094		0.154	0.123		0.866
0.099	0.065		**0.167**	**0.159**	0.097	0.085		0.146	0.121	0.060	0.870

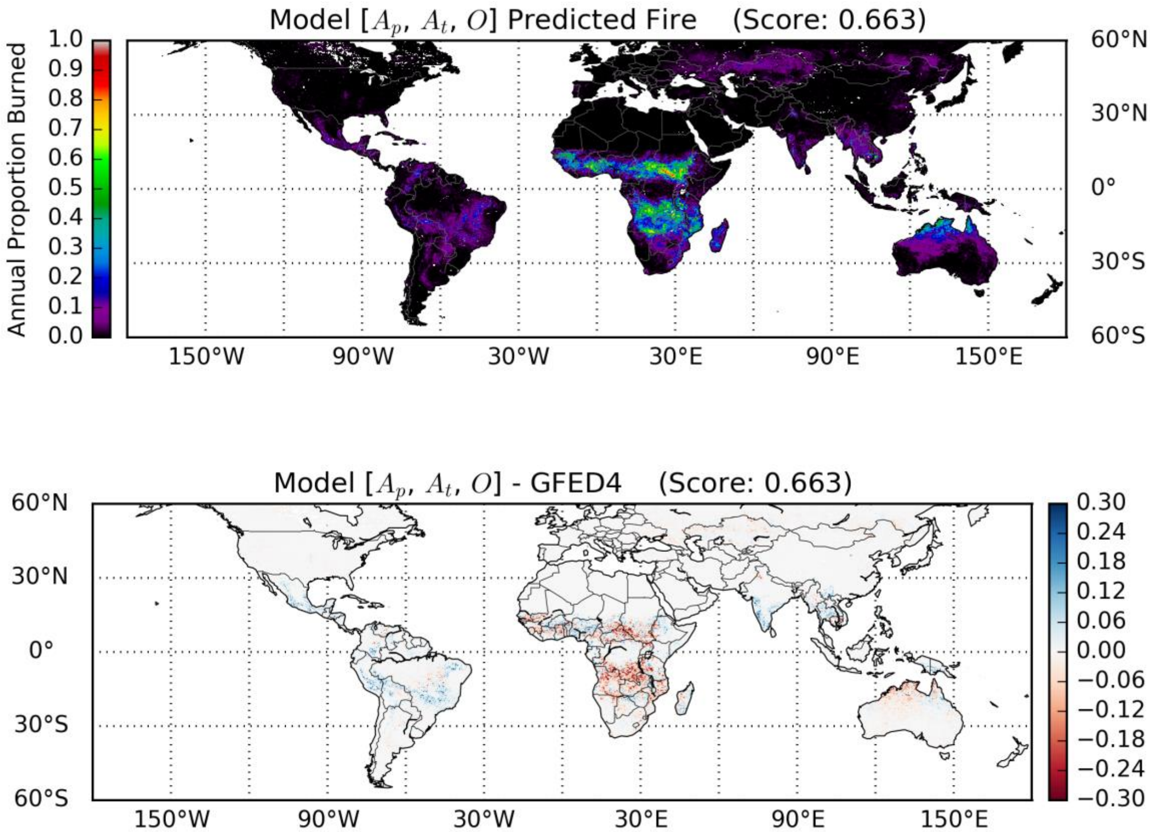

Figure 2.4. Predicted average proportion burned for a simple model (variables A_P, A_T, O; top panel), and the difference between these predictions and GFED4 data (bottom panel).

2.6 Discussion

2.6.1 Global Seasonality Metrics

The seasonality metrics capture known features of the climate system well. For example, monsoonal systems in Asia, Australia, West Africa and North America are visible in the global maps as spatially extended regions of high precipitation seasonality index and amplitude (Fig. 2.3c, g). Long dry and warm seasons are visible in the subtropical deserts (Fig. 2.3e, f). The expected out-of-phase nature of Mediterranean climates, with the warm season out of phase with the wet season, is captured in the synchrony maps. Large temperature amplitudes are also visible in high-latitudes (Fig. 2.3b). The partitioning technique accurately and parsimoniously describes seasonal climate features in a way that can easily be fed into a statistical model.

The predictive performance of the model compares favorably to previous empirical-statistical models of fire activity. For example, Bowman *et al.*, [2014] found that a linear model that includes wet and dry season rainfall amounts and an interaction term could explain 49% of the variability in tropical fire activity. However, linear models are restricted in the way in which they model the underlying relationship between predictors and fire activity. Archibald *et al.* [2009] used a random forests approach similar to ours to model spatially varying fire activity in southern Africa. Their study used a larger number of sophisticated natural and anthropogenic proxies of fuel load, fuel flammability, ignition frequency and fuel continuity (11 predictors in total) and they were able to explain 68% of the variance in regional burned area. However, a drawback of using more specific predictors when scaling up to a global level is the availability of these datasets on global basis. For example, datasets on road density, percentage of communal land and grazing intensity were only available at the regional level and would have to be compiled from multiple sources to achieve global coverage. Using my approach, the prediction of fire at the global scale does not require data inputs that may only be available on a regional basis. Instead, I only require gridded precipitation and temperature datasets, for which long term, global datasets are available.

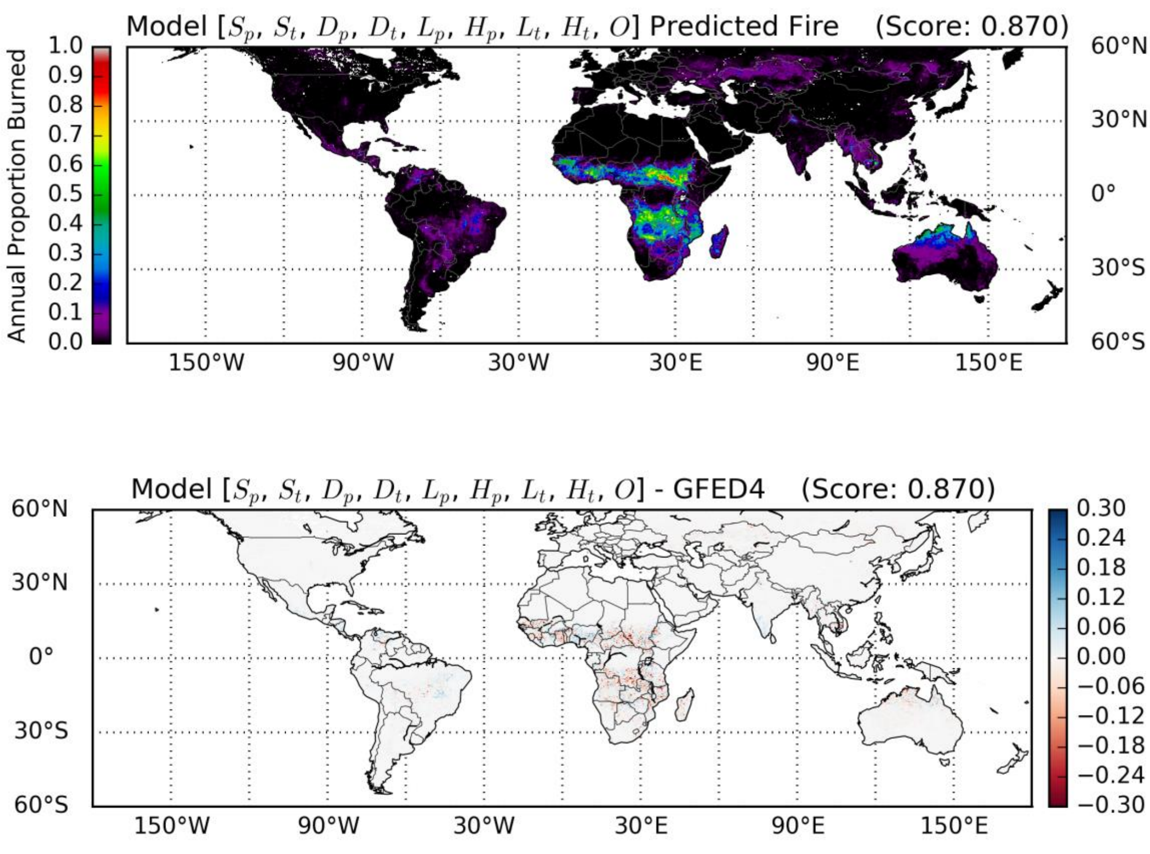

Figure 2.5. Predicted average proportion burned for a complex model (variables A_P, A_T, O; top panel), and the difference between these predictions and GFED4 data (bottom panel).

The current study represents a significant advance for two main reasons. First, the scope of my investigation on seasonality has been extended from the regional to the global scale. A global model requires predicting over many distinct biomes with different types of vegetation and varying levels of fire intensity and I still achieve high accuracy. Second, I can explain the large variations in fire activity using very simple models. For example, just three predictors: (A_T, A_P, and O) can explain a substantial portion of average global burned area (66%) and capture the main geographic features of global fire such as the zonal bands of high fire activity in Africa and Australia (Fig. 2.5a-b). A more complex model including 9 predictors offers exceptional global performance, predicting 87% of the variability in global fire (Fig. 2.6, Table 2.1). This model is accurate even in high fire regions in Africa (Fig 2.5b). While other factors such as human proximity and activity, biome type, vegetation cover, and ignition rates may enhance this predictability regionally, I have demonstrated that they are not necessary for explaining a majority of the spatial variability in global fire. Seasonality metrics – amplitude, duration, coherence, seasonal averages and synchrony –can be used by themselves to achieve high accuracy in global maps of fire activity. These metrics are both simple and descriptive of the known underlying biophysical causes of fire.

My study extends the work of other researchers who have connected seasonality metrics to fire activity on a regional basis. For example, Mondal & Sukumar [2016] found both wet and dry season rainfall to be important in explaining fire across a regional rainfall gradient. My model also identifies these two variables as the two most important variables on a global basis (Table 2.1). This has important implications for understanding the data requirements of fire forecasting under a changing climate. Wet and dry season rainfall offer the most predictive value of global fire activity and these variables must be accurately modeled for future fire regimes to be properly predicted. On the other hand, the duration variables that I considered generally offered the lowest predictive value. This is in contrast to past studies that have found duration variables that add substantial predictive value to a regional model (such as dry season duration as in Archibald *et al*. [2009]). This could indicate that results of models that incorporate variables such as length of wet/dry season, even if they achieve high accuracy in a specific region, may not be widely applicable to other regions. This also highlights the usefulness of the globally consistent approach that I take in this study.

The largest model bias is generally observed in the tropical regions with typically high fire activity, namely Africa and northern Australia (Fig. 2.4b, 2.5b). I offer two explanations for the underestimation of fire where fire frequency is the highest. The first is model dependent. Random forests generate predictions from known data and do not extrapolate estimates outside of the range of variables in the input (see, for example, Jeong *et al*. [2016]). This may affect the ability of the model to achieve high accuracy where fire is at the upper limit of the distribution of global observations. Another potential cause of the spatial clustering of lower-than expected burned area predictions in high fire regions may be region specific and involve the ecological legacy of fire on the land surface. There is evidence that the occurrence of certain biome types is driven by positive fire feedbacks, which can induce a hysteresis in the dependence between vegetation states and climatic variables [*Staver et al*., 2011]. I hypothesize that, because of such positive fire feedbacks, different vegetation types can exist in the same climate conditions and therefore vegetation types and the associated fire regimes cannot be deterministically predicted as a function of climatology. In these regions, the predictive capacity of the model tends to be the lowest. Future research will be needed to test whether the inclusion of historical fire or demographic variables would significantly improve the predictions in this region. Such evidence would support this hypothesis.

I now discuss some of the visualizations (Fig 2.6-2.9) that illustrate how the average fire activity (shading in figures) varies in a subset of data determined by average temperature and rainfall. The darkest pixels indicate higher fire activity relative to other pixels in the same climate. The position of these darker pixels within each panel can elucidate the relationship between seasonality metrics and fire activity for a given average climate. In line with expected biophysical controls on fire, both temperature and precipitation amplitude were positively related to fire activity in different regions (Fig. 2.6). Precipitation amplitude was positively related to fire activity in warmer regions, regardless of overall moisture status (Fig. 2.6e-f, g-i). These regions correspond to tropical and subtropical regions. This finding is consistent with my hypothesis that in warm, dry environments, a higher precipitation amplitude is more likely to result in a lifting of moisture-based constraints on productivity and fuel accumulation. In warm, wet regions the high amplitude implies drier conditions during some part of the year that lift fuel-moisture limitations on the ignition and spread of fire. At high average temperature and intermediate moisture (Fig. 2.6h), the climatic envelope is such that a range of precipitation amplitude values are sufficient to promote the seasonal cycle necessary for abundant fire. Indeed, high fire activity is more abundant overall and is observed over a larger range of amplitudes than in other regions (Fig. 2.6h). In cold climates, temperature amplitude is positively related to the fire activity over the whole moisture gradient. However, the range of temperature amplitudes observed in cold regions is low. This is consistent with a temperature constraint on fire in cold regions; for a given MAT, a larger temperature shift will result in a stronger warm season, potentially enhancing both growing season fuel accumulation and fire weather risk.

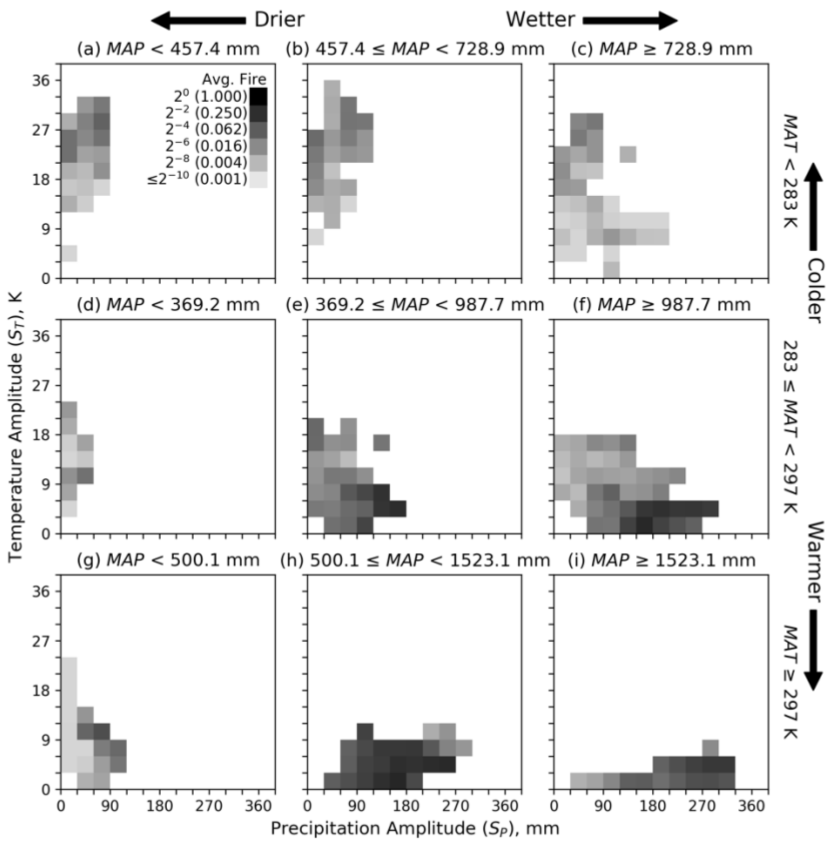

Figure 2.6. Average fire activity as a function of MAP, MAT, precipitation amplitude, and temperature amplitude. Global data are first divided into cold, mild and warm regions (left, middle and right panel, respectively), corresponding to the lower, middle and upper tertiles of the global distribution of MAT. Then I divided each of these samples into the lower, middle and upper tertiles of MAP, giving 9 sets of data all containing about the same number of pixels and corresponding to each panel. In each panel the data are further binned into 30 mm and 3 K precipitation and temperature and amplitude bins (horizontal and vertical axis, respectively) giving 13 bins along each axis. Shading depicts the average yearly proportion burned of all pixels in a given bin. Only the most populous bins that cumulatively represent more 95% of contributing pixels are shaded; excluded bins are shown in white. Note that the color scale is a logarithmic.

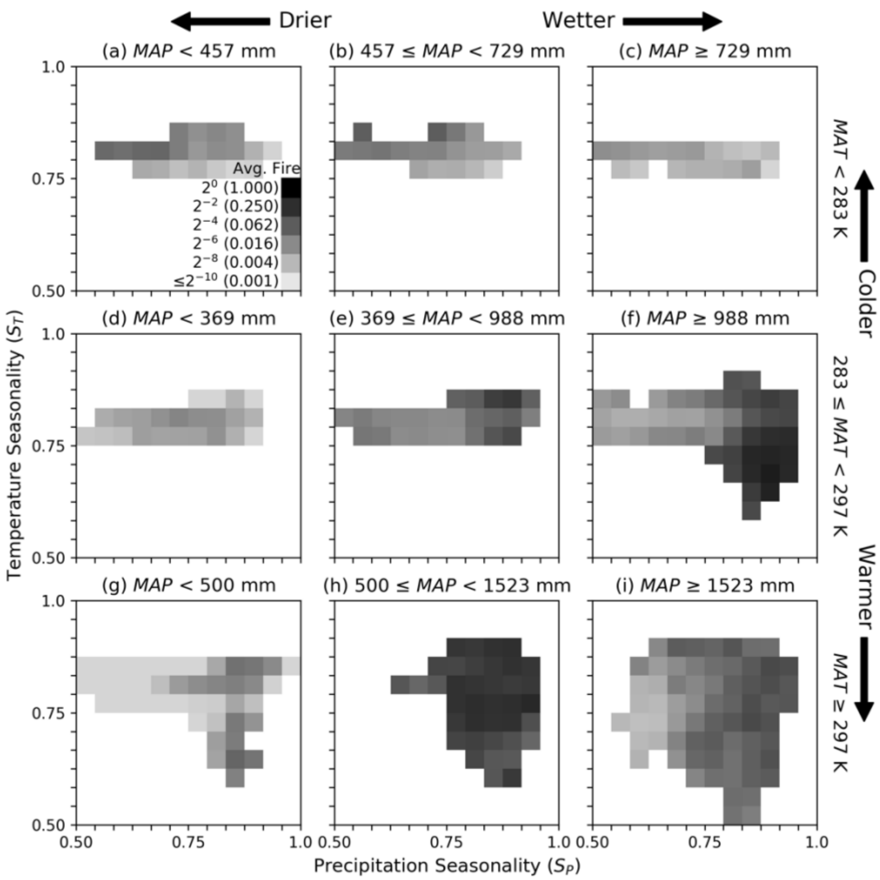

Figure 2.7. Average fire activity as a function of MAP, MAT, precipitation seasonality index, and temperature seasonality index. Global data are first divided into cold, mild and warm regions (top, middle and bottom panels, respectively), corresponding to the lower, middle and upper tertiles of the global distribution of MAT. Then I divided each of these samples into the lower, middle and upper tertiles of MAP, giving 9 sets of data all containing about the same number of pixels and corresponding to each panel. In each panel the data are further binned into 13 equally spaced temperature and precipitation seasonality index bins (horizontal and vertical axis, respectively). Shading depicts the average yearly proportion burned of all pixels in a given bin. Only the most populous bins that cumulatively represent more than 95% of contributing pixels are shaded; excluded bins are shown in white. Note that the color scale is logarithmic.

Locations with low within-season variability relative to total yearly variability (i.e. high seasonality) are expected to promote high fire activity due to a strong temporal partitioning between favorable growing and burning conditions. A positive relationship between high precipitation seasonality indices and fire is observed in all warm regions (Fig. 2.7d-i), particularly in fire prone-regions containing the highest absolute fire activity (Fig. 2.8f, h-i). This suggests that low within-season variability in precipitation promotes fire in warm and dry regions. In cold and dry regions, there is also a positive relationship between temperature seasonality (Fig. 2.9a-e; high relative fire activity is observed at the upper edge of respective climate envelopes). As with temperature amplitude, I infer a similar mechanism by which the lack of variability in the warm season is more favorable to either fuel accumulation or fuel curing because there is reduced risk of intermittent temperature limitations to these processes.

Synchrony is the total number of months of overlap between the respective low and high temperature and precipitation seasons. I hypothesized that in the subtropics where water is a potential limitation on plant growth, a wet season and warm season that are out of phase (i.e. low-synchrony) would increase average burned area due to temporal partitioning between the ideal cool, wet growing and warm dry burning seasons. The most fire prone regions show a preference for low overlap between the warm season and the wet season (i.e. $O_{P,T}$ is less than 6; Fig. 2.8f, h), partially confirming this hypothesis. The warmest, wettest regions do not exhibit a distinct difference in fire activity between high and low synchrony (Fig. 2.8i). This climate region corresponds to the wet tropical regions; I hypothesize that other factors have a stronger control on the average burned area in a given year. For example, climate oscillations such as ENSO are known to drive exceptional fire years in humid regions [*Tacconi et al.*, 2007]. I do not account for this type of interannual variability of climate variables with seasonality metrics.

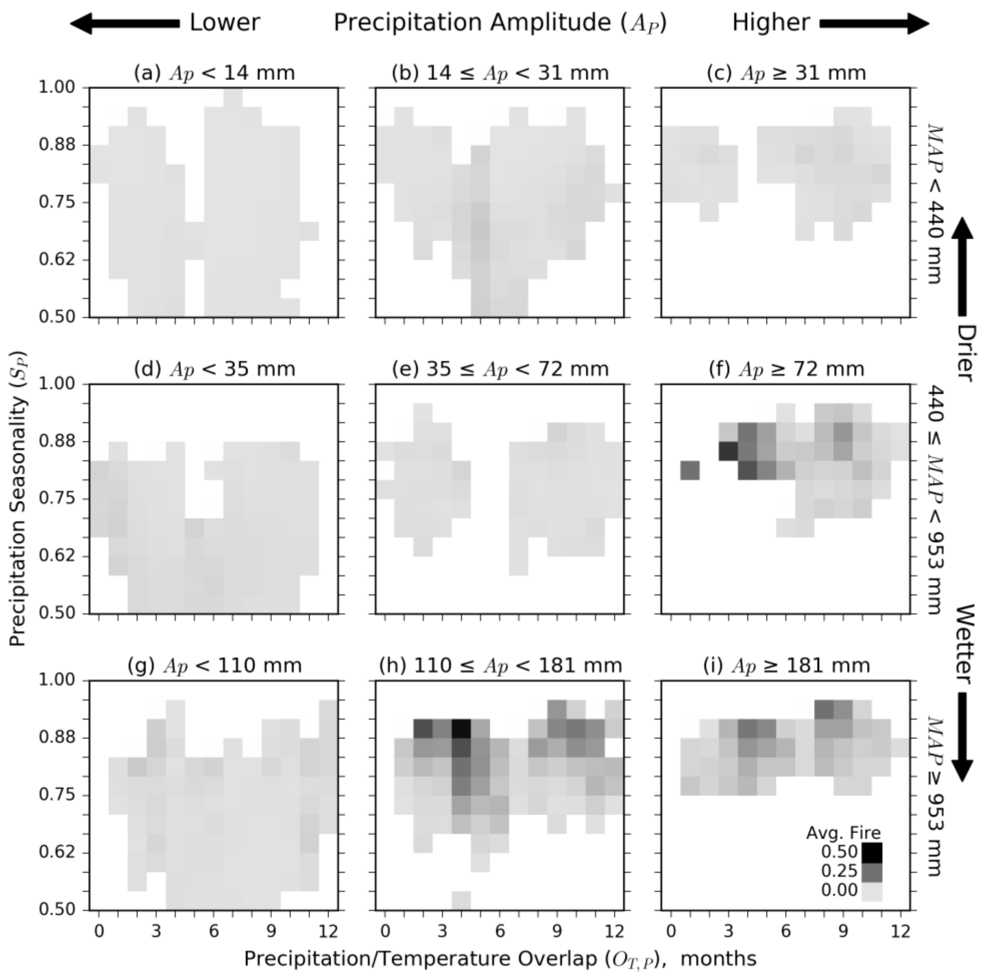

Figure 2.8. Average fire activity as a function of MAP, A_P, synchrony and precipitation seasonality index. Global data are first divided into arid, semiarid/sub-humid, and wet regions (top, middle and bottom panels, respectively), corresponding to the lower, middle and upper tertiles of the global distribution of MAP. Then I divided each of these samples into the lower, middle and upper tertiles of A_P, giving 9 sets of data all containing about the same number of pixels and corresponding to each panel. In each panel the data are further binned into 13 equally spaced synchrony and precipitation seasonality index bins (horizontal and vertical axis, respectively). Shading depicts the average yearly proportion burned of all pixels in a given bin. Only the most populous bins that cumulatively represent more than 95% of contributing pixels are shaded; excluded bins are shown in white.

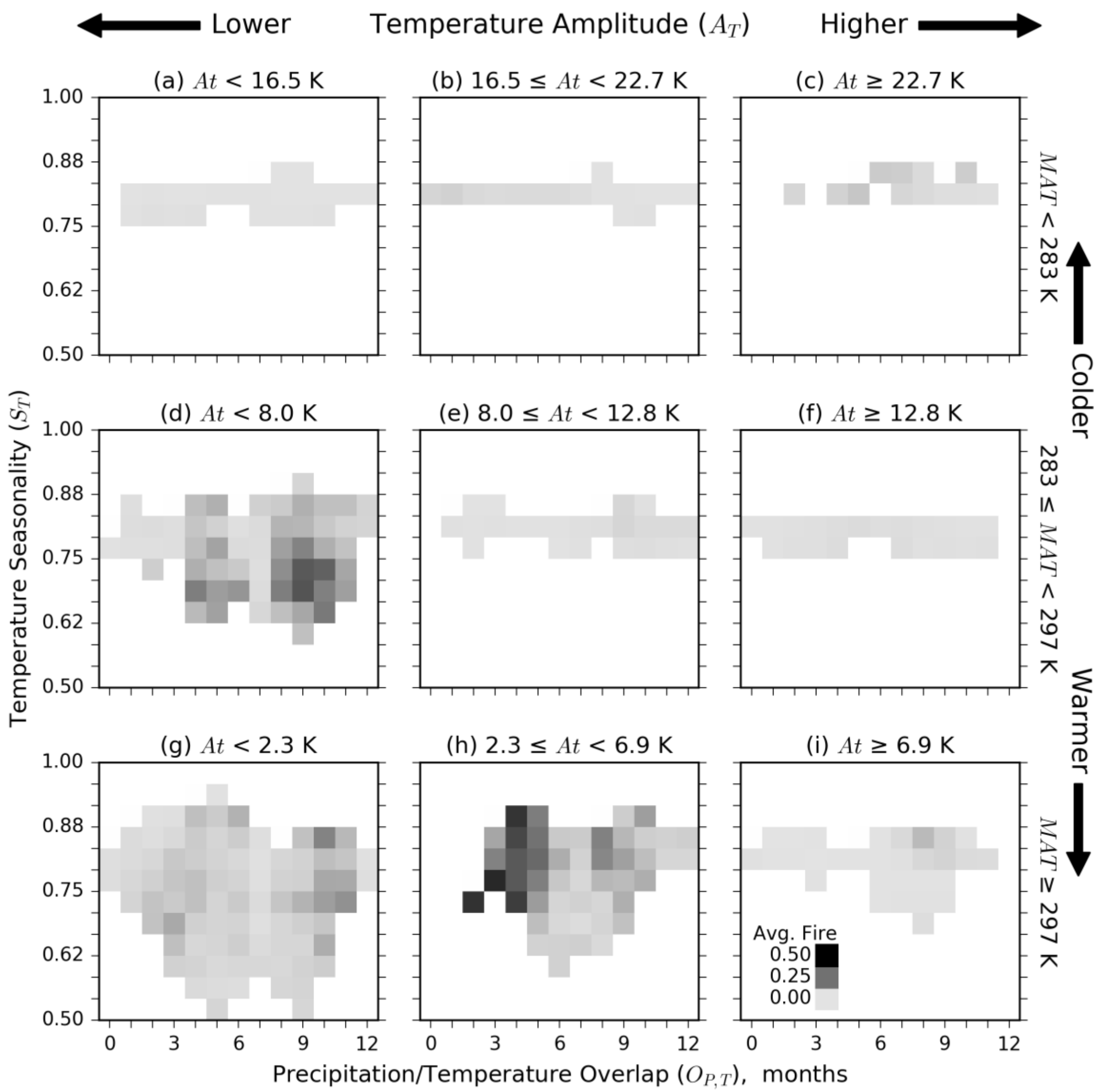

Figure 2.9. Average fire activity as a function of MAT, A_T, synchrony and temperature seasonality index. Global data are first divided into cold, mild and warm regions (top, middle and bottom panels, respectively), corresponding to the lower, middle and upper tertiles of the global distribution of MAT. Then I divided each of these samples into the lower, middle and upper tertiles of temperature amplitude (A_T), giving 9 sets of data all containing about the same number of pixels and corresponding to each panel. In each panel the data are further binned into 13 equally spaced synchrony and temperature seasonality index bins (horizontal and vertical axis, respectively). Shading depicts the average yearly proportion burned of all pixels in a given bin. Only the most populous bins that cumulatively represent more than 95% of contributing pixels are shaded; excluded bins are shown in white.

An exception to the positive A_T-fire and negative synchrony-fire relationships exists at moderate temperatures and low temperature amplitudes (Fig. 2.9d). These regions feature heavily in southern hemisphere subtropics (southern Africa, central America, and the Atlantic coastal forest in southeastern Brazil). However, because the precipitation tends to occur during the warm season, there may not be a long season that is truly favorable for fires in these climates. This may explain why low (<0.75) seasonality in temperature is positively associated with fire. In this case productivity and fuel accumulation could be enhanced if the variability of temperature within the warm season is high (i.e. S_T is low), leading to some periods when mild temperatures co-occur with rainfall. Similarly, during the cool, dry season fire may be enhanced if there is low coherence in the low temperature season and intermittent hot spells that increase chances of burning. However, this does not explain why fire shows a preference for high-synchrony regions in the first place. More work is needed to fully elucidate the underlying drivers.

The relationship between different seasonality metrics and fire activity is not clear in all regions (as in Fig. 2.9d discussed above). This could be due to regionally varying importance of anthropogenic or plant demographic factors in determining fire. Seasonal crop burning occurs in regions with certain seasonality characteristics, for example burning in regions with two wet seasons [*Korontzi et al*., 2006]. This has the potential to confound the climate-fire relationships I have described. Humans also suppress fire at scales large enough to impact regional pyrogeography [*Andela & Van der Werf*, 2014]. Further research must be done in order to contextualize my findings across diverse ecosystems and understand how climate and humans interact to promote novel fire regimes. Nevertheless, despite substantial spatial variability in the non-climatic drivers and constraints of fire, I can successfully model global spatial variability in fire activity using simple seasonality metrics.

Conclusion

I have shown a simple way to describe the seasonal cycle of climate variables that directly aids the prediction of global fire activity. These metrics are conceptually simple, can be applied to time-series of various resolution, and capture the salient climate features that are known to be important for fire prediction from a biophysical standpoint. Generally, more fire is observed where the seasonal amplitude is greater and where there is less intra-seasonal variability. My statistical models achieve high accuracy over a range of biomes and fire regimes with only a handful of predictors. While the purpose of this was to demonstrate the extent to which seasonality alone could predict fire, these new metrics may be combined with other predictors of fire activity (spread, ignitions, fire history, vegetation type, moisture status) to further improve prediction and mechanistic understanding of fire on a global basis. This methodology may be useful hindcasting fire based on station data or predicting novel fire regimes based on the output of global climate models.

References

Andela, N., & Van Der Werf, G. R. (2014). Recent trends in African fires driven by cropland expansion and El Nino to La Nina transition. *Nature Climate Change*, *4*(9), 791.

Archibald, S., Roy, D. P., Wilgen, B. V., W., & Scholes, R. J. (2009). What limits fire? An examination of drivers of burnt area in Southern Africa. *Global Change Biology*, *15*(3), 613-630.

Ashouri, H., Hsu, K. L., Sorooshian, S., Braithwaite, D. K., Knapp, K. R., Cecil, L. D., ... & Prat, O. P. (2015). PERSIANN-CDR: Daily precipitation climate data record from multisatellite observations for hydrological and climate studies. *Bulletin of the American Meteorological Society*, *96*(1), 69-83.

Bradstock, R. A. (2010). A biogeographic model of fire regimes in Australia: current and future implications. *Global Ecology and Biogeography*, *19*(2), 145-158.

Breiman, L. (2001). Random forests. *Machine Learning*, *45*(1), 5-32.

Bowman, D. M., & Johnston, F. H. (2005). Wildfire smoke, fire management, and human health. *EcoHealth*, *2*(1), 76-80.

Bowman, D. M., Murphy, B. P., Williamson, G. J., & Cochrane, M. A. (2014). Pyrogeographic models, feedbacks and the future of global fire regimes. *Global Ecology and Biogeography*, *23*(7), 821-824.

Fan, Y., & Van den Dool, H. (2008). A global monthly land surface air temperature analysis for 1948–present. *Journal of Geophysical Research: Atmospheres*, *113*(D1).

Hantson, S., Arneth, A., Harrison, S. P., Kelley, D. I., Prentice, I. C., Rabin, S. S., ... & Bachelet, D. (2016). The status and challenge of global fire modelling. *Biogeosciences*, *13*(11), 3359-3375.

Jeong, J. H. *et al*. (2016). Random forests for global and regional crop yield predictions. *PloS One*, *11*(6), e0156571.

Kaufman, Y. J., Tanré, D., & Boucher, O. (2002). A satellite view of aerosols in the climate system. *Nature*, *419*(6903), 215.

Korontzi, S., McCarty, J., Loboda, T., Kumar, S., & Justice, C. (2006). Global distribution of agricultural fires in croplands from 3 years of Moderate Resolution Imaging Spectroradiometer (MODIS) data. *Global Biogeochemical Cycles*, *20*(2).

Krawchuk, M. A., & Moritz, M. A. (2011). Constraints on global fire activity vary across a resource gradient. *Ecology*, *92*(1), 121-132.

Mondal, N., & Sukumar, R. (2016). Fires in seasonally dry tropical forest: testing the varying constraints hypothesis across a regional rainfall gradient. *PloS one*, *11*(7), e0159691.

Pausas, J. G., & Ribeiro, E. (2013). The global fire–productivity relationship. *Global Ecology and Biogeography*, *22*(6), 728-736.

Randerson, J. T., Chen, Y., Werf, G. R., Rogers, B. M., & Morton, D. C. (2012). Global burned area and biomass burning emissions from small fires. *Journal of Geophysical Research: Biogeosciences*, *117*(G4).

Schultz, M. G., Heil, A., Hoelzemann, J. J., Spessa, A., Thonicke, K., Goldammer, J. G., ... & van Het Bolscher, M. (2008). Global wildland fire emissions from 1960 to 2000. *Global Biogeochemical Cycles*, *22*(2).

Staver, A. C., Archibald, S., & Levin, S. A. (2011). The global extent and determinants of savanna and forest as alternative biome states. *Science*, *334*(6053), 230-232.

Tacconi, L., Moore, P. F., & Kaimowitz, D. (2007). Fires in tropical forests–what is really the problem? Lessons from Indonesia. *Mitigation and Adaptation Strategies for Global Change*, *12*(1), 55-66.

Tosca, M. G., Diner, D. J., Garay, M. J., & Kalashnikova, O. V. (2014). Observational evidence of fire-driven reduction of cloud fraction in tropical Africa. *Journal of Geophysical Research: Atmospheres*, *119*(13), 8418-8432.

Van Der Werf, G. R., Randerson, J. T., Giglio, L., Gobron, N., & Dolman, A. J. (2008). Climate controls on the variability of fires in the tropics and subtropics. *Global Biogeochemical Cycles*, *22*(3).

Chapter Three

Suppression of Rainfall by Fires in African Drylands

I bless the rains down in Africa

Toto

Substantial parts of this Chapter are published as

Saha, M. V., Scanlon, T. M., & D'Odorico, P. (2016). Suppression of rainfall by fires in African drylands. *Geophysical Research Letters*, *43*(16), 8527-8533.

3.1 Abstract

Fire is a widespread agent of disturbance in African drylands, but the impact of fire on local precipitation remains poorly understood and large-scale observational evidence has been lacking. Here I link fire to a reduction in precipitation across African drylands. Using 15 years of satellite observations over continental sub-Saharan Africa, I find that more extensive and later dry season fires lead to wet season rainfall deficits of up to 30 mm (~10%). The effect is stronger in the southern hemisphere, a signal I attribute to the later timing of fires in the dry season. Given the coupling between rainfall, fuel loads and fire in African drylands, a negative interannual feedback may arise between fire and precipitation, whereby fires suppress precipitation, thereby reducing fuel load and fire in the subsequent season. The reduced fuel load would, in turn, increase precipitation, completing the feedback loop. This feedback may contribute to a pervasive negative autocorrelation observed in southern hemisphere annual rainfall.

3.2 Introduction

Fire is a ubiquitous component of the biosphere, burning up to 350 Mha annually [*Flannigan et al.*, 2009]. It is especially prevalent in Africa, with up to 9% of the continent burnt on an annual basis [*Barbosa et al.*, 1999]. Previous research has characterized the role of fires as determinants of plant community composition [*Lehmann et al.*, 2014], cloud microphysical processes [*Rosenfeld et al.*, 2008] and surface energy and moisture budgets [*Beringer et al.*, 2015], but possible rainfall modification at seasonal timescales is not well understood. Smoke aerosols from fires can inhibit rainfall [*Rosenfeld et al.*, 2008; *Tosca et al.*, 2015]. Wet season rainfall may be impacted by aerosols from late-dry season fires that are burning as the wet season starts. However, the lifetime of aerosols varies from days to weeks, and aerosols may be advected away from the source site, limiting their long-term effect (e.g., the whole wet season). The impact of fire on the land surface is potentially important. By modifying vegetation [*Montes-Helu et al.*, 2009; *Beringer et al.*, 2015], albedo [*Veraverbeke et al.*, 2012] and the partitioning of net radiation into sensible and latent heat fluxes [*Wendt et al.*, 2007; *Montes-Helu et al.*, 2009; *Beringer et al.*, 2015], fire has the potential to mediate land-atmosphere feedbacks ranging from local to continental scales [*Görgen et al.*, 2006; *Findell et al.*, 2011; *Beringer et al.*, 2015; *De Sales et al.*, 2016]. After fire, increased sensible heat fluxes may enhance atmospheric instability and promote the triggering of convective rainfall [*Wendt et al.*, 2007; *Beringer et al.*, 2015]. Spatial patterning in burn scars may further enhance rainfall by promoting mesoscale convergence over burnt patches [*Wendt et al.*, 2007; *Beringer et al.*, 2015]. On the other hand, persistent reductions in soil moisture [*Snyman*, 2003], evapotranspiration [*Montes-Helu et al.*, 2009, *Beringer et al.*, 2015] and net radiation due to increased albedo [*Veraverbeke et al.*, 2012] may result in a drier, more stable planetary boundary layer that suppresses convective precipitation [*De Sales et al.*, 2016].

There have been limited efforts to quantify the impact of fire on wet season rainfall [*Görgen et al.*, 2006; *Lynch et al.*, 2007; *Notaro et al.*, 2011; *De Sales et al.*, 2016; *Hernandez et al.*, 2015]. These studies have relied on coupled land-atmosphere models and largely focus on regional changes in precipitation associated with the evolution of the monsoon. The sign and strength of the fire-rainfall relationship differs considerably across studies, and observational evidence in support of modeled results is lacking. For example, a modelling experiment of northern Australian fires reports a pre-monsoonal precipitation increase of 2.1 mm day^{-1} due to widespread and intense wildfires [*Görgen et al.*, 2006]. However, another study over the same region but using a different modelling approach reports a significant 0.5 mm day^{-1} decrease in pre-monsoonal precipitation [*Notaro et al.*, 2011]. Similarly, a modeling experiment focusing on West Africa showed that fire strengthens atmospheric subsidence by increasing albedo and reducing net radiation, leading to a 3% reduction in wet season precipitation [*De Sales et al.*, 2016]. A case study [*Hernandez et al.*, 2015] of local changes in precipitation after extensive wildfires in Portugal is less conclusive, showing either enhancement or suppression depending on the representation of rainfall processes in the model. The strength of land-atmosphere coupling varies geographically and discrepancies in modeled fire-rainfall relationships may be due in part to differing locations of study sites [*Guillod et al.*, 2015].

I investigate the relationship between dry season fires and subsequent rainfall using over a decade of satellite data from sub-Saharan Africa. In particular I assess how the timing and amount of fire relates to total wet-season precipitation (P_{WS}), which integrates both short-term effects (e.g., aerosol from late dry-season fires) and longer-lived modifications (e.g., albedo changes) to the land surface. I hypothesize that the timing of fire is especially important in governing the strength of land-atmosphere interactions; fires in the late dry season are to be more intense [*Govender et al.*, 2006] and there is less time for recovery from land surface modification before the onset of the wet season.

3.3 Data and Methods

3.3.1 Domain

I focus on dryland areas of continental Africa below 20° N (excluding the Saharan desert, Northern Africa, and Madagascar). I define drylands as regions with mean annual precipitation (MAP) between 300 mm and 1000 mm, including arid, semi-arid and dry sub-humid regions. I perform all analyses at 0.25°, the original resolution of the rainfall dataset. Data were acquired from April 2000 through December 2015.

3.3.2 Precipitation Data

Rainfall retrievals from the Tropical Rainfall Measuring Mission 3B42 (TRMM) data set are used [*Huffman et al.*, 2007]. These data are derived from merged satellite and gauge rainfall data. The wet season, which is distinct for each pixel, is defined as the minimal consecutive time period during which 95% of total annual rainfall occurs, on average (Fig. 3.1). Daily rainfall is then summed over the wet season to achieve a single rainfall value (the variable P_{WS}) for each year. The dry season is defined as the period of time between each wet season.

3.3.3 Fire Data

The Moderate Resolution Spectroradiometer (MODIS) Burned Area Product (MCD45A1, version 5.1) was used to build a daily fire dataset [*Roy et al.*, 2008]. The MODIS dataset provides daily estimates of whether each 500 m pixel has burned or not. For each day of the record, I calculated the fraction of burned 500 m MODIS cells whose centroid was within the larger 0.25°x0.25° TRMM pixel to obtain a single value of daily fire activity, proportion burned, at the same spatial scale as rainfall data. I then calculated the total dry season proportion burned by aggregating daily proportion burned from the start of each dry season to the start of the following wet season.

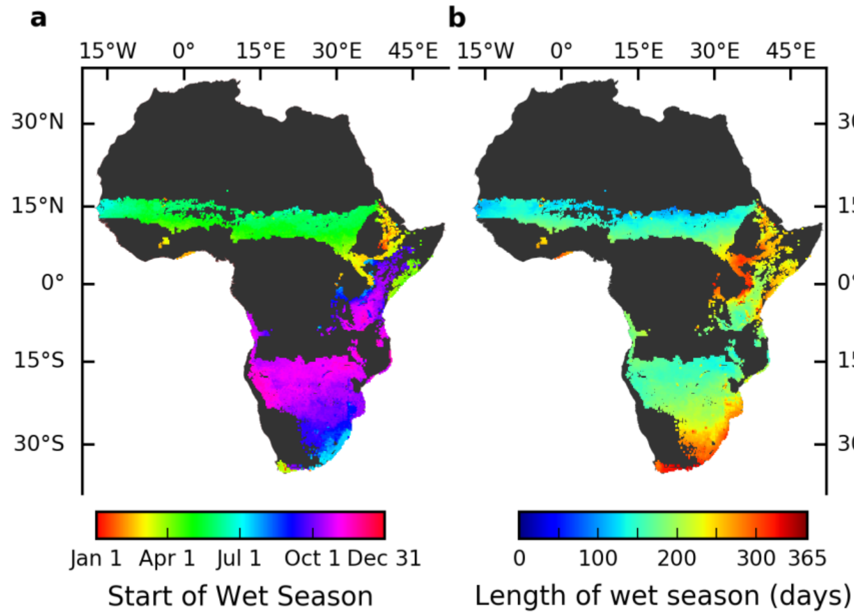

Figure 3.1. (**a**) The start of the wet season across the study region. (**b**) The length of the wet season across the study region. Excluded regions are shown in dark grey (see Methods).

I hypothesized that the amount and timing of fire could potentially impact rainfall. For each pixel and year, I calculated the total proportion of pixel area burned during the early and late dry season (which I call F_E and F_L, respectively). Here, early and late are defined as more than or less than 94 days before the wet season, where 94 days before the wet season is the average timing of fire across the whole domain. I chose to account for the timing of fire implicitly (i.e. by stratifying total fire into early and late) rather than explicitly (e.g. calculating the average day the dry season on which fire was sensed) because the latter variable is undefined for dry seasons with no fires. I excluded seasons when any fire data was unavailable during the dry season. Most notably, missing MODIS data for May and July 2001 resulted in missing fire values for large parts of the southern hemisphere, resulting in 14, instead of 15 years of data. The northern hemisphere was largely unaffected due to the differing timing of the northern hemisphere dry season.

3.3.4 Statistical Analysis

I investigate the relationship between fire and subsequent rainfall using generalized additive models (GAMs), a flexible statistical framework that allows for modeling highly nonlinear relationships [*Friedman et al.*, 2001; *Wood*, 2006]. Here, seasonal rainfall is modeled as a smooth, but otherwise unspecified, function of one or more covariates. My interpretation of model structure can be found in Appendix One. I fit P_{WS} (yearly values) as a smooth function of the average wet season precipitation. This effectively removes the climatic trend from the spatially pooled yearly rainfall data, leaving interannual variability (anomaly) at each pixel to be explained by other predictor variables. I also included a bivariate smooth of MAP and each fire variable, hypothesizing that the possible fire-rainfall interactions will vary across climate zones. All model terms were significant ($P<0.0001$). I compared this model to a null model without F_E and F_L terms (details given in supplementary information), which justified the inclusion of fire variables as covariates in the model. In Figure 3.2 I explore how modeled P_{WS} responds to differing levels of F_E and F_L when MAP is 400 mm. The response surface 900 mm MAP is shown in Figure 3.3. In Figure 3.4 I generate predictions of the average effect of fire on rainfall using temporally averaged values of F_E and F_L for each pixel.

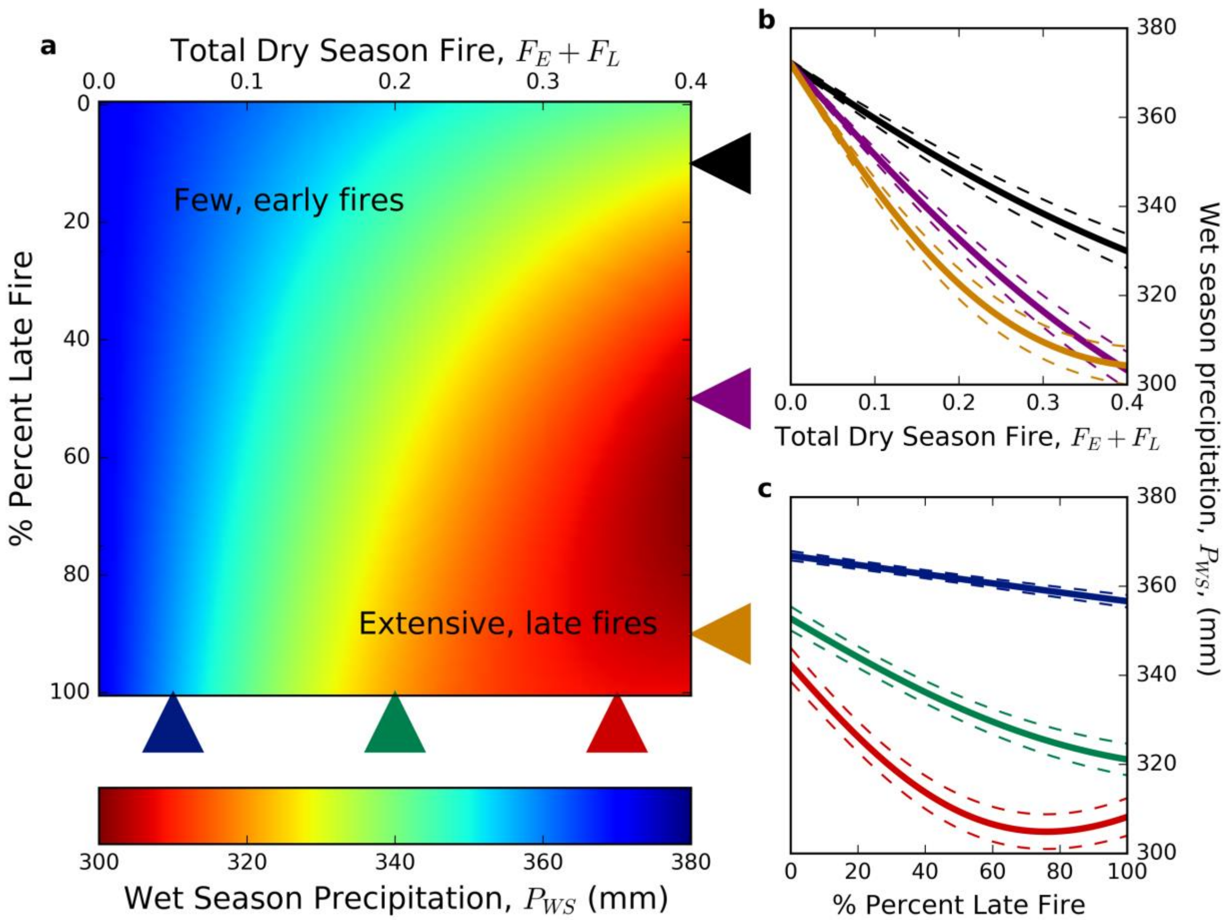

Figure 3.2. The relationship between fire timing, fire extent and wet season rainfall. **(a)** P_{WS} as a function of total dry season fire (F_{Total}) and percent of fire that is late (% F_L) calculated for 400 mm MAP. By definition, the average amount of wet season rainfall for a given pixel is about 95% of MAP. There are substantial deficits when late (high % F_L) and extensive (high F_{Total}) dry season fires occur. **(b)** Cross-sections of plot **(a)** at different levels of % F_L. Line color refers to % F_L values indicated by the triangles on the right margin of **(a)**. **(c)** Cross-sections of plot **(a)** at different levels of F_E+F_L. Line color refers to F_{Total} values of colored triangles on the bottom margin of **(a)**. Dotted lines in **(b)** and **(c)** depict 1-standard error confidence intervals.

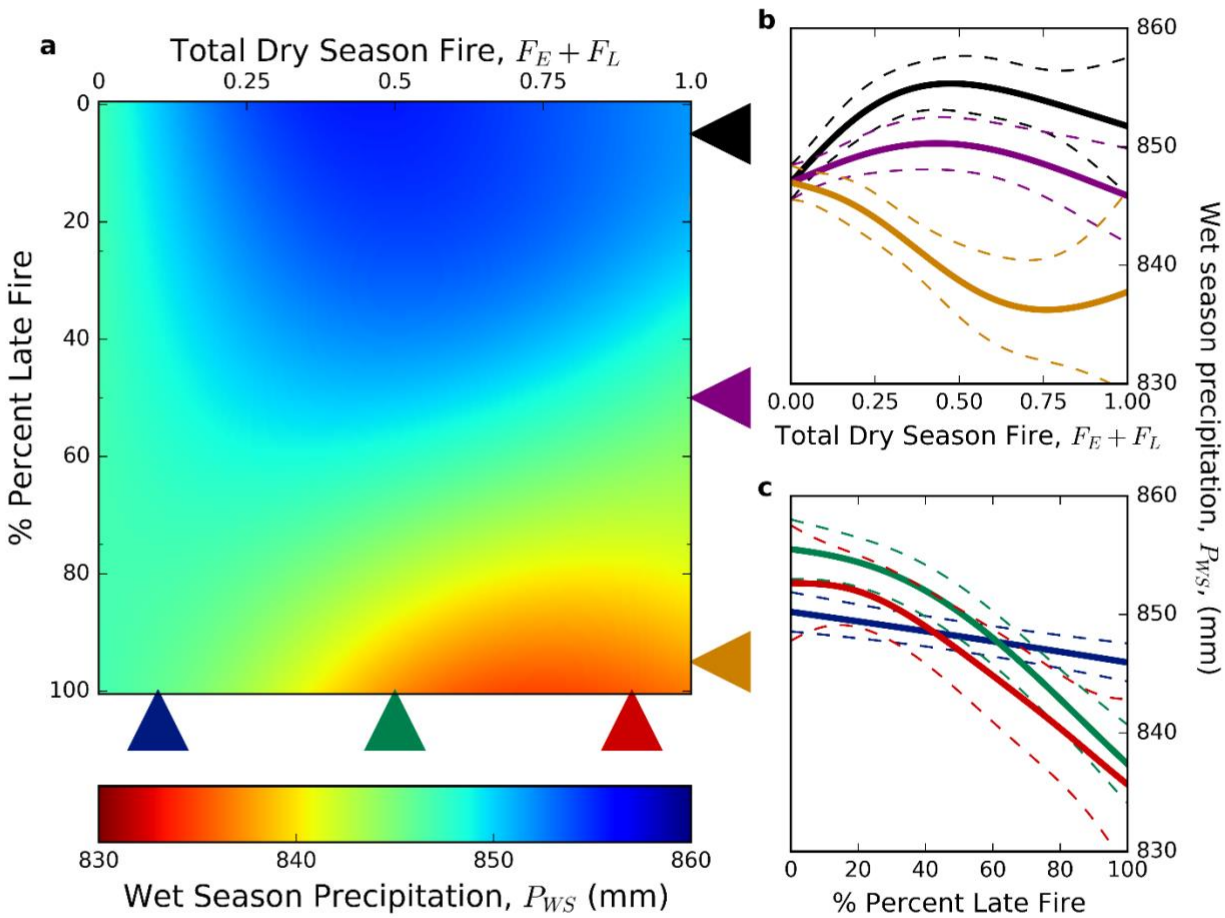

Figure 3.3. (a) P_{WS} as a function of total dry season fire (F_{Total}) and percent of fire that is late (% F_L) calculated for 900 mm MAP. There are substantial deficits when late (high % F_L) and extensive (high F_{Total}) dry season fires occur. **(b)** Cross-sections of plot **(a)** at different levels of % F_L. Line color refers to % F_L values indicated by the triangles on the right margin of **(a)**. **(c)** Cross-sections of plot **(a)** at different levels of F_E+F_L. Line color refers to F_{Total} values of colored triangles on the bottom margin of **(a)**. Dotted lines in **(a)** and **(b)** depict 1-standard error confidence intervals.

3.4 Results and Discussion

I find a significant statistical relationship between fire and subsequent rainfall for both fire variables (F-test, F statistics: F_E=8.48, F_L=30.71, $P<0.0001$). Wet season precipitation decreases as the amount of fire increases and as the percentage of late fire increases (Fig. 3.2).

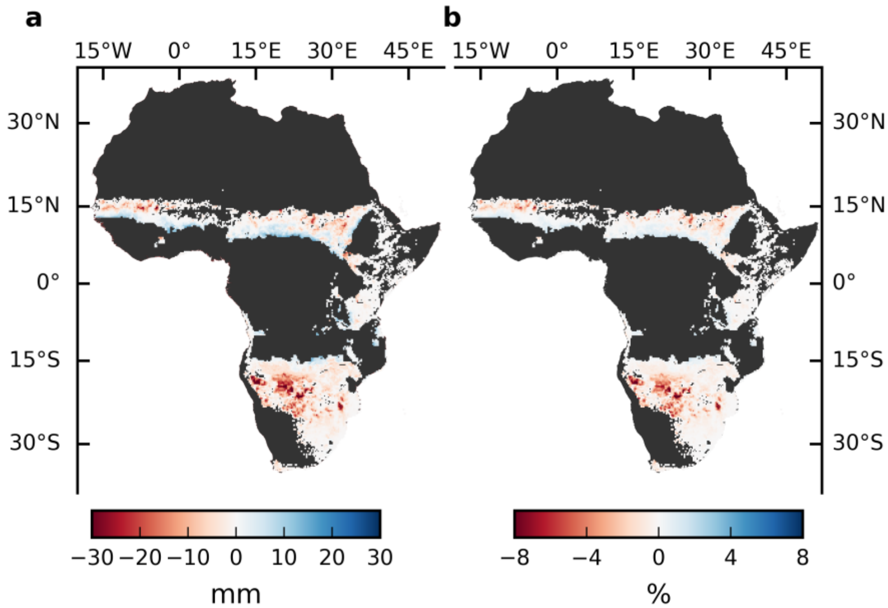

Figure 3.4. Fire-induced rainfall suppression in drylands. Rainfall change under average fire conditions for each pixel. (**a)** Rainfall lost is computed at each pixel as the difference between modeled wet season rainfall for temporally averaged F_E and F_L and modeled wet season rainfall with no fire. (**b)** Rainfall modification as in (a) but expressed as a percentage of MAP.

There is a nonlinear relationship with amount and timing of fire, with the largest rainfall deficits produced by a combination of more extensive and later fires. F_L was strongly associated with subsequent rainfall deficits across all values of MAP. The relationship between F_E and rainfall is more complex, shifting from strongly negative at low MAP to slightly positive at 900 mm MAP (Fig. 3.1). In Fig. 3.4 I quantify average rainfall lost as the difference between modeled rainfall under average fire conditions and modeled rainfall when F_E and F_L are set to 0. Using the model to generate estimates of fire-induced rainfall changes under average conditions identifies large regions of the southern hemisphere where fire reduces rainfall in the subsequent wet season (Fig. 3.4). However, this effect is subdued in the northern hemisphere. This can be attributed to the timing of fire in the northern hemisphere, which tends to occur early in the dry season (Fig 3.5a-b). This demonstrates the importance of fire timing on explaining hemispherical differences in rainfall suppression between hemispheres, despite their similar total burned area.

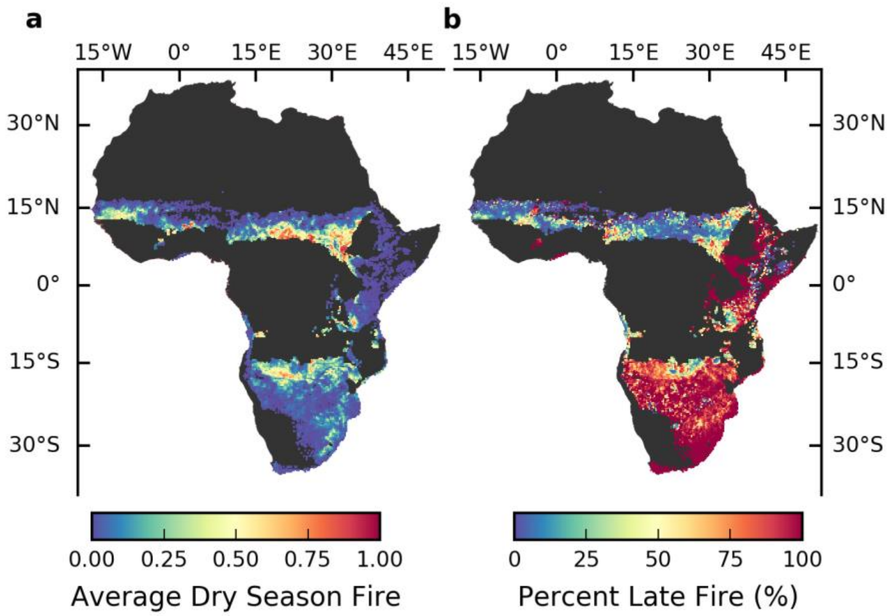

Figure 3.5. (**a**) Average amount of total dry season fire ($F_E + F_L$) across the domain. (**b**) Average proportion of fire that is late, computed as $\langle F_L \rangle / (\langle F_L \rangle + \langle F_E \rangle)$, where <> denote temporal averages using all available years of data.

The overall negative relationship between fire and rainfall is consistent with several possible mechanisms of rainfall modification proposed in the literature. The observed rainfall deficits could result from altered moisture dynamics at the land surface. Previous research has shown consistent decreases in latent heat flux after fire, which may last on the order of months [*Beringer et al.*, 2015]. These changes may have regional consequences for the formation of rainfall [*Findell et al.*, 2011]. Furthermore, fire induces significant soil moisture deficits that can last for more than a wet season [*Snyman*, 2003]. This is caused by lower infiltration, increased runoff and potentially higher bare soil evaporation over burn scars. That negative temporal anomalies in soil moisture contribute to reduced convective rainfall at the mesoscale has been demonstrated on a global basis, with strong observed effects in semiarid regions of Africa [*Guillod et al.*, 2015]. Alternatively, feedbacks associated with increased albedo have been implicated as a cause of reduced precipitation at a variety of scales [*Charney et al.*, 1975; *Meng et al.*, 2014]. In this scenario the exposure of dry soils after vegetation is removed by fire leads to increased albedo, decreased net radiation and total heat flux into the atmosphere and a less energetic planetary boundary layer that inhibits convective processes, a finding supported by modelling [*De Sales et al.*, 2016]. Evidence of long-term brightening has been found over semiarid burn scars but is dependent on the timing of fire and underlying soils [*Veraverbeke et al.*, 2012; *Gatebe et al.*, 2014]. Overall, studies reporting modeled rainfall reductions after fire suggest that the net effect of fire is a drier, more stable planetary boundary layer with stronger atmospheric subsidence and reduced moisture flux convergence [*Notaro et al.*, 2011; *De Sales et al.*, 2016]. Indirect mechanisms may also play a role in maintaining or amplifying early wet season rainfall deficits. Once a rainfall deficit is established early in the wet season, internal positive temporal feedbacks between soil moisture and precipitation may allow anomalies to persist even after the land surface has recovered to pre-fire conditions [*D'Odorico and Porporato* 2004; *Guillod et al.*, 2015].

The role of fire in rainfall-generating processes depends on the location along a climatic moisture gradient. While the major effect of fire was a reduction in P_{WS}, I observed slightly increased rainfall associated with high F_E in the wettest regions of the study domain (Fig. 3.3, light blue areas in Fig.3.4). As the limitation on convective rainfall transitions from moisture at low MAP to energy limitation at higher MAP [*Seneviratne et al.*, 2010], mesoscale features formed by moderate levels of fire disturbance may enhance rainfall [*Katul et al.*, 2012; *Lawrence & Vandecar*., 2015]. In these regions the timing of the disturbance is important, as there is still a negative relationship between F_L and P_{WS}. The importance of fire in promoting these land surface feedbacks is that persistent land surface modification is spatially fixed, allowing rainfall deficits to accumulate over the whole wet season at a single location. This is in contrast to the negative spatial soil moisture feedback that tends to homogenize moisture at the land surface over the course of multiple storms [*Guillod et al.*, 2015].

Incorporating a well-described link between rainfall and subsequent fire in drylands - fuel limitation - has the potential to contribute to a biennial oscillation in rainfall (Fig 3.6). Fire in drylands is limited by plant productivity through fuel limitation, which in turn is controlled by rainfall [*Andela et al*., 2013; *Fensholt et al*., 2012; *Zhu and Southworth*, 2013]. When ignitions do not limit fire, rainfall positively correlates with fire in the following dry season [*Van der Werf et al.*, 2008; *Archibald et al.*, 2009]. I find strong evidence of this fuel limitation in drylands, in line with previous studies. More than 60% of drylands exhibit a positive correlation between wet season rainfall and fire the very next year. Over 40% of these correlations exceed 0.2 (compared to about 18% of pixels with Pearson correlation coefficients lower than -0.2, Fig. 3.6a).

The new evidence of fire-induced rainfall suppression completes this feedback loop (Fig. 3.6b & d), whereby a high rainfall year is more likely to be followed by an extensively burned landscape in the dry season and a low rainfall in the following wet season. The lower rainfall subsequently reduces fuel loads and the occurrence of fire, representing a fire-mediated negative feedback on rainfall anomalies. A strong enough relationship along each leg of the proposed feedback would lead to an oscillation between low and high rainfall years, measured statistically as a negative autocorrelation in P_{WS}.

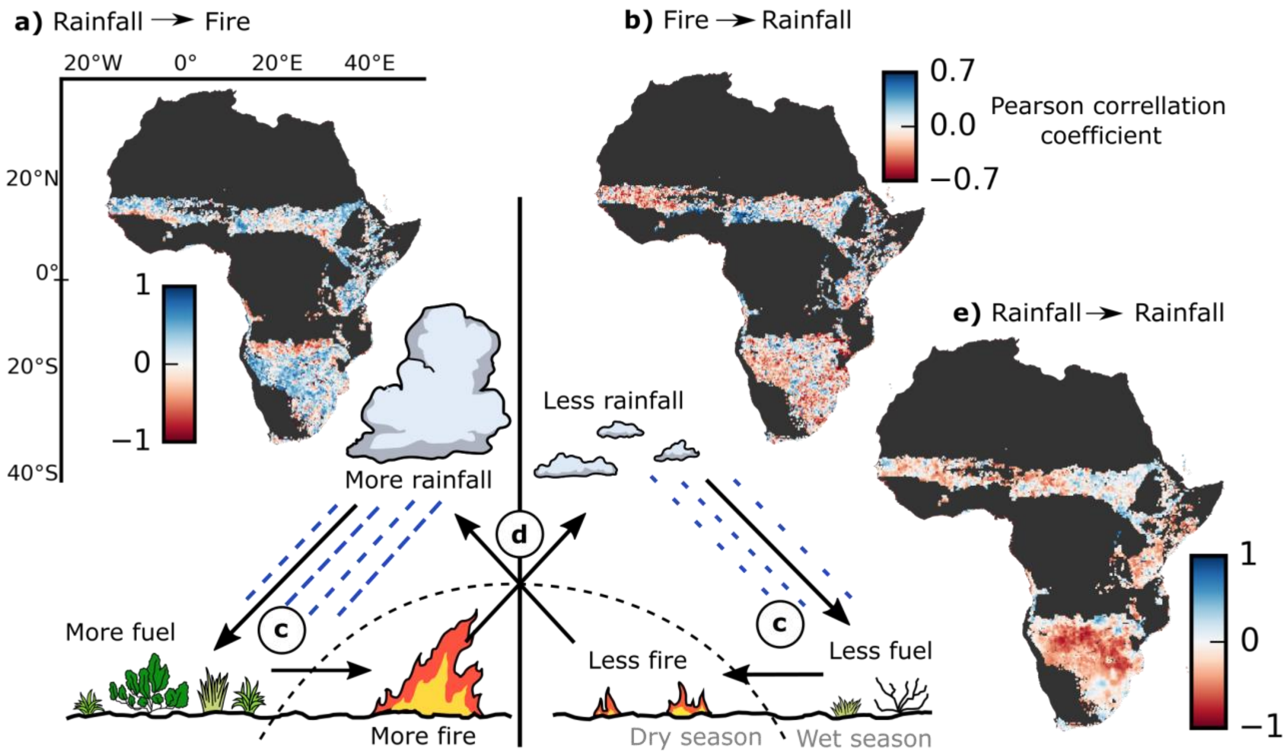

Figure 3.6. A proposed fire-rainfall feedback**. (a**) Pearson correlation coefficient of wet season rainfall and following dry season fire in drylands. Cool colors are indicative of a fuel limitation on a year-to-year basis. Excluded regions are shown in dark gray (see Methods). (**b**) Pearson correlation between dry season fire and following wet season rainfall. Warm colors represent fire suppression of wet season rainfall. The central conceptual diagram outlines a possible fire-rainfall feedback. The dotted line represents the temporal transition between the dry and wet seasons. (**c**) High rainfall increases fuel loads and subsequent fires, whereas low rainfall decreases fuel accumulation and subsequent fires. (**d**) Low fire activity results in more rainfall the next wet season, while extensive fire leads to less rainfall. (**e**) Lag-1 autocorrelation in total wet season rainfall. A biennial oscillation, detected as a negative autocorrelation (shown here in warm colors), could be caused by the proposed feedback.

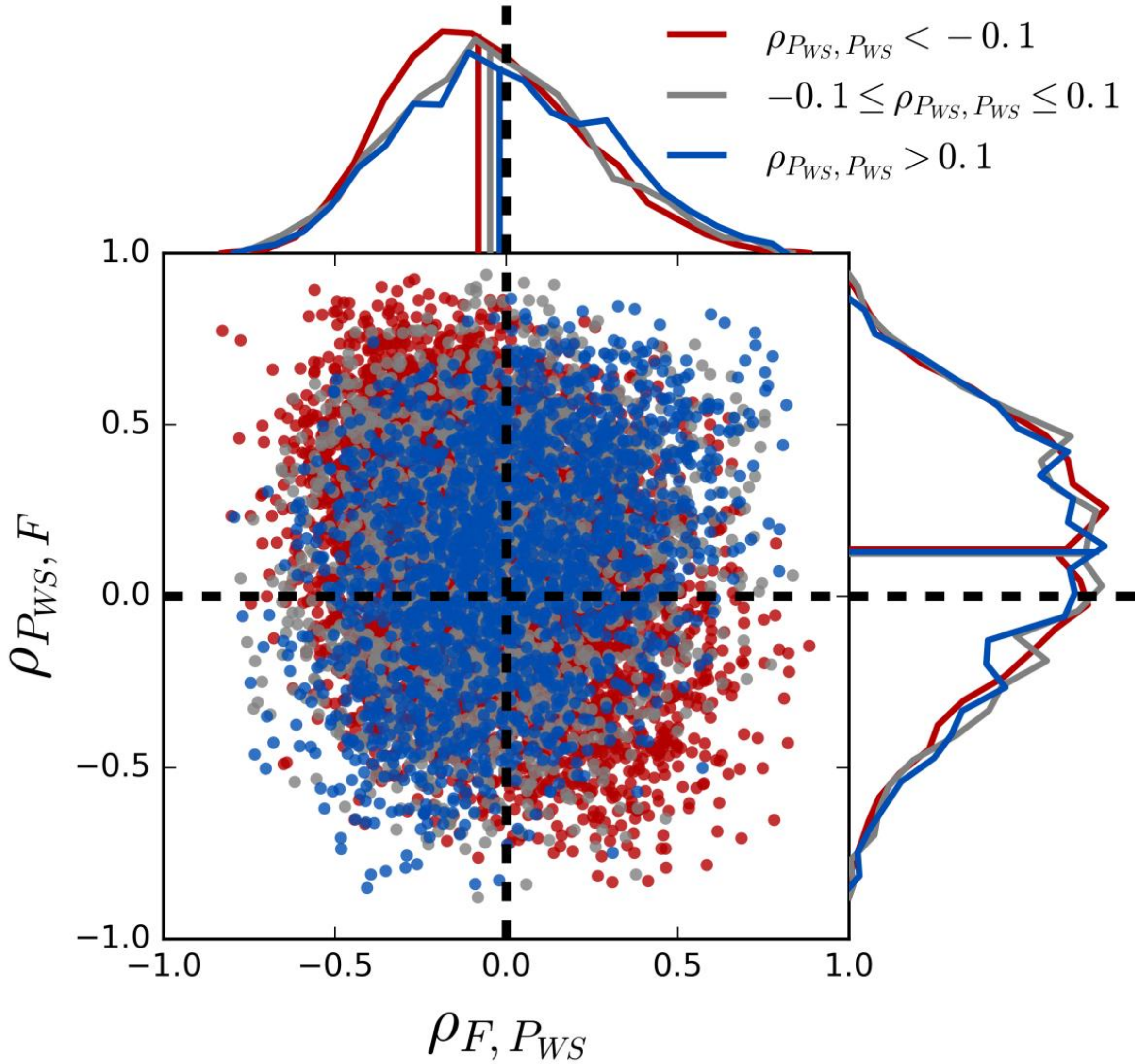

Figure 3.7. Dependence of yearly autocorrelation in rainfall on observed fire-rainfall relationships. Distribution of negative (red), neutral (gray) and positive (blue) yearly autocorrelation in P_{WS} for all pixels as a function of the Pearson correlation between fire and subsequent rainfall (ρ_{FPws}), and rainfall and subsequent fire ($\rho_{Pws,F}$). Normalized marginal histograms are depicted on axes margins. Colored lines in the marginal distributions indicate the distribution median. Negative autocorrelation in wet season rainfall tends to occur in regions where there is both a positive correlation between rainfall and subsequent fire (positive ρ_{PwsF}) and a negative correlation between fire and subsequent rainfall (negative ρ_{FPws}).

Indeed, I find strong negative correlations in inter-annual precipitation, generally limited to the southern Hemisphere (Fig 3.6e). Critically, the autocorrelation of annual wet season precipitation rainfall is dependent on the link between fire and rainfall, and is strongest in regions where the fire is linked with subsequent rainfall reductions (Fig. 3.7).

This does not single out fire as the only cause of this statistical feature, as there is still a weak, negative autocorrelation in regions where the fire-rainfall relationship is neutral or positive. I note that my analysis does not consider exogenous drivers such as climate or ocean temperatures or how these might contribute to alternating low and high rainfall years (e.g., the quasi-biennial oscillation [*Hastenrath*, 1995; *Jury et al.*, 2004]). However, my proposed feedback could help explain the differing modes of climate variability between the Kalahari and the Sahel, despite similar large-scale climatic controls [e.g. *Nicholson*, 2000; *Cook et al.*, 2006].

Acknowledgements

This research was supported by NASA under grant award number NNX 11AQ23G. M.V.S. received partial support from the National Science Foundation Graduate Research Fellowship Program and the Virginia Space Grant Consortium Graduate STEM Research Fellowship Program. The authors declare no conflicts of interest, financial or otherwise. The datasets used in this study are freely available from their respective websites: MODIS: https://lpdaac.usgs.gov/data_access/data_pool, TRMM: http://pmm.nasa.gov/data-access/downloads/trmm.

References

Andela, N., Liu, Y. Y., Van Dijk, A. I. J. M., De Jeu, R. A. M., & McVicar, T. R. (2013). Global changes in dryland vegetation dynamics (1988-2008) assessed by satellite remote sensing: comparing a new passive microwave vegetation density record with reflective greenness data. *Biogeosciences*, *10*(10), 6657.

Archibald, S., Roy, D. P., Wilgen, B., W., & Scholes, R. J. (2009). What limits fire? An examination of drivers of burnt area in Southern Africa. *Global Change Biology*, *15*(3), 613-630.

Barbosa, P. M., Stroppiana, D., Grégoire, J. M., & Cardoso Pereira, J. M. (1999). An assessment of vegetation fire in Africa (1981–1991): Burned areas, burned biomass, and atmospheric emissions. *Global Biogeochemical Cycles*, *13*(4), 933-950.

Beringer, J., *et al*. (2015). Fire in Australian savannas: from leaf to landscape. *Global Change Biology*, *21*(1), 62-81.

Charney, J., Stone, P. H., & Quirk, W. J. (1975). Drought in the Sahara: a biogeophysical feedback mechanism. *Science, 187*(4175), 434-435.

Cook, B. I., Bonan, G. B., & Levis, S. (2006). Soil moisture feedbacks to precipitation in southern Africa. *Journal of Climate*, *19*(17), 4198-4206.

De Sales, F., Xue, Y., & Okin, G. S. (2016). Impact of burned areas on the northern African seasonal climate from the perspective of regional modeling. *Climate Dynamics*, *47*(11), 3393-3413.

D'Odorico, P., & Porporato, A. (2004). Preferential states in soil moisture and climate dynamics. *Proceedings of the National Academy of Sciences of the United States of America*, *101*(24), 8848-8851.

Fensholt, R., *et al*. (2012). Greenness in semi-arid areas across the globe 1981–2007—An Earth Observing Satellite based analysis of trends and drivers. *Remote sensing of environment*, *121*, 144-158.

Findell, K. L., Gentine, P., Lintner, B. R., & Kerr, C. (2011). Probability of afternoon precipitation in eastern United States and Mexico enhanced by high evaporation. *Nature Geoscience, 4*(7), 434.

Flannigan, M. D., Krawchuk, M. A., de Groot, W. J., Wotton, B. M., & Gowman, L. M. (2009). Implications of changing climate for global wildland fire. *International Journal of Wildland Fire, 18*(5), 483-507.

Friedman, J., Hastie, T., & Tibshirani, R. (2001). *The Elements of Statistical Learning* (Vol. 1, pp. 337-387). New York: Springer series in statistics.

Gatebe, C. K., Ichoku, C. M., Poudyal, R., Román, M. O., & Wilcox, E. (2014). Surface albedo darkening from wildfires in northern sub-Saharan Africa. *Environmental Research Letters*, *9*(6), 065003.

Görgen, K., Lynch, A. H., Marshall, A. G., & Beringer, J. (2006). Impact of abrupt land cover changes by savanna fire on northern Australian climate. *Journal of Geophysical Research: Atmospheres, 111*(D19).

Govender, N., Trollope, W. S., & Van Wilgen, B. W. (2006). The effect of fire season, fire frequency, rainfall and management on fire intensity in savanna vegetation in South Africa. *Journal of Applied Ecology*, *43*(4), 748-758.

Guillod, B. P., Orlowsky, B., Miralles, D. G., Teuling, A. J., & Seneviratne, S. I. (2015). Reconciling spatial and temporal soil moisture effects on afternoon rainfall. *Nature Communications*, *6*, 6443.

Hastenrath, S. (1995), Climate Dynamics of the Tropics, Kluwer Academic Publishers, Netherlands.

Hernandez, C., Drobinski, P., & Turquety, S. (2015). Impact of wildfire-induced land cover modification on local meteorology: A sensitivity study of the 2003 wildfires in Portugal. *Atmospheric Research*, *164*, 49-64.

Huffman, G. J., Bolvin, D. T., Nelkin, E. J., Wolff, D. B., Adler, R. F., Gu, G., ... & Stocker, E. F. (2007). The TRMM multisatellite precipitation analysis (TMPA): Quasi-global, multiyear, combined-sensor precipitation estimates at fine scales. *Journal of Hydrometeorology*, *8*(1), 38-55.

Jury, M. R., White, W. B., & Reason, C. J. (2004). Modelling the dominant climate signals around southern Africa. *Climate Dynamics*, *23*(7-8), 717-726.

Katul, G. G., Oren, R., Manzoni, S., Higgins, C., & Parlange, M. B. (2012). Evapotranspiration: a process driving mass transport and energy exchange in the soil-plant-atmosphere-climate system. *Reviews of Geophysics*, *50*(3).

Lawrence, D., & Vandecar, K. (2015). Effects of tropical deforestation on climate and agriculture. *Nature Climate Change*, *5*(1), 27.

Lehmann, C. E., *et al*. (2014). Savanna vegetation-fire-climate relationships differ among continents. *Science*, *343*(6170), 548-552.

Lynch, A. H., Abramson, D., Görgen, K., Beringer, J., & Uotila, P. (2007). Influence of savanna fire on Australian monsoon season precipitation and circulation as simulated using a distributed computing environment. *Geophysical Research Letters*, *34*(20).

Meng, X. H., Evans, J. P., & McCabe, M. F. (2014). The influence of inter-annually varying albedo on regional climate and drought. *Climate Dynamics*, *42*(3-4), 787-803.

Montes-Helu, M. C., Kolb, T., Dore, S., Sullivan, B., Hart, S. C., Koch, G., & Hungate, B. A. (2009). Persistent effects of fire-induced vegetation change on energy partitioning and evapotranspiration in ponderosa pine forests. *Agricultural and Forest Meteorology*, *149*(3-4), 491-500.

Nicholson, S. E. (2000). The nature of rainfall variability over Africa on time scales of decades to millenia. *Global and Planetary Change*, *26*(1-3), 137-158.

Notaro, M., Wyrwoll, K. H., & Chen, G. (2011). Did aboriginal vegetation burning impact on the Australian summer monsoon?. *Geophysical Research Letters*, *38*(11).

Rosenfeld, D., *et. al*. (2008). Flood or drought: how do aerosols affect precipitation?. *Science*, *321*(5894), 1309-1313.

Roy, D. P., Boschetti, L., Justice, C. O., & Ju, J. (2008). The collection 5 MODIS burned area product—Global evaluation by comparison with the MODIS active fire product. *Remote Sensing of Environment*, *112*(9), 3690-3707.

Seneviratne, S. I., *et al*. (2010). Investigating soil moisture–climate interactions in a changing climate: A review. *Earth-Science Reviews*, *99*(3-4), 125-161.

Snyman, H. A. (2003). Short-term response of rangeland following an unplanned fire in terms of soil characteristics in a semi-arid climate of South Africa. *Journal of Arid Environments*, *55*(1), 160-180.

Tosca, M. G., Diner, D. J., Garay, M. J., & Kalashnikova, O. V. (2015). Human-caused fires limit convection in tropical Africa: First temporal observations and attribution. *Geophysical Research Letters*, *42*(15), 6492-6501.

Van Der Werf, G. R., Randerson, J. T., Giglio, L., Gobron, N., & Dolman, A. J. (2008). Climate controls on the variability of fires in the tropics and subtropics. *Global Biogeochemical Cycles*, *22*(3).

Veraverbeke, S., Verstraeten, W. W., Lhermitte, S., Van De Kerchove, R., & Goossens, R. (2012). Assessment of post-fire changes in land surface temperature and surface albedo, and their relation with fire–burn severity using multitemporal MODIS imagery. *International Journal of Wildland Fire*, *21*(3), 243-256.

Wendt, C. K., Beringer, J., Tapper, N. J., & Hutley, L. B. (2007). Local boundary-layer development over burnt and unburnt tropical savanna: an observational study. *Boundary-Layer Meteorology*, *124*(2), 291-304.

Wood, S. (2006) *Generalized Additive Models. An Introduction with R.* Chapman & Hall/CRC, New York.

Zhu, L., & Southworth, J. (2013). Disentangling the relationships between net primary production and precipitation in southern Africa savannas using satellite observations from 1982 to 2010. *Remote Sensing*, *5*(8), 3803-3825.

Chapter Four

Albedo Changes After Fire as an Explanation of Fire-Induced Rainfall Suppression

Go write your message on the pavement
Burn so bright I wonder what the wave meant

Red Hot Chili Peppers

Substantial parts of this Chapter are published as

Saha, M. V., D'Odorico, P., & Scanlon, T. M. (2017). Albedo changes after fire as an explanation of fire-induced rainfall suppression. *Geophysical Research Letters*, *44*(8), 3916-3923.

4.1 Abstract

Observational evidence of rainfall suppression by fire has recently been documented in African drylands, but the underlying mechanism remains poorly understood. Here I investigate the extent to which fire-induced changes in latent heat flux and albedo may inhibit boundary layer predisposition to convective rainfall. I use MERRA-2 reanalysis data from the Kalahari region of Southern Africa to drive a low-dimensional boundary layer growth model. I find that both increased albedo and, to a lesser extent, increased latent heat flux, could result in less convective rainfall. The sensitivity to land surface feedbacks is higher earlier in the dry season and at drier sites. Finally, using MODIS fire and albedo data, I present novel evidence that increases in albedo after fire, or brightening, is common in regions receiving less than 850 mm of precipitation annually. This supports the idea that fire-induced surface brightening is responsible for observed rainfall deficits after fire.

4.2 Introduction

Fire is widespread in sub-Saharan Africa and has the ability to alter the land surface at frequent intervals and over large spatial scales [*Barbosa et al*., 1999]. Such disturbances modify the surface energy balance and local atmospheric conditions, which could in turn modify rainfall [*Wendt et al*., 2007]. Because fire scars are spatially fixed, preferential convective activity over burned or unburned areas could result in the accumulation of significant rainfall anomalies at seasonal time-scales [*Beringer et al*., 2003; *Ichoku et al*., 2016; Chapter Three]. Building understanding of seasonal rainfall deficits in regions where water resources are tightly linked to livelihoods has clear societal implications. Given the link between human activities and fire, fire-induced rainfall suppression may represent a novel anthropogenic influence on regional climate. In Chapter Three I presented remotely-sensed observational and statistical evidence of significant rainfall suppression in African drylands after widespread fire. I demonstrated that extensive fire, particularly if late in the dry season, preceded lower than average wet season rainfall, especially in water limited regions. While the statistical relationship reported was robust, that study did not investigate the underlying mechanisms and did not attempt to explain the observed effect of fire-induced rainfall suppression. Indeed, to date a mechanistic understanding of the impact of fire on wet season precipitation is still missing. Developing a mechanistic understanding of these observed deficits is the goal of this current study. Aerosol-mediated rainfall-fire feedbacks are known to occur during the dry season, when fires are burning [*Tosca et al*., 2015; *Hodnebrog et al*., 2016]. Land surface influences on energy balance and atmospheric development could be a possible, longer-enduring mechanism to explain how rainfall deficits accumulate over the entire wet season, when aerosol loading is limited. In this study, I specifically evaluate the hypothesis that land-surface feedbacks, caused by modification to the land surface by fire, could realistically explain observed rainfall suppression. Previous studies have investigated this question using coupled regional models, finding either enhancement or suppression of rainfall depending on the region and the parameterization of fire and convection in the model [*Görgen et al*., 2006; *Lynch et al*., 2007; *Hernandez et al*., 2015; *De Sales et al*., 2016]. For this reason, I use a conceptually simple boundary layer growth model, which allows us to isolate the various mechanisms that could produce suppression while parameterizing the effects of fire on land surface changes in a simple but realistic way.

The impacts of fire on the land surface vary and in some cases are heavily dependent on climate and ecosystem properties. Two well-described changes after fire are albedo modification and latent heat flux reductions [*Gatebe et al*., 2014; *Beringer et al*., 2015]. Albedo is a key surface attribute that influences the amount of solar radiation that is available for turbulent heat fluxes originating at the land surface. Typically, fire results in instantaneous darkening due to char deposition on the land surface, which in turn enhances absorption of solar radiation and increases the amount of energy available to sensible and latent heat fluxes. Over longer time periods, however, this char may be removed by wind and precipitation, revealing a de-vegetated land surface with exposed dry and optically bright soils, thereby increasing in albedo. There is evidence of increased albedo relative to unburned areas (hereafter "brightening") in semi-arid systems at temporal lags of years [*Veraverbeke et al*., 2012], but the extent to which this occurs over intermediate timescales has not been fully explored, particularly in the study region of southern Africa. For this reason, I model both increases and decreases in albedo after fire, and attempt to quantify the effect of fire on albedo over timescales relevant to the land-atmosphere interactions being investigated.

While albedo modulates the total amount of available energy, damage to vegetation affects the way available energy is partitioned. Damage to plants occurs directly by removing plant biomass and indirectly through heat damage from fire, resulting in reduced photosynthetic activity and transpiration [*Beringer et al*., 2003]. The result is an overall reduction in latent heat fluxes and land surface contributions to atmospheric moisture while increasing sensible and ground heat fluxes. The severity and persistence of these changes is dependent on the intensity of the fire, but can result in a 400% reduction in latent heat fluxes, with accompanying increases in sensible heat flux [*Beringer et al*., 2003; *Beringer et al*., 2015].

Geographic setting, climate and seasonality influence the sensitivity of the land surface to land-atmosphere coupling and atmospheric feedbacks [*Koster et al*., 2004; *Guillod et al*., 2015]. Studies have identified transition zones, both spatial and temporal, as regions where coupling is typically strong [*Seneviratne et al*., 2010; *Nicholson*, 2015]. Spatial transition zones include semi-arid landscapes along a rainfall gradient, and temporal transition periods include shifts from the dry to wet season [*Koster et al*., 2004; *Notaro et al*., 2011]. To investigate the influence of these factors, I consider different locations along a rainfall gradient and different times of the wet season in my analysis.

The specific goals of this study are to (1) investigate how land surface changes after fire could modify convective rainfall using a simple boundary layer model, (2) understand how these results vary over a climatic gradient and during different times of the wet season, and (3) use satellite data to assess the actual land surface modifications after fire in southern Africa and to see if this agrees with the model-derived mechanism for suppression of rainfall by fire. Achieving these goals will give a mechanistic explanation of observed rainfall suppression and build understanding of the role that fire plays in fire-rainfall feedbacks.

4.3 Methods and Satellite Data

4.3.1 Study Region

The focus of this study is the Kalahari region of southern Africa. Also known as the "Kalahari Transect", this region features a strong north-south rainfall gradient that that is dominated by a November-April wet season during which ~90% of precipitation occurs [*Koch et al*., 1995; *Nicholson,* 2011]. Some of the strongest rainfall suppression presented in Chapter Three was observed here, and therefore focusing on this region may help to diagnose a land-surface control on rainfall suppression. In the discussion that follows, November represents a transitional period, when the southward expansion of the inter-tropical convergence zone results in a shift from dry conditions to higher moisture availability and increased plant productivity.

The month of February represents the peak of the wet season. I run the model using reanalysis data from these two months (see Section *4.3.2 Reanalysis Data*) on pixels located at 23°, 20°, 17° and 14° S along a north-south transect fixed at 21.88° W longitude. These sites have a mean annual precipitation (MAP) of approximately 300, 400, 600, and 800 mm, respectively.

4.3.2 Reanalysis Data

I use reanalysis data from MERRA-2 [*Molod et al.*, 2015] to impose initial conditions (morning boundary layer height, potential temperature and specific humidity) and prescribe sensible and latent surface fluxes in the boundary layer growth model. MERRA-2 provides surface fluxes and atmospheric states using the GEOS-5 land surface model [*Molod et al.*, 2015 and references therein]. To complete these analyses, I compiled hourly data from the months of February and November over the period 1980-2015, with all times reported in local standard time (LST). The use of reanalysis data in this model is not meant to represent an accurate historical record of actual boundary layer dynamics, but rather to capture daily and synoptic variability in the drivers of boundary layer growth across many seasons.

4.3.3 Boundary Layer Growth Model

Following Andersen *et al*. [2007], Van Heerwaarder *et al*. [2009] and others, I adopt the boundary layer growth model of McNaughton and Spriggs [1986] to simulate the response of the land surface to fire-induced changes in sensible and latent heat fluxes (the time-varying variables H and λE, respectively). This model tracks the evolution of height, potential temperature and specific humidity of a well-mixed layer over the course of a day. A detailed description of the model is provided in Appendix Two (section *A2.1.1: Model Details*) and other references

[*Lhomme & Elguero*, 1999]. To assess the effect of fire on boundary layer dynamics, I artificially modify the reanalysis input to reflect changes that typically occur after fire, namely albedo and latent heat flux modification. I parameterize fire as a proportional change in surface albedo and latent heat flux (the variables f_{α} and $f_{\lambda E}$, respectively). These changes are then used to adjust the reanalysis time-series of H and λE as inputs into the boundary layer model. The approach used to modify H and λE for different values of f_{α} and $f_{\lambda E}$ is described in Appendix Two (*section 3.1.2 Representing Fire in the Model*).

4.3.4. Assessing Boundary Layer Differences

I quantify the potential modification of convective rainfall using lifting condensation level (LCL) crossings, an approach that reflects the dominance of convection as a rainfall generating mechanism in southern Africa [Nicholson, 2011]. The equations used to calculate LCL height are described in the Supporting Information (Appendix Two, *section A2.1.3 LCL Calculation*, based on Bolton [1980]). An LCL crossing occurs at any model time-step when the boundary layer height, h exceeds the lifting condensation level, h_{LCL}. While this does not measure the occurrence or depth of actual convective storms, it provides a simple indicator of whether the atmosphere is predisposed to convective rainfall at a given time and is considered a necessary condition for the occurrence of convective rainfall [*Juang et al*., 2007]. Using this method with simple boundary layer growth models has proven a useful tool for gaining insight into how competing mechanisms of boundary layer growth and entrainment can modify convective rainfall [*Daly et al*., 2004; *Mande et. al*., 2015; *Manoli et al*., 2016]. For example, using similar simple boundary layer growth model, Mande *et al.* [2015] found that all instances of measured convective rainfall at their semi-arid study site were preceded by an LCL crossing.

There is a strong empirical relationship between daily crossing statistics and bias-corrected rainfall rate and cumulative rainfall across all sites and both months (Appendix Two, *section A2.1.3*, Fig. 4.1-2; Reichle *et al*. [2016]), confirming the relevance of LCL crossings as a proxy of convective precipitation. This method will allow us to isolate the effect of surface modification by attributing changes in LCL crossings with changes in *h*, changes in h_{LCL}, or both.

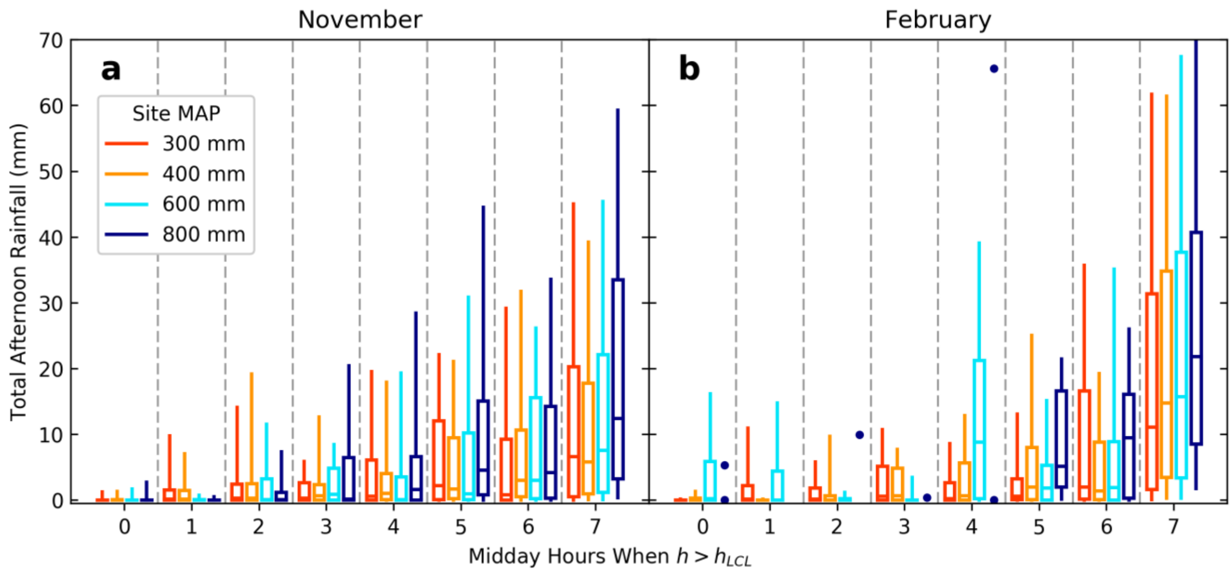

Figure 4.1. Variability in daily afternoon (1200-2000 LST) rainfall amount for different durations of midday (1000-1600 LST) crossings for (a) November and (b) February. The boxes depict the 25th, 50th and 75th percentiles of each distribution. Whiskers represent the 10th and 90th percentiles of each distribution. Bins with less than 5 elements are depicted with dots for each individual measurement.

4.3.5. Fire and Albedo Satellite Data

To quantify the actual albedo changes caused by fires I used MODIS MCD45A1 collection 5.1 burned area product at 500 m resolution over the Kalahari Transect between the southernmost and northernmost sites included in this study (latitude range 23° to 8° S; longitude range 22° to 25° W) [*Roy et al*., 2008]. I used 15 years of dry season (April-October) data, from

2000 through 2015 (omitting 2001 because of missing data) to catalog the occurrence of dry season fire. I quantified albedo anomalies using the MODIS white sky albedo product (MCD43A3, collection 5.0) at the same resolution and over the same years. I obtained an average November albedo for each pixel and year of record by averaging available November measurements (3-4 scenes each year), ignoring missing values. Albedo anomalies due to fire were computed at each burned pixel as the difference between these yearly November albedo values and the average albedo of that same pixel during years when no fire occurred (a temporal anomaly). An additional spatial anomaly is also computed using the same data (details in Appendix Two, *section A2.2.4*). For comparison with f_α, I present these temporal anomalies as a fractional deviation from the average albedo over all years.

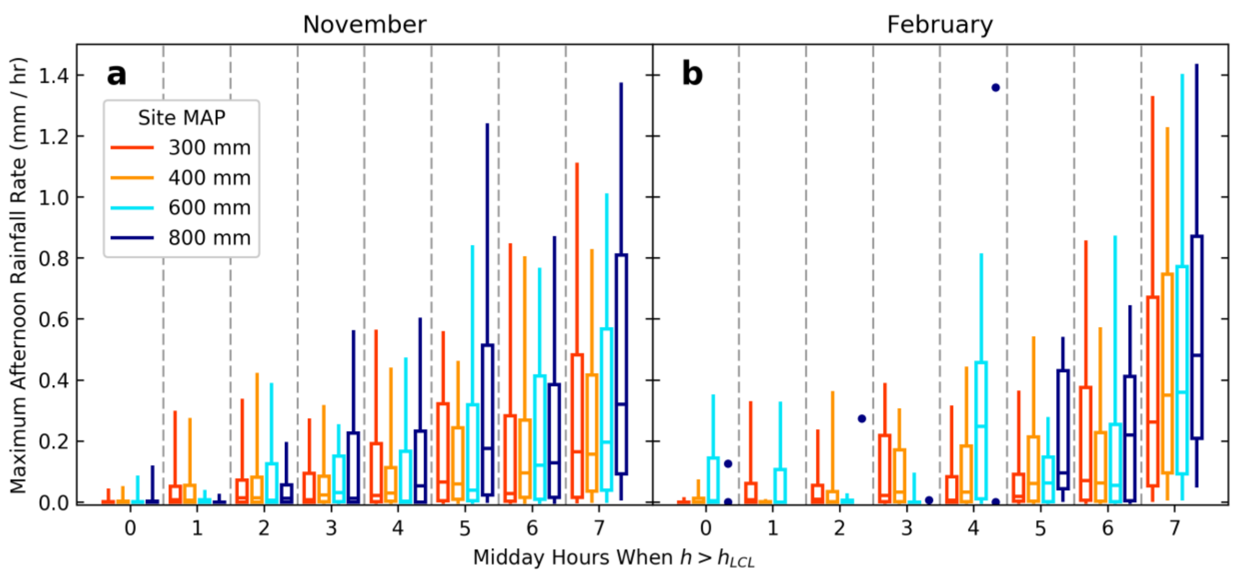

Figure 4.2. Variability in daily afternoon (1200-2000 LST) maximum rainfall rate for different durations of midday (1000-1600 LST) crossings for November (left panel) and February (right panel). The boxes depict the 25th, 50th and 75th percentiles of each distribution. Whiskers represent the 10th and 90th percentiles of each distribution. Bins with less than 5 elements are depicted with dots for each individual measurement.

4.4 Results

4.4.1 Comparison between model and reanalysis crossing statistics

For the month of November, hourly LCL crossings calculated from reanalysis data peak in the afternoon across all of the sites (Fig. 4.3a, solid lines). The frequency of crossings is dependent on the aridity of the site, with peak hourly crossings increasing from 54.1% of days at 300 mm MAP to 94.3% of days at 800 mm MAP. In February, all sites show a higher proportion of days with crossings (Fig 4.3b) with a similar diurnal pattern.

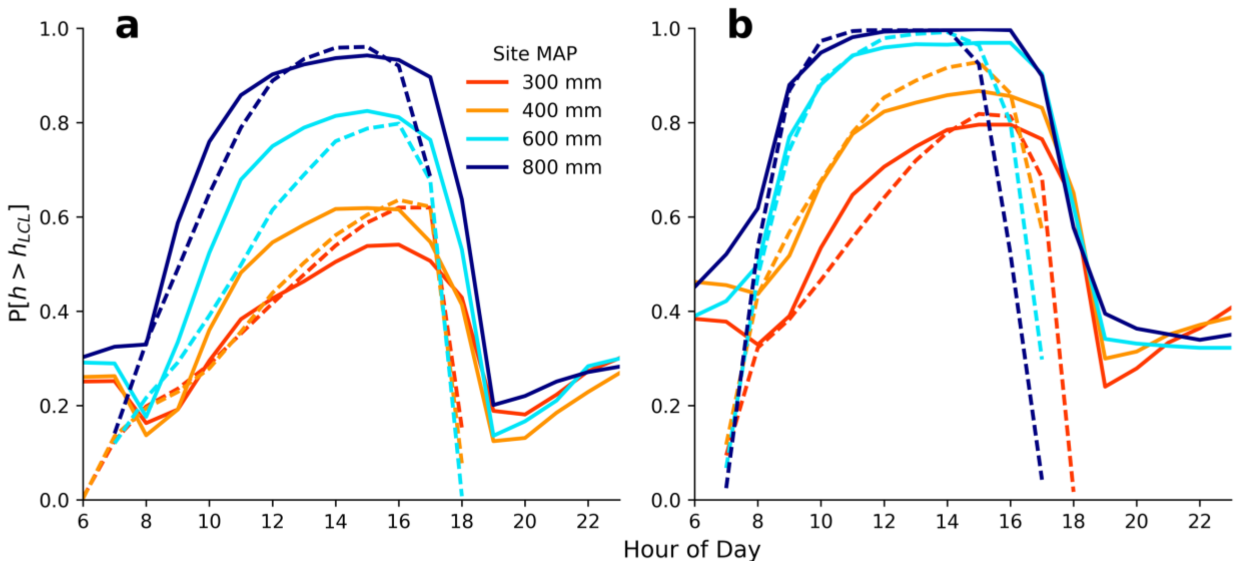

Figure 4.3. The proportion of days in (a) November or (b) February for which *h* exceeds h_{LCL} during a given hour. Reanalysis data and control simulations are shown with a solid and dotted line, respectively. Colors represent different sites along the Kalahari Transect.

I compare these reanalysis values with the base case of the simulation in which both f_α and $f_{\lambda E}$ are set to 1, such that net radiation and heat fluxes are not modified from reanalysis values. This control case can be compared to crossing statistics derived from the reanalysis dataset and can be used to gauge the performance of my model. The control simulation largely mirrors the diurnal dynamics observed in the reanalysis data, both in timing and overall magnitude (Fig. 4.3a, dotted lines). The model captures the temporal dynamics of boundary layer crossings well in all of the sites. The timing of the control simulation peak crossing is within an hour of the corresponding reanalysis value for all sites and the average difference between crossing peaks across sites is 2.18%. The performance of the control simulation is similar for the month of February (Fig. 4.3b).

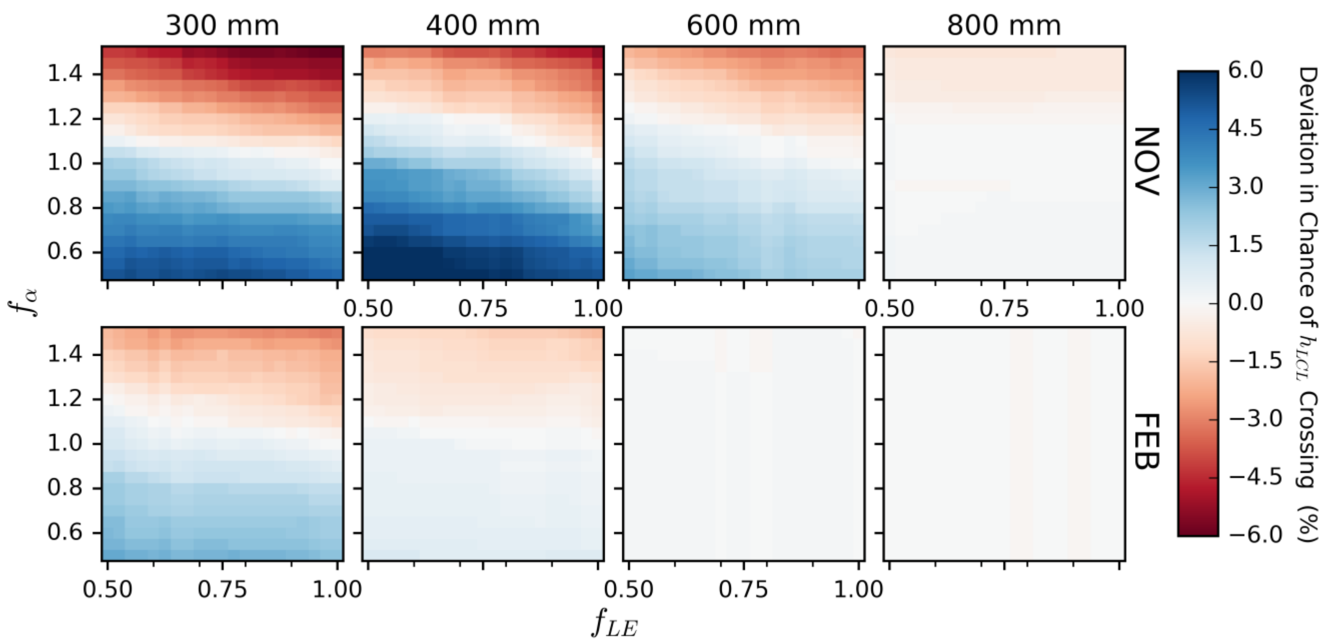

Figure 4.4. Changes in the frequency of LCL crossing associated with proportional changes in albedo and latent heat fluxes. Each column represents a site at a different position and MAP along the Kalahari Transect (from left to right: 300 mm, 400 mm, 600 mm, 800 mm) and each row represents different timings during the season (top: November, bottom: February).

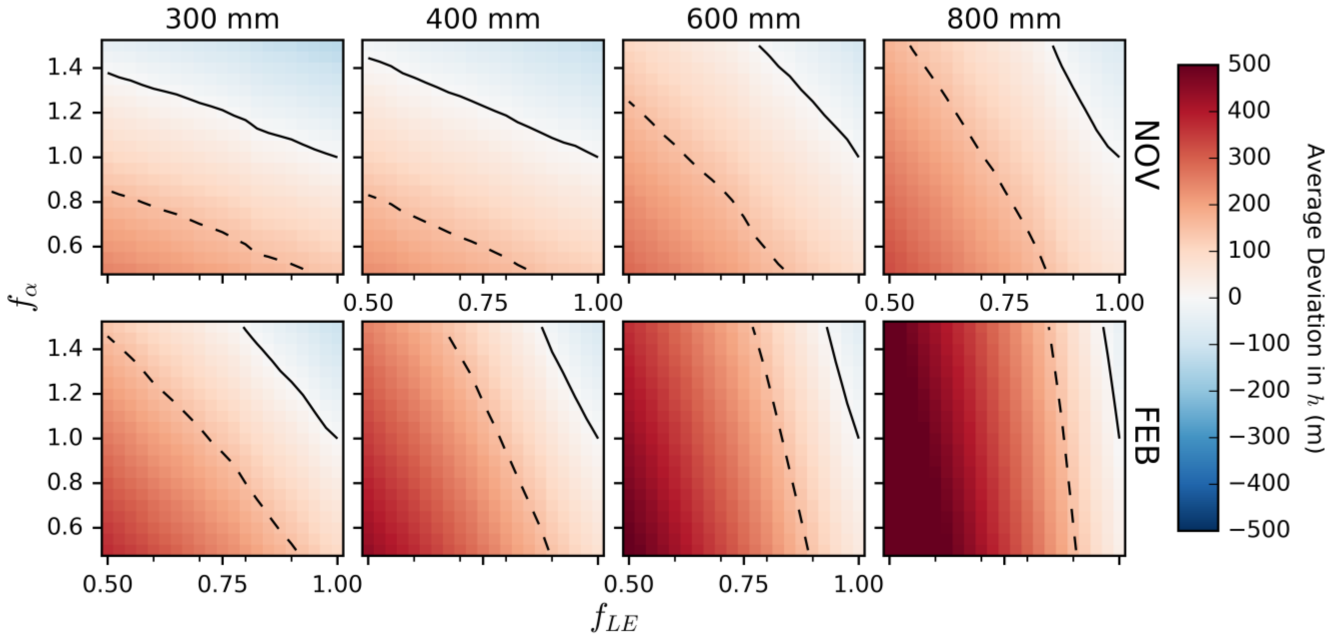

Figure 4.5. Variation in simulated average 1500 LST boundary layer height (*h*) as a function of proportional changes in albedo and latent heat flux. The solid and dashed lines represent contours at 0 m and +/-150 m, respectively. Panels arranged as in Fig 4.1.

4.4.2 Effect of experimental variables on h, h_{LCL} crossings.

I now compare simulated crossings under experimental values of f_α and f_{LE} to the control scenario with f_α and f_{LE} equal to 1. Excluding the 800 mm site in which almost no variability is seen as a result of f_α or f_{LE} modification, I observe increases in the rate of crossings in simulations where f_{LE} and f_α are both high (Fig. 4.4). Suppression of crossings, on the other hand, is only observed where brightening occurs ($f_\alpha > 1$). For the range of experimental values of f_{LE} (0.5 to 1.0) and f_α (0.5 to 1.5) considered here, the deviation in the chance of crossings (calculated as the percent of days with crossings in the experimental case minus the percent of days with crossings in the control case) is about +/-6%.

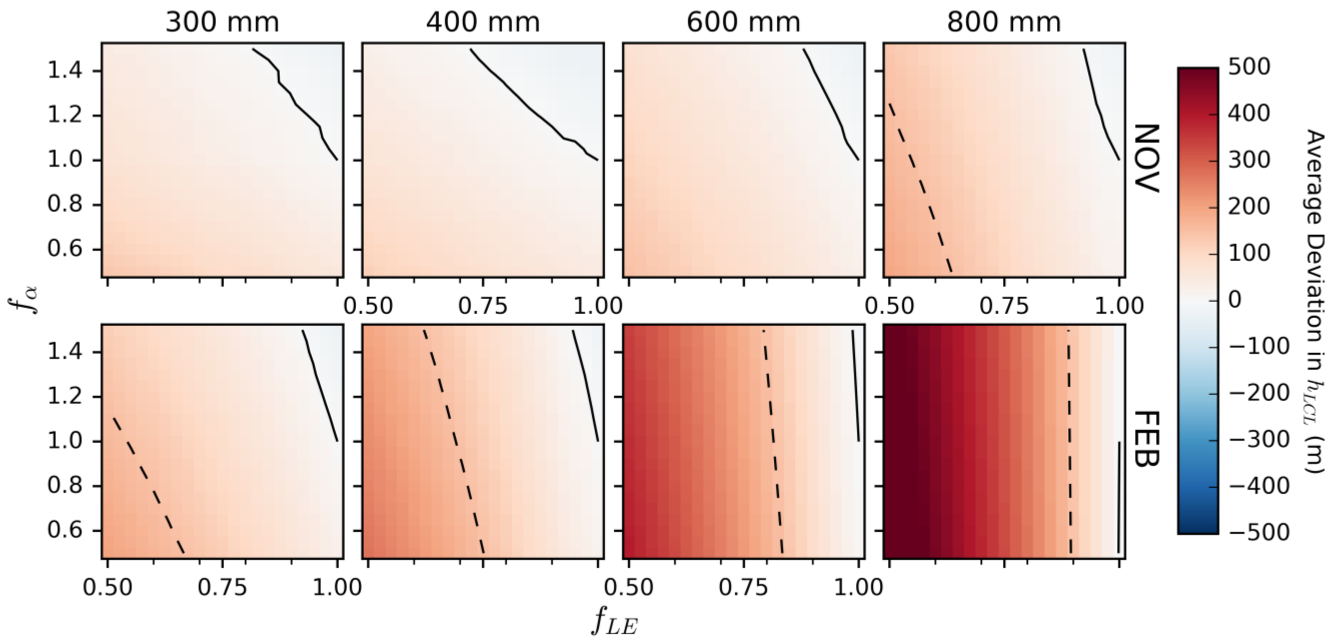

Figure 4.6. Variation in simulated average 1500 LST h_{LCL} as a function of proportional changes in albedo and latent heat flux. The solid and dashed lines represent contours at 0 m and +/-150 m, respectively. Panels arranged as in Fig 4.1.

The diurnal variability in boundary layer growth and LCL growth represents a tradeoff in the growth of the boundary layer and the height of the LCL. On one hand, lower f_α and f_{LE} increase sensible heat fluxes and boundary layer growth, which could increase the chance of a crossing due to higher *h*. On the other hand, higher sensible heat flux increases mixed layer potential temperature, which could decrease the chance of a crossing due to a higher h_{LCL}. My findings of rainfall enhancement at lower f_α and f_{LE} indicate that in the semi-arid Kalahari region, crossings are more heavily influenced by the first pathway (modified *h* growth) than by simultaneous modifications to h_{LCL}. This can be seen by comparing Figures 4.5 and 4.6, which show that the magnitude of the *h* deviations (Fig. 4.5) are larger than changes in h_{LCL} for the same point in parameter space (Fig. 4.6, compare respective panels). Similarly, where I see suppression at high values of f_α and f_{LE}, the decrease in boundary layer height due to reduced sensible heat flux is of a larger magnitude than the decrease in LCL due to a moister boundary layer, in effect lowering the chance of a crossing.

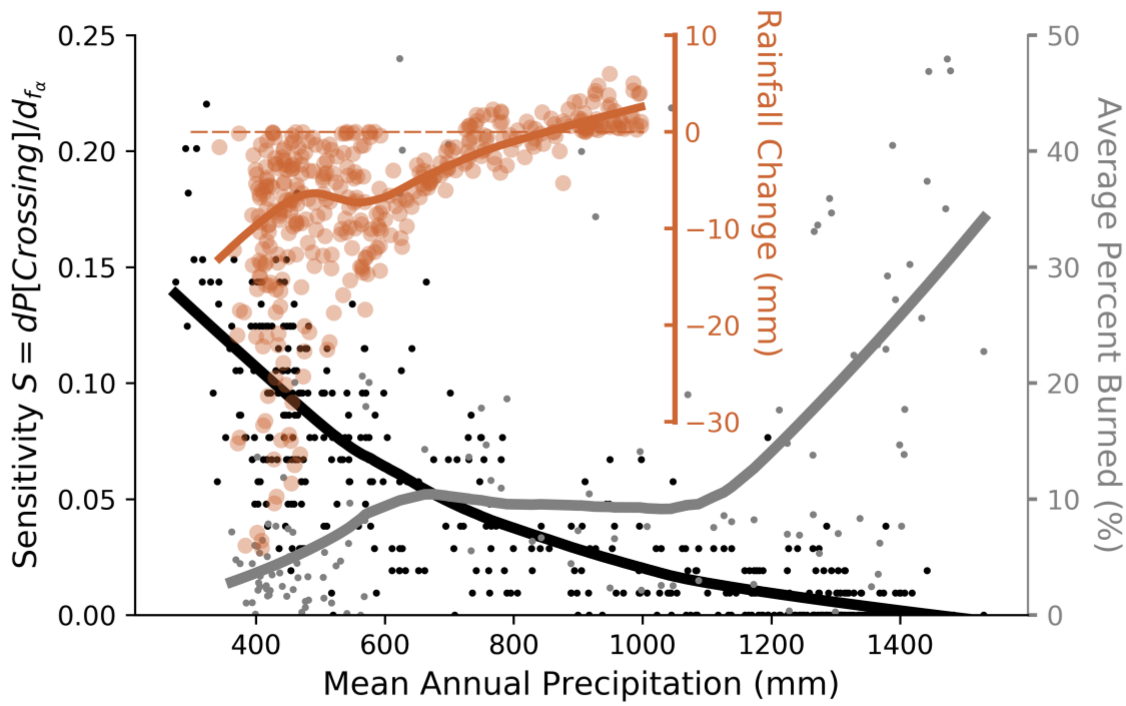

Figure 4.7. Fire, sensitivity to land surface feedbacks and rainfall suppression along the Kalahari Transect. Black points (left vertical axis) represent sensitivity of LCL crossings to albedo changes as a function of MAP. Grey points (right vertical axis) show the average percentage of the landscape burned annually. Orange sub-plot depicts the average change in wet season annual precipitation due to fire over the Kalahari Transect. Trends are highlighted in thick lines using a lowess smoother with bandwidth 0.5. Fire and rainfall suppression data are reproduced from Chapter Two over the Kalahari transect.

4.4.3 Seasonal and spatial variability in the occurrence of h, h_{LCL} *crossings*

I can interpret the deviation of the crossing rates per a given change in f_α or f_{LE} as the sensitivity of that site to land-atmosphere feedbacks. The largest deviations from the baseline crossing rate occurred at the driest site, indicating that more arid regions have a higher sensitivity to a given increment in f_α (Fig 4.4.; comparing across columns). Likewise, the sensitivity decreases from the transitional month of November to February (Fig. 4.4; comparing across rows). As the change in crossing rate is greater over the range of f_α at constant f_{LE} than for f_{LE} at constant f_α, I formally define the sensitivity in terms of f_α as $S=\Delta P[h > h_{LCL}] / \Delta f_\alpha$, evaluated at $f_\alpha = f_{LE} = 1$, where $P[h > h_{LCL}]$ is the proportion of days with a simulated LCL crossing. I calculate sensitivity to understand how it changes across a finer gradient of MAP in Figure 4.7. Clearly, the sensitivity of LCL crossings to fractional changes in albedo increase with increased aridity.

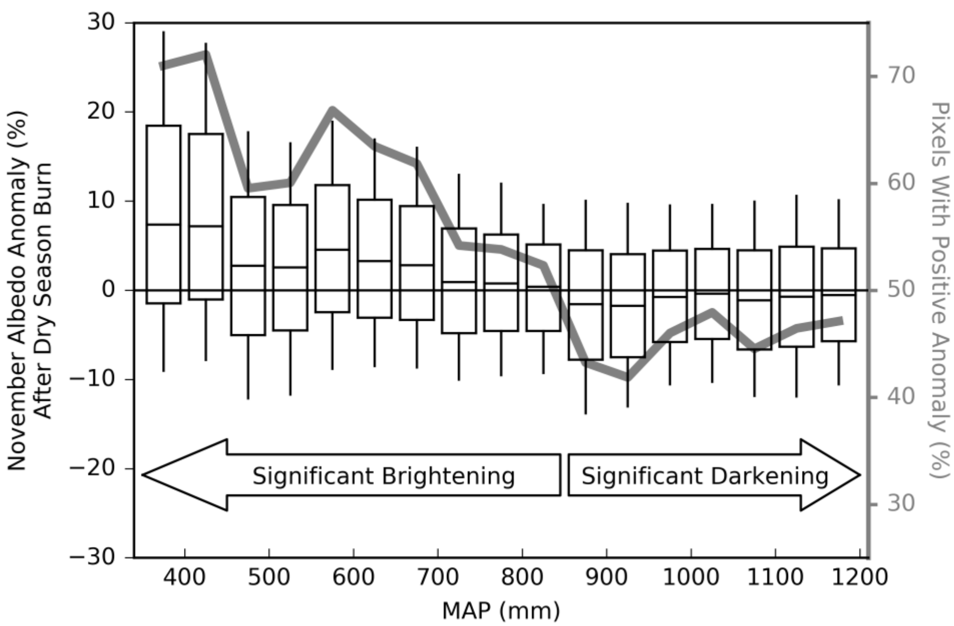

Figure 4.8. Changes in albedo after fires in southern Africa. Individual albedo anomalies for a given year and pixel are pooled into 50 mm wide MAP bins starting at 375 mm. The boxes depict the 25th, 50th and 75th percentiles. Whiskers represent the 10th and 90th percentiles of the bin samples. The thick gray line shows the percentage of pixels in each bin that have a positive albedo anomaly. Due to the large sample sizes all bins are significantly different than zero (α=0.001) as determined by the Wilcoxon signed-rank test with the sequential Bonferroni adjustment for multiple comparisons.

4.4.4 Satellite Evidence of Brightening

There is strong observational evidence of increased albedo after fires (brightening) below 800 mm MAP that is manifested during the transition month of November (Fig. 4.8). The median albedo anomaly in the 350 – 400 mm range is a +7.36% above average, a significant positive bias. A high proportion of pixels undergo some brightening; at 425 mm MAP 72% of pixels show positive anomalies after fire. To a lesser extent, there is evidence of darkening between about 800 and 1200 mm MAP, with a minimum median anomaly of -1.74%.

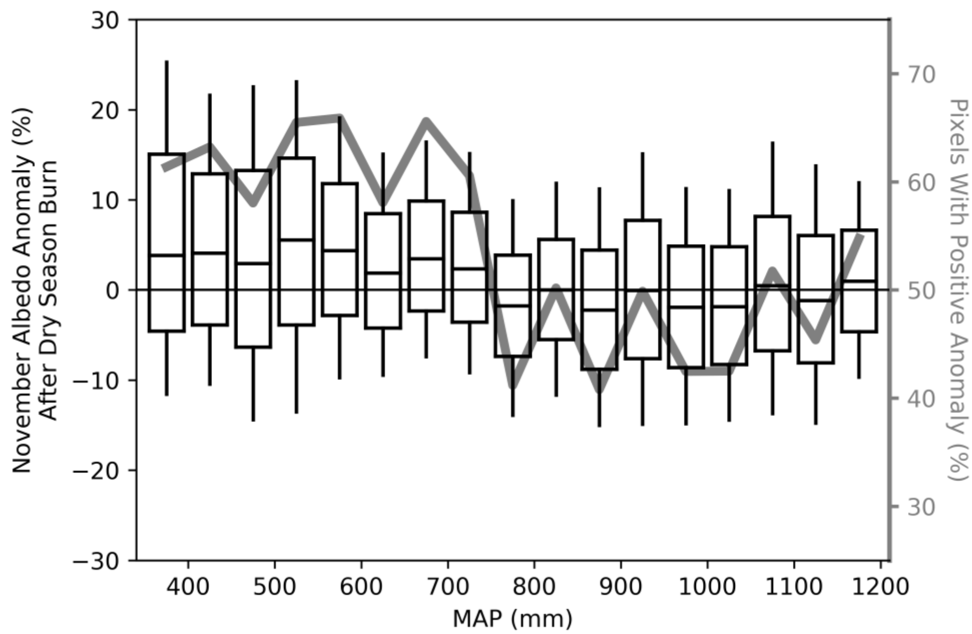

Figure 4.9. Distribution of spatial albedo anomalies as a function of MAP. Spatial albedo anomalies for each year are pooled into 50 mm wide MAP bins starting at 375 mm. The boxes depict the 25th, 50th and 75th percentiles. Whiskers represent the 10th and 90th percentiles of the bin samples. The thick gray line shows the percentage of pixels in each bin that have a positive albedo anomaly. Due to the large sample sizes all bins are significantly different than zero (α=0.05) as determined by the Wilcoxon signed-rank test with the sequential Bonferroni adjustment for multiple comparisons.

4.5 Discussion

4.5.1 Suitability and usefulness of the boundary layer growth model

I demonstrate a strong relationship between afternoon rainfall rates and the number of midday hours for which $h > h_{LCL}$, as determined by reanalysis data (Fig. 4.1-2). This relationship suggests that LCL crossings are an appropriate proxy for investigating changes in convective rainfall. Increased variability at higher crossing durations is expected, as an LCL crossing is a necessary, but not sufficient condition for convective rainfall, and some days with sustained LCL exceedance will not experience rainfall due to factors not investigated here (such as convective inhibition). Nevertheless, the highest median rainfall rate is observed under the highest frequency of crossings in all months and over all sites.

There is an overall agreement between reanalysis and control simulation crossing statistics (Fig 4.3). This is encouraging given the simplistic nature of the model and the lack of site-specific tuning of parameters. The results are similarly encouraging for February data (Fig. 4.3b). I found that the sensitivity of h, h_{LCL} crossings to changes in albedo and LE are the strongest during the onset of the wet season. These findings are in line with the idea that coupling between the surface conditions and precipitation is strongest at times when water limitation and convective activity coincide [*Seneviratne et al*., 2010; *Notaro et al*., 2011; *Nicholson*, 2015]. Moreover, I found that sensitivity to land surface conditions was strongest in drier regions, for similar reasons.

4.5.2 Causes of Rainfall Suppression

The chance of an h/h_{LCL} crossing depends on non-linear interactions between boundary layer height, temperature, and moisture content and their influence on h and h_{LCL}. My results detail two possible mechanisms that could contribute to observed rainfall suppression after fire. The first mechanism of rainfall suppression is increased latent heat fluxes. There are some reports of rapid regrowth of herbaceous plants (a "green flush") following fires in Africa drylands [*Archibald et al*., 2005]. Transpiration, a component of latent heat fluxes, increases as a function of green leaf area and could theoretically offset transpiration reductions stemming from damage to woody plants. However, studies that directly measure turbulent fluxes after fire tend to report decreases in latent heat flux [*Beringer et al*., 2003; *Beringer et al*., 2015], which would imply an increase in crossing frequency, are not consistent with the observed patterns of post-fire rainfall suppression [Chapter Two].

A second possible mechanism of convective rainfall suppression is through large-scale brightening of the land surface. The idea of an albedo-rainfall feedback is not new. Notably, Charney [1975] proposed albedo-rainfall feedbacks to explain severe, decadal drought in the Sahel. Albedo-rainfall interactions have been shown to operate on seasonal timescales as well [*Meng et al*., 2014; *Vamborg et al*., 2014]. Negative deviations in crossing frequency (red colors in Fig. 4.4) are observed over the whole ranges of f_{LE}, but only if f_α is positive. While higher f_{LE} results in a lower rate of crossing, brightening ($f_\alpha > 1$) is a necessary condition for rainfall suppression. I note that this finding could change if a broader range of latent heat flux modification were included (specifically, $f_{LE} > 1$), but as stated before, the evidence of LE increases is lacking. Therefore, I claim that albedo changes are more important than latent heat flux changes in explaining observed suppression.

4.5.3 Evidence of Brightening After Fires

My results indicate that over a range of typical changes in albedo and latent heat flux, albedo tends to have a stronger influence on boundary layer crossings than changes in latent heat flux. Specifically, my model results suggest that it is brightening after fires, not darkening as is commonly reported, that could be responsible for rainfall suppression. While studies of fire in African dryland commonly report instantaneous darkening, the possibility of brightening over longer timescales has not been previously studied in this region. I present evidence that, by the time of wet-season onset, the lagged, net effect of dry season fire is a brighter land surface (Fig. 4.8). The evidence of brightening is robust, and is confirmed by calculating spatial albedo anomalies rather than temporal albedo anomalies (Fig. 4.9, compare pattern to Fig. 4.8). This suggests that the observed brightening is not an artifact of spurious correlations of both fire and albedo with interrannual climatic factors (such as drought, which may raise the albedo) that may confound a temporal-only comparison. Because brightening is almost certain to reduce sensible heat fluxes, taken together with evidence that reduced sensible heat flux reduces boundary layer crossings and convective rainfall, evidence of brightening provides a likely mechanism for the observed rainfall suppression. The cause of brightening is not yet known, but other studies have suggested some mechanisms. The revelation of optically bright soils by removing live and senescent vegetation could be one factor. Also, preferential drying of burnt soils may further increase albedo [*Snyman*, 2003], as drier soils are brighter than moist soil [*Lobell & Asner*, 2002]. Further research is needed to better define the role of each of these mechanisms in producing large scale brightening.

There is minimal reporting of fire-induced brightening in Africa and semi-arid landscapes in general, with most studies focused on the instantaneous darkening that follows fire (e.g. Govaerts *et al*., [2002]; Myhre *et al*., [2005]). In a study on long-term albedo dynamics of

Sahelian fires, Gatebe et al. [2014] reported that some fire-affected regions in croplands exhibited brightening, but the majority of burnt pixels exhibit long-term darkening. Chapter Two reported substantial hemispheric differences in the timing of fires, with fires in the Kalahari region tending to occur much later in the dry season than in the Sahel. Late fires tend to be more intense, which could influence the level to which the surface is denuded after fire and potentially alter how much brightening or darkening occurs. Other factors, such as the optical properties of the underlying soil may also determine where brightening occurs after fire relative to a background vegetated state. For example, my study site is underlain by the homogeneous Kalahari sands, it is not clear if these findings are universally applicable over all soil types. Methodological differences prevent a direct comparison with previous studies; future research must resolve this discrepancy to understand where fire has the potential to locally suppress rainfall.

4.5.4 Implications for Fire-Rainfall Interactions

The findings in this study shed light on the observations of fire-induced rainfall deficits in multiple ways. In Chapter Three I presented evidence that fire results in lower than-expected wet season precipitation. In that study I offered a mechanism to further explain these observations, namely, the presence of widespread brightening in the rainfall band where this suppression occurs. Chapter Three also showed that the relationship between fire and wet season rainfall was strongly negative (i.e. rainfall was suppressed) in drier regions (below 850 mm MAP) and weakly positive in more mesic regions (>850 mm MAP, Fig. 4.8, orange line). Not only does my model predict suppression where brightening occurs, but also more frequent crossings when darkening persists after fire. I find that the pattern of brightening as observed in satellite data mirrors this pattern exactly; the strongest rainfall suppression occurs where brightening is the strongest and slight rainfall enhancement occurs above 850, where brightening shifts to darkening. The reduced effect of fire on rainfall above 850 mm MAP relative to the strong suppression that occurs below this threshold is a plausible combination of two observations. First, the magnitude of darkening is significantly lower than the relative magnitude of brightening observed at below 850 mm MAP, which my model suggests would reduce the impact on LCL crossings (Fig. 4.4). Second, my model-derived measure of sensitivity to land surface feedbacks indicates that drier regions are more sensitive to land-surface changes. Together, these results explain subdued enhancement where darkening is observed. My findings suggest that arid regions, which already face severe water limitation and strong interannual variability in water resources, may suffer the greatest adverse effects of rainfall suppression due to fire.

4.5.5 Conclusion

There has been mixed observational and modeling evidence of both rainfall suppression and enhancement due to fire effects at the land surface including vegetation modification. This study builds on previous studies by providing a mechanistic explanation based on post-fire brightening, which could explain observational evidence of rainfall suppression. Furthermore, I present new observational evidence of brightening that occurs at timescales relevant to the rainfall suppression hypothesis. This finding challenges the idea that only darkening occurs after dryland fire. Future modeling efforts should incorporate these findings to fully assess the meteorological impacts of fire. The global extent of brightening and fire-induced rainfall modification has not yet been quantified. If this phenomenon occurs in other regions and continents, it could mean that fire results in seasonal rainfall deficits on a globally relevant scale.

4.6 Acknowledgements

This research was supported by NASA under grant award number NNX 11AQ23G. M.V.S. received support from the NSF Graduate Research Fellowship Program. The authors declare no conflicts of interest. The datasets used are public and freely available from their websites: MODIS: https://lpdaac.usgs.gov/data_access/data_pool, MERRA2: https://disc.gsfc.nasa.gov/daac-bin/FTPSubset2.pl.

4.7 References

Anderson, M. C., Norman, J. M., Mecikalski, J. R., Otkin, J. A., & Kustas, W. P. (2007). A climatological study of evapotranspiration and moisture stress across the continental United States based on thermal remote sensing: 1. Model formulation. *Journal of Geophysical Research: Atmospheres*, *112*(D10).

Archibald, S., Bond, W. J., Stock, W. D., & Fairbanks, D. H. K. (2005). Shaping the landscape: fire–grazer interactions in an African savanna. *Ecological applications*, *15*(1), 96-109.

Barbosa, P. M., Stroppiana, D., Grégoire, J. M., & Cardoso Pereira, J. M. (1999). An assessment of vegetation fire in Africa (1981–1991): Burned areas, burned biomass, and atmospheric emissions. *Global Biogeochemical Cycles*, *13*(4), 933-950.

Beringer, J., Hutley, L. B., Tapper, N. J., Coutts, A., Kerley, A., & O'grady, A. P. (2003). Fire impacts on surface heat, moisture and carbon fluxes from a tropical savanna in northern Australia. *International Journal of Wildland Fire*, *12*(4), 333-340.

Beringer, J., *et. al*. (2015). Fire in Australian savannas: from leaf to landscape. *Global Change Biology*, *21*(1), 62-81.

Bolton, D. (1980). The computation of equivalent potential temperature. *Monthly Weather Review*, *108*(7), 1046-1053.

Charney, J. G. (1975). Dynamics of deserts and drought in the Sahel. *Quarterly Journal of the Royal Meteorological Society*, *101*(428), 193-202.

Daly, E., Porporato, A., & Rodriguez-Iturbe, I. (2004). Coupled dynamics of photosynthesis, transpiration, and soil water balance. Part I: Upscaling from hourly to daily level. *Journal of Hydrometeorology*, *5*(3), 546-558.

De Sales, F., Xue, Y., & Okin, G. S. (2016). Impact of burned areas on the northern African seasonal climate from the perspective of regional modeling. *Climate Dynamics*, *47*(11), 3393-3413.

Gatebe, C. K., Ichoku, C. M., Poudyal, R., Román, M. O., & Wilcox, E. (2014). Surface albedo darkening from wildfires in northern sub-Saharan Africa. *Environmental Research Letters*, *9*(6), 065003.

Görgen, K., Lynch, A. H., Marshall, A. G., & Beringer, J. (2006). Impact of abrupt land cover changes by savanna fire on northern Australian climate. *Journal of Geophysical Research: Atmospheres*, *111*(D19).

Govaerts, Y. M., Pereira, J. M., Pinty, B., & Mota, B. (2002). Impact of fires on surface albedo dynamics over the African continent. *Journal of Geophysical Research: Atmospheres*, *107*(D22).

Guillod, B. P., Orlowsky, B., Miralles, D. G., Teuling, A. J., & Seneviratne, S. I. (2015). Reconciling spatial and temporal soil moisture effects on afternoon rainfall. *Nature Communications*, *6*, 6443.

Hernandez, C., Drobinski, P., & Turquety, S. (2015). Impact of wildfire-induced land cover modification on local meteorology: A sensitivity study of the 2003 wildfires in Portugal. *Atmospheric Research*, *164*, 49-64.

Hodnebrog, Ø., Myhre, G., Forster, P. M., Sillmann, J., & Samset, B. H. (2016). Local biomass burning is a dominant cause of the observed precipitation reduction in southern Africa. *Nature Communications*, *7*, 11236.

Ichoku, C., *et al.* (2016). Biomass burning, land-cover change, and the hydrological cycle in Northern sub-Saharan Africa. *Environmental Research Letters*, *11*(9), 095005.

Juang, J. Y., *et al*. (2007). Eco-hydrological controls on summertime convective rainfall triggers. *Global Change Biology*, *13*(4), 887-896.

Koch, G. W., Vitousek, P. M., Steffen, W. L., & Walker, B. H. (1995). Terrestrial transects for global change research. *Vegetatio*, *121*(1-2), 53-65.

Koster, R. D., *et al*. (2004). Regions of strong coupling between soil moisture and precipitation. *Science*, *305*(5687), 1138-1140.

Lhomme, J. P., & Elguero, E. (1999). Examination of evaporative fraction diurnal behaviour using a soil-vegetation model coupled with a mixed-layer model. *Hydrology and Earth System Sciences Discussions*, *3*(2), 259-270.

Lobell, D. B., & Asner, G. P. (2002). Moisture effects on soil reflectance. *Soil Science Society of America Journal*, *66*(3), 722-727.

Lynch, A. H., Abramson, D., Görgen, K., Beringer, J., & Uotila, P. (2007). Influence of savanna fire on Australian monsoon season precipitation and circulation as simulated using a distributed computing environment. *Geophysical Research Letters*, *34*(20).

Mande, T., Ceperley, N. C., Katul, G. G., Tyler, S. W., Yacouba, H., & Parlange, M. B. (2015). Suppressed convective rainfall by agricultural expansion in southeastern Burkina Faso. *Water Resources Research*, *51*(7), 5521-5530.

Manoli, G., Domec, J. C., Novick, K., Oishi, A. C., Noormets, A., Marani, M., & Katul, G. (2016). Soil–plant–atmosphere conditions regulating convective cloud formation above southeastern US pine plantations. *Global Change Biology*, *22*(6), 2238-2254.

McNaughton, K. G., & Spriggs, T. W. (1986). A mixed-layer model for regional evaporation. *Boundary-Layer Meteorology*, *34*(3), 243-262.

Meng, X. H., Evans, J. P., & McCabe, M. F. (2014). The influence of inter-annually varying albedo on regional climate and drought. *Climate Dynamics*, *42*(3-4), 787-803.

Molod, A., Takacs, L., Suarez, M., & Bacmeister, J. (2015). Development of the GEOS-5 atmospheric general circulation model: Evolution from MERRA to MERRA2. *Geoscientific Model Development*, *8*(5), 1339.

Myhre, G., Govaerts, Y., Haywood, J. M., Berntsen, T. K., & Lattanzio, A. (2005). Radiative effect of surface albedo change from biomass burning. *Geophysical Research Letters*, *32*(20).

Nicholson, S. E. (2011). *Dryland climatology*. Cambridge University Press.

Nicholson, S. E. (2015). Evolution and current state of our understanding of the role played in the climate system by land surface processes in semi-arid regions. *Global and Planetary Change*, *133*, 201-222.

Notaro, M., Wyrwoll, K. H., & Chen, G. (2011). Did aboriginal vegetation burning impact on the Australian summer monsoon?. *Geophysical Research Letters*, *38*(11).

Reichle, R. H., Liu, Q., Koster, R. D., Draper, C. S., Mahanama, S. P., & Partyka, G. S. (2017). Land surface precipitation in MERRA-2. *Journal of Climate*, *30*(5), 1643-1664.

Roy, D. P., Boschetti, L., Justice, C. O., & Ju, J. (2008). The collection 5 MODIS burned area product—Global evaluation by comparison with the MODIS active fire product. *Remote Sensing of Environment*, *112*(9), 3690-37

Seneviratne, S. I., *et al*. (2010). Investigating soil moisture–climate interactions in a changing climate: A review. *Earth-Science Reviews*, *99*(3-4), 125-161.

Snyman, H. A. (2003). Short-term response of rangeland following an unplanned fire in terms of soil characteristics in a semi-arid climate of South Africa. *Journal of Arid Environments*, *55*(1), 160-180.

Tosca, M. G., Diner, D. J., Garay, M. J., & Kalashnikova, O. V. (2015). Human-caused fires limit convection in tropical Africa: First temporal observations and attribution. *Geophysical Research Letters*, *42*(15), 6492-6501.

Vamborg, F. S. E., Brovkin, V., & Claussen, M. (2014). Background albedo dynamics improve simulated precipitation variability in the Sahel region. *Earth System Dynamics*, *5*(1), 89.

Van Heerwaarden, C. C., Vilà-Guerau de Arellano, J., Moene, A. F., & Holtslag, A. A. (2009). Interactions between dry-air entrainment, surface evaporation and convective boundary-layer development. *Quarterly Journal of the Royal Meteorological Society*, *135*(642), 1277-1291.

Veraverbeke, S., Verstraeten, W. W., Lhermitte, S., Van De Kerchove, R., & Goossens, R. (2012). Assessment of post-fire changes in land surface temperature and surface albedo, and their relation with fire–burn severity using multitemporal MODIS imagery. *International Journal of Wildland Fire*, *21*(3), 243-256.

Wendt, C. K., Beringer, J., Tapper, N. J., & Hutley, L. B. (2007). Local boundary-layer development over burnt and unburnt tropical savanna: an observational study. *Boundary-Layer Meteorology*, *124*(2), 291-304.

Chapter Five

Land surface brightening following wildfires in sub-Saharan Africa

Fully loaded satellites
Wait for a sign

Muse

5.1 Abstract

Albedo is an important component of the Earth's energy budget. Fire can induce long-lived changes to land-surface albedo, but the temporal evolution of these anomalies is poorly understood. Due to the widespread presence of fire in Africa, this represents substantial uncertainty in the continental energy budget, which has important implications for regional climate and hydrologic cycling. In this study, I present the first object-based accounting of albedo anomalies induced by larger (>1 km^2) individual fires in sub-Saharan Africa (SSA). I group spatially contiguous burnt pixels into fire objects and track the albedo anomaly for five years after the burn. I find that albedo anomalies all have the same general temporal signature: an immediate and short period of darkening followed by persistent brightening. The strongest brightening is found in the Kalahari region while more intense and persistent initial darkening is found in the Sahel region. The average albedo anomaly is $+2.71 \times 10^{-4}$ in the five years following fire, representing a statistically significant negative forcing on a continental scale. Over the Kalahari sands the albedo increases of ~0.02 represent approximately ~10 increase in the. This study challenges an existing paradigm surrounding the physical effects of fire on the landscape. These results suggest that models of albedo that assume a darkening and recovery to baseline are overly simplistic in almost all circumstances. Furthermore, the presumption that immediate darkening is the only meaningful effect on albedo is incorrect for at least half of the continent, and depending on the timing of fire, for Northern Hemisphere SSA as well.

5.2 Introduction

Albedo is a critical component of the Earth system and plays an important role in determining the terrestrial radiation budget. Changes to albedo can modify local atmospheric conditions and instigate land-atmosphere feedbacks with continental repercussions. A canonical example of an albedo-atmosphere feedback is the classic hypothesis of Charney [1975] invoked to explain multi-decadal drought in the Sahel. Charney [1975] hypothesized that persistent brightening due to desertification and associated positive albedo anomalies would enhance regional atmospheric subsidence, thereby reducing rainfall and further promoting desertification. There more recent, observational and mechanistic evidence that links fire-induced albedo changes to observed reductions in precipitation in the following wet season [Chapter Three; Chapter Four; *De Sales et al*., 2018]. This pathway of fire-induced rainfall suppression hinges on the presence of widespread positive anomalies in albedo (brightening) following extensive wildfire. The basic premise is that in fire-prone regions dominated by convective rainfall systems such as tropical Africa, reduced energy available for boundary layer growth under brighter than normal albedo conditions decreases the likelihood that the boundary layer will cross the lifting condensation level, a necessary condition for the formation of convective rainfall. This pathway could explain reductions in rainfall in regions where access to water resources is tightly coupled to human livelihoods. Furthermore, given the strong linkage between humans and fire [*Andela & Van Der Werf*, 2014], this could represent a novel way in which humans modify regional hydrologic cycling. Understanding the scope and magnitude of brightening is key to assessing the viability of this pathway on a continental scale.

Currently, there are inconsistent findings across Africa reporting how albedo anomalies after fire develop and recover over time, both in the sign and magnitude of anomalies. Ground based measurements of albedo change during and after fire are lacking in Africa. Therefore, many researchers have turned to long-term satellite reflectance datasets such as those derived from the Moderate Resolution Imaging Spectroradiometer (MODIS) to investigate fire-induced land surface changes. Previous studies have reported instantaneous decreases in albedo after fire by up to 50% [Govaerts *et al.* 2002; Gatebe *et al*. 2014]. Gatebe *et al*. [2014] reported significant darkening in Northern Hemisphere SSA that consistently lasted up to two years after fire for a majority of fire-affected pixels in the MODIS dataset. There was limited evidence of brightening in some cropland regions during the year following fire as well as in most regions when fire occurred outside of the fire season, but the number of pixels reporting brightening was statistically dominated by reports of extended darkening. Recently, Dwinte *et al.* [2017] measured widespread, immediate darkening after fires over all of Africa using a single pixel-based measurement approach.

On the other hand, in Chapter Four, I presented evidence of strong brightening (up to ~+7% above baseline albedo) in the Kalahari region of Southern Hemisphere Africa in the months following dry season fire [Chapter Four]. The measured effect was more pronounced in more arid environments. Wetter regions showed slight darkening over the same timescale. Elsewhere on the globe there are reports of immediate halving of albedo following intense fires in Australia [*Beringer et al*., 2003] and significant brightening in the years following intense wildfires in Greece [*Veraverbake et al*., 2012]. Notably, all of these studies relied on data derived from MODIS reflectances, which suggests that data sources are not the driving factor between differences in fire-induced albedo change.

The extent to which these studies differ because of geographic or methodological differences is unclear. Each of the aforementioned studies computes changes in albedo due to fire differently. Perhaps the main issue is in determining a reference baseline value for albedo so that an anomaly can be calculated after fire occurs. For example, if the anomaly were purely temporal (i.e. comparing the albedo in a burn scar to the albedo in that same region before or well after it burned) then it is possible that the computed anomaly would capture factors like temporary drought that temporarily modify both albedo and the likelihood of fire. On the other hand, if only a spatial reference were used (i.e. comparing albedo in a burn scar to a different, unburned region at the same time) then I could not ensure that the surrounding pixels actually had a similar long-term baseline albedo.

Part of this difficulty stems from the fact there is no standard way to calculate albedo anomalies using a spatial or temporal reference. Given the natural spatial covariance of a spreading process like fire, there is some difficulty in establishing a nearby, representative reference pixel because many potential reference pixels have also burned. Indeed, Gatebe *et al*. [2014] used a spatial window ranging from 2.5 km to 30 km in their reference pixel matching scheme to associate burnt pixels with similar reference pixels. There is a question of how truly representative a reference 500 m pixel that is ~30 km away from the burned pixel actually is. Dwinte *et al*. [2017] point out another potential issue with spatial references. The fact that a potential reference region *didn't* burn in proximity to a burn scar could be indicative of underlying dissimilarity between the two pixels; making that an unsuitable reference to measure albedo anomalies. Without correcting for underlying biases between the two pixels, this comparison would be invalid.

On the other hand, there are also potential issues with temporally-derived baselines. Regions with an active fire regime show a strong fuel buildup and burn cycle. Multiple studies have demonstrated how climatic correlates such as previous wet season rainfall modify fire in the following dry season [*Mondal & Sukumar*, 2016; Chapter Three]. Therefore, albedo anomalies calculated with only a temporal baseline might instead be capturing signals of temporal shifts in overall climate that are linked to both albedo and fire. For example, Dwinte *et al*. [2017] use an albedo anomaly calculated using the average of the year before the fire and after the fire. By using a control baseline derived from data in the year following fire, there is an implicit assumption that full recovery has occurred in less than a year. However, if brightening lasting longer than a year were actually occurring past that window then their methodology would both (a) overestimate the darkening associated with fire, and (b) fail to sense the brightening occurring after the first year. However, there is ample evidence of fire-induced land surface effects that last on the order of years (e.g. *Veraverbeke et al*. [2012], *Gatebe et al*. [2014]), which challenges the assumptions of the other mentioned studies. Without ground-based evidence of limited temporal effects in Africa, anomaly calculations must be designed to incorporate this potential effect.

Despite recognition of issues with both spatial- and temporal-only anomaly definitions, to date no study has attempted to account for both kinds of pitfalls on a continental scale. I aim to fill this gap with an improved methodology. The specific temporal lags and apparent disparity in albedo anomalies across hemispheres clearly warrant further investigation. However, despite the common occurrence of fire in Africa and potential impact on the continental radiation budget, a holistic continental analysis that investigates the long-term evolution of fire-induced albedo changes using a unified framework has not yet been undertaken. That is the aim of the current study.

5.3 Data & Methods

5.3.1 Fire data

The MODIS burned area product (MCD45A1, collection 6) gives global estimates of whether or not a given 500 m resolution pixel burned and, if so, estimates the time at which that pixel burned [*Roy et al*., 2008]. I tracked fires from this dataset during the period April 2006 through March 2011 (5 years of data). April was chosen as the start of the fire year due to a continental minimum of fire during the month of April. I reserved the period before this for use in the calculation of the baseline albedo. I stopped tracking new fires in 2011 to ensure that the anomalies could be calculated for a full 5 years after the fire occurred.

5.3.2 Fire object characterization

I defined fires using an object oriented, rather than a single pixel-based, approach. My object-oriented analysis groups individual burned pixels into discrete fire events based on their spatio-temporal connectivity. I used a Moore (8-neighbor) spatial connectivity and 5 days of temporal connectivity. After defining all individual objects, further analyses were then done on the aggregated values of the member pixels, rather than on the individual pixels themselves. Instead of comparing a single burnt pixel to other single burnt pixels, I defined a reference buffer to compare albedo values to. Similar to my fire objects, the reference buffer is a contiguous group of pixels to which I compare the albedo of fire objects against. To define the reference buffer, I first excluded a one-pixel buffer around each fire to exclude. These pixels were not considered in further analysis to reduce the potential of edge effects of partially burned pixels in my fire-reference comparison. After than I initialized the reference buffer as a one-pixel buffer outside the excluded edge pixels. Following initialization, the reference buffer was iteratively built up by incrementally adding a 1 pixel outer buffer to the external border until the number of pixels in the reference buffer contained at least the number of pixels in the fire object. In this way, I was comparing the fire object to a similar number of nearby pixels.

The linkage between fire and anthropogenic land use has the potential to affect the results. For example, if fire was used to clear forest that is then maintained as pasture, I may falsely associate the extended change in albedo with fire, even though the extended change in albedo is unrelated to the fact that a fire was observed and was being artificially maintained by human activity. For this reason, I focus on fires that do not overlap with human activities. I address this potential issue by omitting any pixels classified as either urban, cropland or cropland mosaic by the MODIS IGBP land cover dataset [*Friedl et al.*, 2010].

I performed additional quality assurance steps to ensure a strong albedo signal. Most notably, I excluded fires with an area < 1 km^2 (i.e. consisting of 4 or fewer MODIS pixels). This was to reduce the number of cases in which a small fire comprised a very small area of the burned pixel an lead to an overestimate of burned area. Indeed, the MODIS burned area product can routinely detect the fires smaller than 1000 m^2 (or ~30 m x 30 m) within the larger ~500 m x 500 m MODIS pixel. In these cases tracking the albedo over the larger pixel that is not substantially burned would result in a scale mismatch that could lead to reduced statistical power and an overly conservative anomaly estimate.

5.3.3 Albedo anomaly calculation

For each fire object, I tracked the average albedo of the fires and reference buffers for five years after the fire. For each point in time (specifically each 8-day period for which MODIS albedo data are available) I calculated the spatiotemporal albedo anomaly as

(1) $\Delta\alpha_t = [\alpha_{t,f} - \alpha_{h,f}] - [\alpha_{t,r} - \alpha_{h,r}]$

where the subscript $_t$ denotes the albedo at a given time after fire, subscript $_h$ denotes the historical albedo at the same time of year averaged over the period April 2001 through March

2006. The subscripts $_f$ and $_r$ denote the average albedo within the fire object and the surrounding reference buffer, respectively. I believe that using both a spatial and a temporal reference for albedo anomaly computation is necessary to reduce the spurious effects of using a single method as discussed in the Introduction. This allows us to achieve higher quality estimates of fire performance that consider both underlying differences in the spatial and temporal heterogeneity of the landscape and represents an improvement upon previous studies.

5.4 Results and Discussion

I identified 1.54 M fires, amounting to 11.2 M km^2 of burned area over the five-year period, or approximately 11% of the continental area of Africa. Due to the strict quality requirements for fire objects classification, the fire objects represent 88% of fire pixels in the MODIS dataset over my period of record. For this reason, the total impact of fire shown in results is likely to be an underestimate. Smaller fires dominated the dataset. Of the fires I identified, 65.4% exceeded 10 km^2 and 31.0% exceed 100 km^2. The average albedo anomaly in the year following fire was +6.51 x 10^{-4} for all of sub-Saharan Africa. The five-year continental average was +2.71 x 10^{-4}. Overall, the return to baseline generally occurred within the first two years after fire (Fig. 5.1, black lines).

I identified a general temporal signature of albedo anomaly development. First, there is a strong immediate darkening that recovers within about three months. After that there is less intense, but still significant, brightening up to about one year after fire. Depending on the region, there is some variability in this signature. For example, fires that occur in the Southern Hemisphere during the wet season show no immediate darkening but later substantial brightening around 6 months after fire. These findings of dominant darkening in the Northern Hemisphere and dominant brightening in the southern Hemisphere unify seemingly conflicting reports of hemispheric differences in the physical effect of fire on the land surface (e.g. Chapter Two and Gatebe *et al*. [2014]).

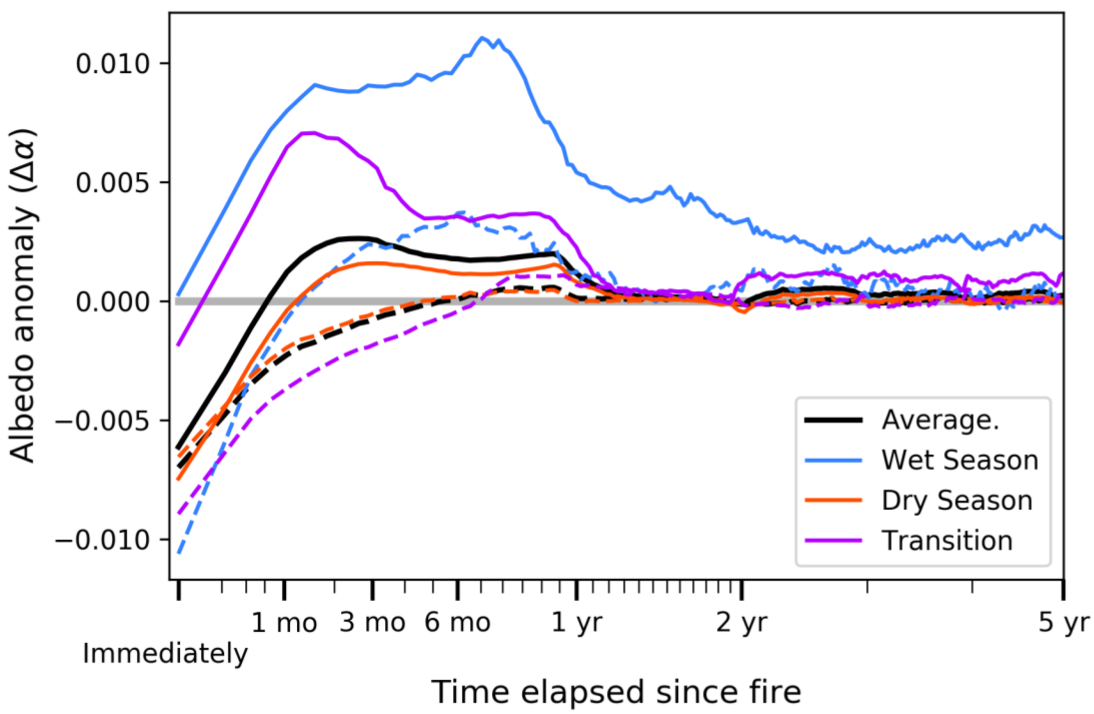

Figure 5.1. Evolution of albedo anomalies after fire for the Northern (dotted line) and Southern (solid line) Hemisphere. Different colors represent different times of year. The wet season months are JJAS for the Northern Hemisphere and DJFM for the Southern Hemisphere. October, November, April and May are considered transition months for both hemispheres. Each line is the average of all fires that occurred within the given time of year weighted by the area of each fire. The whole year average (black) closely tracks the dry season (orange) average because most fires occur during the dry season.

The amount of brightening is dependent on when and where the fire occurs. Wet season fires result in substantially more brightening than fires during other times of the year within each respective hemisphere (Fig. 5.1, blue lines). This is especially the case in the Northern Hemisphere. Gatebe *et al*. [2014] report similar findings after Northern Hemisphere fires but suggested a possible statistical anomaly due to low sample size. I believe that the observed effect is important and must be considered in future studies. I hypothesize that the severity of rarer wet season fires, when they do burn, tends to be greater, as they would occur only during extremely dry times such as intense drought. Additionally, during the wet season, the vegetated unburnt reference region may be substantially less reflective than the underlying soil, leading to an intensified brightening. If the relative contrast between the brighter burn scar and darker wet season vegetation more pronounces, then this could account for the stronger brightening observed in the wet season signal. Further research efforts should aim to decouple these two signals of darkening char deposition and potential brightening to gain a more complete understanding of fire-induced surface changes. Vegetation cover and species could play a large role in determining the magnitude of immediate darkening due to char.

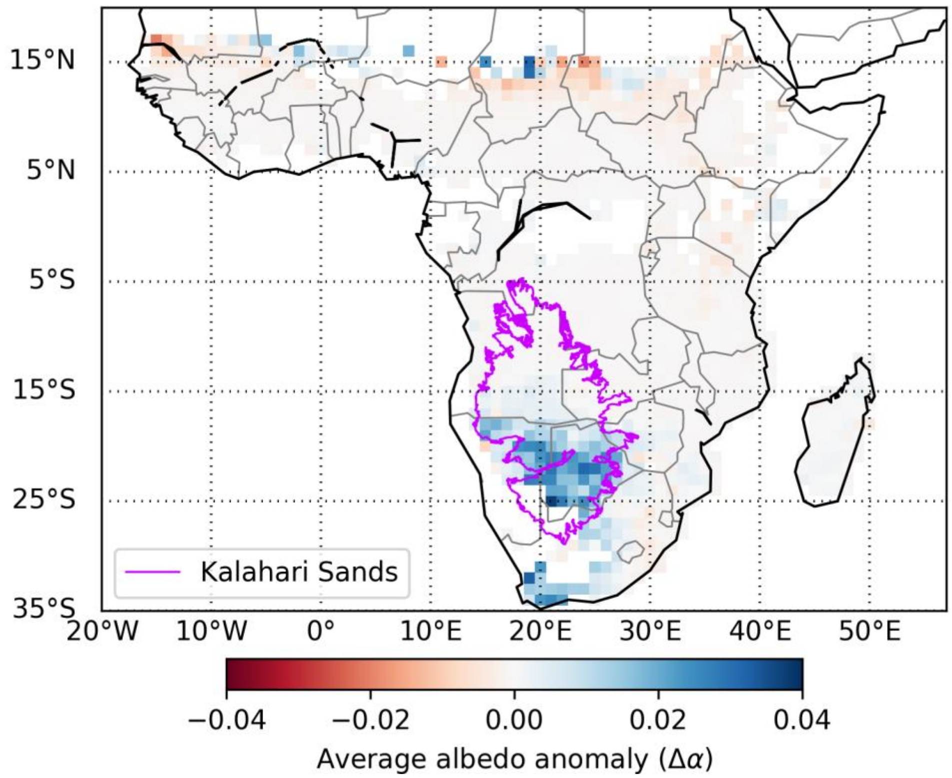

Figure 5.2. Average albedo anomaly in the year following fire. Individual albedo time series are binned into 1° latitude and longitude bins and averaged by weighting each fire by area before averaging. Bins with less than XX fires are shown in white. An outline of the Kalahari Sands is shown in fuschia.

The Kalahari region exhibits a strong brightening that lasts for over a year, on average. I suggest that the soil color is important in explaining the brightening, as there is a significant contrast between the brightening observed over the Kalahari sands (arenosols) and the nearby darker luvisols and south-east Africa of the (Fig. 5.2; eastern border of purple line representing Kalahari sands; Dewitte *et al*. [2013]). The brightening is subdued in the northern half of the Kalahari sands. This could be an effect of spatial trends in soil moisture. The negative relationship between soil moisture and albedo across soil types is well described [*Lobell & Asner*, 2002]. It is likely that the revelation of wetter, darker soils has less of an effect on albedo anomalies. This is supported by the fact that the highest average albedo anomalies following wet season fires (2.71×10^{-4} and 2.71×10^{-4} for the NH and SH, respectively), occur about 6 months after the burn (i.e. during the dry season). To the south of the Kalahari (i.e. the South African veld), the decreasing frequency of fire precludes us from drawing definitive conclusions about fire-induced albedo changes. The timing of brightening also shows differences from surrounding areas. The fastest brightening also occurs in the Kalahari sands, on average in 31 days after fire (Fig. 5.3). In the Northern Hemisphere brightening occurs after 107 days on average, compared to the 60 days for the Southern Hemisphere.

This methodology represents an advancement over previous research for three reasons. First, this methodology addresses concerns raised about both temporal-only and spatial only comparisons. I account for both underlying differences between the burned pixels and reference pixels that might taint a purely spatial calculation and temporal factors such as drought that might affect a purely temporal calculation. Second, I do not assume the sign of the albedo anomaly will be either positive or negative. Previous research has typically assumed that darkening will be observed, and as such, some detection algorithms are modeled around finding the minimum albedo after fire (e.g. Gatebe *et al*. [2014], Dwinte *et al*. [2017]). Finally, I do not assume any set duration for the recovery of albedo after fire. Previous studies have focused on the immediate darkening that occurs after fire, and then measured the recovery to a baseline or assumed implicitly that meaningful albedo changes do not last longer than one year. Because of that, previous studies do not capture the extended brightening of which I have found convincing evidence across Africa.

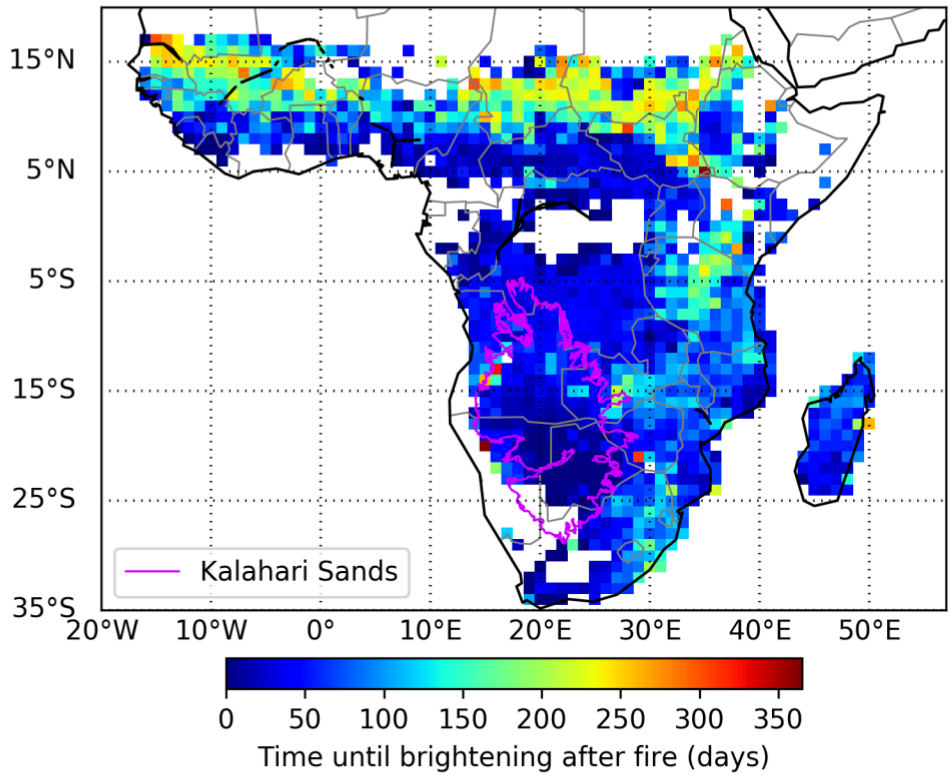

Figure 5.3. Timing of first brightening following fire. Individual albedo time series are binned as in Figure 2 using a weighted average. The timing for the first observed brightening for these binned averages is depicted here. An outline of the Kalhari Sands is shown in fuchsia.

Understanding the effect of fire on the overlying atmosphere through physical modeling is an active research area [e.g. *Hernandez et al.*, 2015; *De Sales et al.*, 2016; Chapter Three; *De Sales et al.*, 2018]. The parameterization of fire in climate models is key to describing how burn scars modify regional climate and how this relationship may change under future fire regimes. This study contributes fundamental understanding to how the physical effects of fire should be parameterized for the most fire prone region on Earth.

References

Andela, N., & Van Der Werf, G. R. (2014). Recent trends in African fires driven by cropland expansion and El Nino to La Nina transition. *Nature Climate Change*, *4*(9), 791.

Beringer, J., Hutley, L. B., Tapper, N. J., Coutts, A., Kerley, A., & O'grady, A. P. (2003). Fire impacts on surface heat, moisture and carbon fluxes from a tropical savanna in northern Australia. *International Journal of Wildland Fire*, *12*(4), 333-340.

Charney, J. G. (1975). Dynamics of deserts and drought in the Sahel. *Quarterly Journal of the Royal Meteorological Society*, *101*(428), 193-202.

De Sales, F., Xue, Y., & Okin, G. S. (2016). Impact of burned areas on the northern African seasonal climate from the perspective of regional modeling. *Climate Dynamics*, *47*(11), 3393-3413.

De Sales, F., Okin, G. S., Xue, Y., & Dintwe, K. (2018). On the effects of wildfires on precipitation in Southern Africa. *Climate Dynamics*, 1-17.

Dewitte, O., *et al*. (2013). Harmonisation of the soil map of Africa at the continental scale. *Geoderma*, *211*, 138-153.

Dintwe, K., Okin, G. S., & Xue, Y. (2017). Fire-induced albedo change and surface radiative forcing in Sub-Saharan Africa savanna ecosystems: implications for the energy balance. *Journal of Geophysical Research: Atmospheres*.

Friedl, M. A., Sulla-Menashe, D., Tan, B., Schneider, A., Ramankutty, N., Sibley, A., & Huang, X. (2010). MODIS Collection 5 global land cover: Algorithm refinements and characterization of new datasets. *Remote sensing of Environment*, *114*(1), 168-182.

Gatebe, C. K., Ichoku, C. M., Poudyal, R., Román, M. O., & Wilcox, E. (2014). Surface albedo darkening from wildfires in northern sub-Saharan Africa. *Environmental Research Letters*, *9*(6), 065003.

Govaerts, Y. M., Pereira, J. M., Pinty, B., & Mota, B. (2002). Impact of fires on surface albedo dynamics over the African continent. *Journal of Geophysical Research: Atmospheres*, *107*(D22).

Hernandez, C., Drobinski, P., & Turquety, S. (2015). Impact of wildfire-induced land cover modification on local meteorology: A sensitivity study of the 2003 wildfires in Portugal. *Atmospheric Research*, *164*, 49-64.

Lobell, D. B., & Asner, G. P. (2002). Moisture effects on soil reflectance. *Soil Science Society of America Journal*, *66*(3), 722-727.

Mondal, N., & Sukumar, R. (2016). Fires in seasonally dry tropical forest: testing the varying constraints hypothesis across a regional rainfall gradient. *PloS One*, *11*(7), e0159691.

Roy, D. P., Boschetti, L., Justice, C. O., & Ju, J. (2008). The collection 5 MODIS burned area product—Global evaluation by comparison with the MODIS active fire product. *Remote Sensing of Environment*, *112*(9), 3690-3707.

Veraverbeke, S., Verstraeten, W. W., Lhermitte, S., Van De Kerchove, R., & Goossens, R. (2012). Assessment of post-fire changes in land surface temperature and surface albedo, and their relation with fire–burn severity using multitemporal MODIS imagery. *International Journal of Wildland Fire*, *21*(3), 243-256.

Chapter Six

Conclusions and Future Research

This dissertation advanced the states of knowledge of fire-climate interactions on multiple fronts. In Chapter Two, I demonstrated that strong seasonality in climate signal can greatly enhance the predictability of annual burnt area across the globe. This was done with simple, interpretable seasonality metrics that could be applicable beyond the field of fire science. Furthermore, this single, global model performed remarkably well across the different biomes on Earth.

In Chapters Three through Five I developed the new concept of fire-induced rainfall suppression over seasonal timescales via land surface modification. First, I used satellite data to link observations of excessive dry season fire to subsequent reductions in wet season rainfall. This effect is estimated to be the strongest in the Kalahari region of southern Africa. Building on this finding, I employed a boundary layer model to investigate possible mechanisms of this observed suppression. The major finding was that increases in albedo after fire—or brightening—could potentially explain rainfall suppression. Finally, in Chapters Four and Five I used continental scale satellite data to demonstrate that there is overwhelming brightening after fire in the Kalahari. This provides strong evidence of brightening as a mechanistic explanation of rainfall suppression. However, while strong enough to drive a continental brightening effect, this has phenomenon not yet been explained. Finding the root causes will require a better understanding of the interplay between the immediate effect and extended recovery of vegetation and soil moisture and their respective albedos. Ground based measurements could be the key to understanding this why the Kalahari exhibits a uniquely strong effect. A necessary future research direction is to incorporate the evidence of brightening in fully coupled regional climate models. Recent studies have started this investigation, but a richer parameterization of fire-induced albedo changes is still needed. These investigations are relevant on scientific and societal levels because the land-surface changes due to fire are long-lasting and may affect precipitation for months.

In addition to the knowledge gained, this dissertation represents advances in methodology that will be useful to future researchers. Firstly, in Chapter Two I developed a framework for calculating seasonality metrics over a general periodic signal. This framework is extensible to cyclical or seasonal patterns of arbitrary temporal resolution. One specific area of research where this could be useful is in the characterization of the seasonal cycle of fires in regions across the globe. The high seasonality of fire in many regions of the globe lends itself to a description using the seasonal metrics. This area of research could inform more accurate global yearly carbon accounting through a better understanding of the global fire cycle. Furthermore, these high-level metrics may help fire scientists establish baselines for shifting fire activity in a future, warmer, climate and detect yearly anomalies in the dryland carbon sink.

The work presented in Chapter Four represents methodological advances on two fronts. The grouping of single pixels into spatially coherent fire objects and reference buffers presents advantages over pixel-centric approaches. I also presented a combined spatiotemporal anomaly computation that addresses the drawbacks of a purely spatial or temporal reference. In particular, this approach was used to reveal previously unreported findings of large scale brightening in southern Africa, a finding heretofore hidden from investigations using less sophisticated methodologies. Through the use of large scale satellite data and novel methodology, this dissertation provides a more holistic understanding of the role of fire in the Earth System.

Appendices A1 to A2

Appendix One

A2.1 Statistical Modeling

I fitted the GAM using the ‘mgcv’ package in R [*Wood*, 2006]. The model selection and assessment is largely based on ref. 33. Across the study domain, P_{WS} showed a positive mean-variance relationship, violating the model assumption of constant variance in residuals. Additionally, the P_{WS} shifted from highly right skewed in arid regions to an approximately symmetric distribution in wetter regions. I found that using a square root transformation of P_{WS} with a normal distribution and identity link function resulted in appropriate model residuals (constant variance in residuals). Therefore, I used the square root transformation on the response variable for my model. My GAM was of the form:

$$(1)\ P_{WS}^{1/2} \sim \mathbf{s}(\langle P_{WS}\rangle, k) + \mathbf{te}(F_E, \mathrm{MAP}, k) + \mathbf{te}(F_L, \mathrm{MAP}, k)$$

Where **s** is a univariate smooth, **te** is a bivariate smooth formed as the tensor product of two smooths, $\langle P_{WS}\rangle$ is the temporal average of P_{WS} for each pixel and k is a smoothness parameter. I used a thin plate regression spline smoother with shrinkage for all smooth terms. To prevent overfitting, I restricted k in each fire term to a low value and incrementally increased it until summary diagnostics indicated that the smoothing basis dimension was sufficient (i.e. k-index values were close to 1). Using this procedure, I selected k=4 for each tensor term. Additionally, I set the gamma term to 1.4 to reduce overfitting [*Wood*, 2006].

To assess model suitability, I fit a null model (M_0) that excluded the two fire tensor terms in (1), I used the AIC to compare the model with fire as a predictor variable to a null model that only included a smooth of $\langle P_{WS}\rangle$. The AIC is a measure of model quality that takes into account model fit and complexity. Here a lower value of AIC indicates a more parsimonious model. The AIC for the M_F was lower than that of M_0 (M_0= 539611.2, M_F=539120.3), which suggests that fire variables are relevant to explaining variance in rainfall.

I note that the deviance explained, an analogue to the adjusted R^2 for GAMs, differs little between each model (M_0=65.6%, M_F=65.7%) over the entire model domain. For this reason, M_F is not likely to offer an improvement in predictive performance over M_0. While other statistical techniques may perform better in this respect, they can lack the interpretability of the contribution of individual model terms and interactions that is afforded by GAMs. As my main goal was to describe the observed relationship between fire and subsequent rainfall, rather predict rainfall totals, I chose GAMs. Fig. 2A estimates the average rainfall 'lost' due to fire based on mean F_E and F_L for each pixel. The estimates presented in Fig 2A are calculated by subtracting model estimates of M_F at average F_E, and F_L from estimates of M_F at F_E=0 and F_L=0. In Fig. 2B, I show the values in Fig. 2A divided by $\langle P_{WS} \rangle$.

References

Wood, S. (2006) *Generalized Additive Models. An Introduction with R.* Chapman & Hall/CRC, New York.

Appendix Two

A2.1 Boundary Layer Growth Model

A2.1.1 Model Details

My modeling approach is adapted from McNaughton and Spriggs [1986]. In this model, the boundary layer is represented as a well-mixed layer with potential temperature θ and specific humidity q. Above the boundary layer the free-atmosphere profile of potential temperature (θ_{FA}) and specific humidity (q_{FA}) changes linearly with height. The exact values of θ_{FA} and q_{FA} are a function of height above the land surface, z. The undisturbed free atmosphere profiles are:

(1) $\theta_{FA}(z) = \gamma_\theta z + \theta_0$

(2) $q_{FA}(z) = \gamma_q z + q_0$,

where γ_θ and γ_q are the slopes of the profiles, and θ_0 and q_0 the extrapolated intercepts at the z=0 for potential temperature and specific humidity, respectively. I use the values presented in Lhomme and Elguero [1999] of γ_q=2.85 x 10^{-6} m^{-1}, γ_θ=4.78 x 10^{-3} K m^{-1} which are based on a linear fit to a typical mid-latitude summer undisturbed free atmosphere profile. Then intercepts are uniquely determined for each day by extrapolating the initial (morning) boundary layer values of θ and q at the reanalysis-determined initial boundary layer height to z=0. Initial conditions are taken from reanalysis data at the time of model initialization. Boundary layer growth is promoted by sensible heat flux (H, units: W m^{-2}) at the land surface. The change in height, h, of the boundary layer is expressed as:

(3) $\frac{dh}{dt} = \frac{H}{\rho c_p h \gamma_\theta}$,

where ρ is the density of the air at the top of the boundary layer and c_p is the specific heat capacity of dry air at constant pressure. Following Lhomme and Elguero [1999], these are taken to be constants with values 1.05 kg m^{-3} and 1005.7 J kg^{-1} K^{-1}, respectively. The evolution of specific humidity in the mixed layer is governed by the amount and characteristics of entrained free atmosphere air incorporated into the boundary layer:

(4) $$\rho h \frac{dq}{dt} = E + \rho(q_{FA} - q)\frac{dh}{dt}$$

where E is the evaporation rate at the land surface (kg s^{-1} m^{-2}) found by dividing latent heat flux (λE) by the latent heat of vaporization (λ). Likewise, changes in potential temperature can be expressed as:

(5) $$\rho c_p h \frac{d\theta}{dt} = H + \rho c_p(\theta_{FA} - \theta)\frac{dh}{dt}$$

The only temporally variable parameters in the boundary layer growth model are H and E. For each day of reanalysis data, I start the simulation when H is consistently positive (daytime conditions) and run the simulation until H is no longer positive. The values of θ, q, and h are initialized from near surface reanalysis data at the beginning of each day. Equations (3-5) are solved explicitly with a small time-step (1 minute). Hourly modified flux data derived from reanalysis and used to drive this model (H and λE; see following section) are resampled to the simulation timescale using linear interpolation. For each latitudinal position along the latitudinal transect, the boundary layer growth model is run for all days during the months of November and February, 1980-2015.

A2.1.2 Representing Fire in the Model

I represent fire in the model by artificially modifying the shortwave radiation budget and the partitioning between latent and sensible heat fluxes provided by the reanalysis data. I use the term simulation to refer to the group of model runs over all individual days in the reanalysis record for a given set of experimental variables.

A2.1.2.1 Albedo Modification

Fire tends to immediately darken the land surface, in some cases halving albedo [*Beringer et al.*, 2003]. However, at longer time scales fire may result in an optically brighter land surface. Because of this uncertainty, I test both darkening and brightening in my experimental framework. The relevance of this choice is further explored in the Discussion section. I represent the change in albedo after fire as a fractional change, f_α, so that the albedo value α that I use for a given simulation is:

(6) $$\alpha = f_\alpha \ \alpha_{RA}$$

where α_{RA} is the surface albedo in the MERRA-2 reanalysis data for the site. Values of f_α less than and greater than 1 represent darkening and brightening of the land surface, respectively. The change in the shortwave energy budget due to this albedo change, ΔS, is given by the equation:

(7) $$\Delta S = \alpha \ S_i - \alpha_{RA} \ S_i$$

where S_i is hourly downwelling shortwave radiation (W m^{-2}; derived from RA). In this model, I assume that only the shortwave radiation budget is modified. After actual fires, generally there is an increase in land surface temperature, which presumably modifies the net long-wave radiation budget, but I do not consider that aspect in this study. This omission is not expected to be important; Beringer *et al*. [2003] found that despite halving of albedo after fire, the outgoing longwave radiation only increased by 10% after fire in an Australian savanna. With this assumption the proportional change in net radiation, p, is

(8) $$p = (\Delta S + R_{RA}) / R_{RA}$$

where R_{RA} is hourly reanalysis net radiation. I assume that the changes in available energy result in proportional changes to the component heat fluxes at the surface:

(9) $$R_N = p \ \lambda E_{RA} + p \ H_{RA} + p \ G_{RA}$$

Where R_N is the modified net radiation (=p R_N) and λE_{RA}, H_{RA}, and G_{RA} are the hourly values of latent heat flux, sensible heat flux and ground heat flux taken from reanalysis data. The values of sensible and latent heat flux after albedo modification and associated shortwave radiation changes are given as

(10) $$H_\alpha = p\, H_{RA}$$

(11) $$\lambda E_\alpha = p\, \lambda E_{RA}$$

respectively.

A2.1.2.2 Latent Heat Flux Changes

In addition to modifying the radiative properties of the land surface, fire damages and removes plants. By destroying transpiring leaves, ecosystem latent heat flux may decline to one quarter of undisturbed values, resulting in significantly increased sensible heat fluxes [*Beringer et al.*, 2003]. Here I consider a fractional change in latent heat flux, $f_{\lambda E}$, due to fire. I maintain the assumption that ground heat flux is a constant proportion of R_N. Therefore, changes to λE_α translate to proportional changes in H_α. The final values of H and λE used to drive simulations are:

(12) $$H = H_\alpha + \Delta\lambda E_\alpha$$

(13) $$\lambda E = \lambda E_\alpha - \Delta\lambda E_\alpha$$

where the value $\Delta\lambda E_\alpha = f_{\lambda E}\, \lambda E_\alpha$ represents the component of latent heat flux that is converted into sensible heat flux.

To summarize, the main experimental variables in this study are f_α and $f_{\lambda E}$, which represent fractional changes in albedo and latent heat flux, respectively. In this study, I consider how changing these values results in boundary layer differences as compared to the control case in which f_α and $f_{\lambda E}$ are equal to 1 (and therefore $H = H_{RA}$ and $\lambda E = \lambda E_{RA}$).

A2.1.3. LCL Calculation

The height of the LCL, h_{LCL}, is calculated by first determining the temperature of the LCL [*Bolton*, 1980]:

$$T_{LCL} = \frac{2840}{3.5ln(T) - ln(e) - 4.805}$$

where T (K) is the near surface air temperature calculated from θ and P_S, and e (mbar) is the near surface vapor pressure calculated from q and T. The pressure at the LCL, P_{LCL} (Pa), is calculated as:

$$P_{LCL} = P_S \left(\frac{T_{LCL}}{T}\right)^{3.5}.$$

Where P_S (Pa) is the hourly surface pressure from the reanalysis dataset. Finally, the height of the LCL, h_{LCL} (m) is found using

$$h_{LCL} = \frac{RT}{Mg} ln\left(\frac{P_S}{P_{LCL}}\right).$$

Where R is the universal gas constant (8.314 J mol^{-1} K^{-1}), M is the molecular weight of dry air (0.029 kg mol^{-1}) and g is acceleration due to gravity (9.8 m s^{-2}). At a given time-step LCL is determined by the temperature and moisture content of the mixed layer. To investigate the propensity of convective rainfall, I compute LCL heights at the 1-hour timestep of the original reanalysis data, noting when the condition $h > h_{LCL}$ is met during any time step. I report how varying the parameters f_α and $f_{\lambda E}$ contribute to differences in the average rate of crossings across the whole record.

A2.2. Details on the relationship between crossing statistics and rainfall characteristics

I use the bias-corrected rainfall data that is provided with MERRA to characterize how rainfall characteristics vary with the number of midday crossing hours at four sites along the Kalahari Transect. Afternoon rainfall is a proxy of convective rainfall due to common convective afternoon storms that dominate these regions. Afternoon rainfall has been successfully applied to diagnosing land-atmosphere interactions in previous studies [*Guillod et al.*, 2015]. The corrected MERRA-2 rainfall product is a combination of reanalysis generated rainfall and observational datasets. Further details on the corrected MERRA-2 precipitation can be found in Reichle *et al.* [2017]. I investigate two rainfall characteristics: (1) the total afternoon rainfall amount and (2) maximum rate. In each case the independent variable is the duration (in hours) of for which h_{LCL} exceeds h during midday *(1000 LST to 1600 LST)*. The conditional distributions of these rainfall characteristics are presented in Fig. 4.4 and Fig. 4.5, respectively.

A2.2. Details on the calculation of the spatial albedo anomaly

In addition to the temporal anomalies outlined in the main text (Section *4.3.5 Fire and Albedo Satellite Data*), I calculate a spatial albedo anomaly that highlights the spatial differences in November albedo between burnt and unburnt regions. This addresses the issue of whether the temporal anomalies are due to and increases our confidence that brightening is not an artifact of spurious climate correlations.

Using the same spatial domain, study period and 500 m MODIS fire and albedo satellite products as the analysis presented in Section 2.5, I calculate, for each pixel and year, whether a pixel has burned in the dry season (April-October) and the average November albedo anomaly. For each year of record, I chunk the domain into 0.25 degree latitude/longitude blocks. I calculate the spatial albedo anomaly for each pixel as the November albedo in each burnt pixel minus the average November albedo of unburnt pixels in the chunk for the same year. These anomalies are normalized by dividing by the average albedo of the chunk in the same year from which they were sampled and aggregated across all years. These distributions, pooled into bins based on each chunk's MAP and expressed as a percentage change, are presented in Fig.4.9.

References

Beringer, J., Hutley, L. B., Tapper, N. J., Coutts, A., Kerley, A., & O'grady, A. P. (2003). Fire impacts on surface heat, moisture and carbon fluxes from a tropical savanna in northern Australia. *International Journal of Wildland Fire*, *12*(4), 333-340.

Bolton, D. (1980). The computation of equivalent potential temperature. *Monthly Weather Review*, *108*(7), 1046-1053.

Guillod, B. P., Orlowsky, B., Miralles, D. G., Teuling, A. J., & Seneviratne, S. I. (2015). Reconciling spatial and temporal soil moisture effects on afternoon rainfall. *Nature Communications*, *6*, 6443.

Lhomme, J. P., & Elguero, E. (1999). Examination of evaporative fraction diurnal behaviour using a soil-vegetation model coupled with a mixed-layer model. *Hydrology and Earth System Sciences Discussions*, *3*(2), 259-270.

McNaughton, K. G., & Spriggs, T. W. (1986). A mixed-layer model for regional evaporation. *Boundary-Layer Meteorology*, *34*(3), 243-262.

Reichle, R. H., Liu, Q., Koster, R. D., Draper, C. S., Mahanama, S. P., & Partyka, G. S. (2017). Land surface precipitation in MERRA-2. *Journal of Climate*, *30*(5), 1643-1664.